Production of optically functional nanoscale structures by chemical de-alloying of metallic precursor alloys

By Matthew Tai

Supervisors: Assoc. Prof. Matthew Arnold, Dr. Annette Dowd and Dr. Angus Gentle

Doctor of Philosophy: Science

11/07/2019

Certificate of Original Authorship

I, Matthew Tai declare that this thesis, is submitted in fulfilment of the requirements for the award of Doctor of Philosophy (PhD) - Science, in the School of Mathematics and Physical Sciences, Faculty of Science at the University of Technology Sydney. This thesis is wholly my own work unless otherwise reference or acknowledged. In addition, I certify that all information sources and literature used are indicated in the thesis.

This document has not been submitted for qualifications at any other academic institution. This research is supported by the Australian Government Research Training Program.

Signature:

Production Note:
Signature removed prior to publication.

Matthew Tai

Date: 11/07/2019

Acknowledgements

Firstly I would like to thank and acknowledge my supervisors Matthew Arnold, Annette Dowd and Angus Gentle for assisting me through this long endeavour. Their expertise and vast knowledge has taught me many new things in this field. The time they have sacrificed to explain and discuss crucial information to me has been invaluable and much appreciated. I would also like to thank them for allowing me to undertake a PhD under them and their supervision. A special thanks to Michael Cortie for guidance and useful advice to progress my research and for the time he put in to proof-read my thesis. Thanks to Geoff Smith for overseeing the funding of my project and also to the Australian Research Council (DP140102003) for funding my scholarship. I would also like to thank the Graduate Research School for funding through the Vice-Chancellor's Postgraduate Research Students Conference Fund which allowed me to attend an international conference.

Next I would like to thank lab managers, technicians and staff that assisted me in conducting experiments in the lab. Thanks to Geoff McCredie who made it possible for me to complete experiments and troubleshoot problems with machines and systems in the vacuum laboratory. I would also like to thank him for allowing me to learn to troubleshoot my own sputter chamber and assist with any upgrades and add-ons that was made to the chamber. For all things done in the MAU labs I would like to acknowledge Katie McBean, Mark Berkahn and Herbert Yuan for their assistance and patience to answer my many questions. They were all a great help using the SEM, TEM and XRD, teaching me and reminding me of the step to take to use the machines effectively.

I am thankful for the PhD students who I have been able to meet throughout my candidature, especially those who started at the same time as me: Mika Westerhausen, Marc Galí, Kerem Bray and Alba Santín. The ability to talk and make friendships with them has been helpful to de-stress and enjoy my time as a PhD student. I would like to further express my gratitude to my other colleagues: Rodolfo Previdi, Minh Nguyen, Blake Regan, Vince Ha-Hau and many others who were helpful in turning off from work as well as discuss any issues that arose throughout my PhD. I would also like to thank Simon White and Caleb Estherby for assistance in lab work and doing menial tasks as undergraduate students.

Finally, I must thank my family for the kindness, care and encouragement they have given me to ultimately finish my PhD candidature. It has been a long 4 years and the support they have provided is immeasurable. I want to specifically thank my wife for her immense patience with me for taking such an extended period to completion and am very grateful for her kindness and encouragement contributed, to be able to finish my work.

List of papers/publications included

Tai, M.; Gentle, A.; de Silva, K.; Arnold, M.; Lingen, E.; Cortie, M. Thermal Stability of Nanoporous Raney Gold Catalyst. *Metals (Basel).* **2015**, *5* (3), 1197–1211. https://doi.org/10.3390/met5031197.

Keast, V. J.; Wallace, J. W.; Wrightson, C. J.; Tai, M.; Gentle, A.; Arnold, M. D.; Cortie, M. B. The Effect of Vacancies on the Optical Properties of AuAl 2. *J. Phys. Condens. Matter* **2015**, *27* (50), 505501. https://doi.org/10.1088/0953-8984/27/50/505501.

Tai, M. C.; Gentle, A.; Arnold, M. D.; Cortie, M. B. Optical in Situ Study of De-Alloying Kinetics in Nanoporous Gold Sponges. *RSC Adv.* **2016**, *6* (89), 85773–85778. https://doi.org/10.1039/C6RA18272K.

Tai, M. C.; Gentle, A. R.; Arnold, M. D.; Cortie, M. B. Spontaneous Growth of Polarizing Refractory Metal 'Nano-Fins.' *Nanotechnology* **2018**, *29* (10), 105702. https://doi.org/10.1088/1361-6528/aaa639.

Gentle, A.; Tai, M.; White, S.; Arnold, M.; Cortie, M.; Smith, G. Design, Control, and Characterisation of Switchable Radiative Cooling. In *New Concepts in Solar and Thermal Radiation Conversion and Reliability*; 2018; Vol. 10759, p 107590L–10759–10.

Table of Contents

Certificate of Original Authorship i

Acknowledgements ii

List of papers/publications included iii

Table of Contents iv

List of figures viii

Abstract 1

1 Chapter 1 – Introduction 2

1.1 Motivation 2

1.2 Aims 2

1.3 Outline 3

2 Chapter 2 – Production of precursor alloys and nanoporous gold 5

2.1 Porous materials 5

2.1.1 Metallic Sponges 6

2.2 De-alloying method 6

2.3 Precursor alloy method and Au-Al results 10

2.3.1 Formation of nanoporous structures 12

2.4 Noble metal alloy results and discussion 13

2.5 Effect of defects and annealing on $AuAl_2$ optical properties 14

2.6 Structural characterisation of precursor alloys 18

2.7 Summary 21

3 Chapter 3 – Characterization and features of de-alloyed precursor alloys 23

3.1 Tuning the characteristics of nanoporous gold 23

3.1.1 Alterations in size of sponges after de-alloying 23

3.2 Optical properties 24

3.2.1 Surface structure 25

3.2.2 Pore size 25

3.2.3 Residual reactive metal 26
3.2.4 Applications for SERS 26
3.3 Metal oxide sponges 27
3.4 Structural characterisation of new metal sponges 27
3.5 Dynamic transmission technique to understand and optimise de-alloying kinetics 30
3.6 Optical properties of the nanoporous metals 35
3.7 Thermal stability of gold nanoporous sponges 39
3.8 Summary 44
4 Chapter 4 – Formation and morphologies of refractory metal 'nano-fins' 46
4.1 Fabrication of nano-fins 48
4.2 Analysis of nano-fins 49
4.3 Conditions for construction of nano-fins 50
4.3.1 Alterations of sputter energies during film deposition 50
4.3.2 Position of substrate 51
4.3.3 Gas pressures within sputter chamber 53
4.3.4 Choice of refractory metals to produce nano-fins 57
4.3.5 Variations of structure with growth times 57
4.3.6 Attempts at different combinations to replicate nano-fins 58
4.3.7 Necessity of co-sputter deposition 59
4.4 Summary 60
5 Chapter 5 – Properties of various as-deposited and selectively etched refractory metal nano-fins 62
5.1 Capacitance of the refractory metal nano-fins 62
5.1.1 Types of capacitors 62
5.2 Radiative cooling 63
5.2.1 Emissometers 64
5.3 Electrical measurements on Mo-Al and Ru-Al nano-fins 64
5.3.1 Capacitance and longevity 65

5.4 Temperature stability tests 65
5.5 Surface modifications on the nano-fins 66
5.6 Fabrication and oxidation process of VO_2 66
5.6.1 Preparation of vanadium thin films 66
5.6.2 Nano-fin V-Al 66
5.6.3 Oxidation of metallic precursor 67
5.7 Infrared optical analysis techniques 68
5.7.1 Infrared Ellipsometry 68
5.7.2 Thermal Emission measurement 68
5.8 Electrical properties of the nano-fins 69
5.9 Optical and thermal properties of refractory metal nano-fins and resultant etched nano-fin 71
5.10 Thermal stability of the Mo-Al nano-fins 71
5.11 Thermal stability of etched Mo-Al nano-fins 72
5.12 Transmission polarizability of the etched Mo-Al nano-fins 73
5.13 Optical analysis of uniform and nanostructured thin films of VO_2 75
5.13.1 In-air heated ellipsometry 75
5.13.2 Temperature Dependent Emissivity (via thermal emission measurement) 77
5.14 Summary 79
6 Chapter 6 - Conclusion 81
7 Appendix 84
7.1 Refractive indices 84
7.1.1 Water 84
7.1.2 Glass substrate 85
7.1.3 $AuAl_2$ 86
7.1.4 Nanoporous gold 88
7.2 SEM micrographs of attempted nano-fins 90
7.3 Capacitance within the Mo-Al nano-fins 90

7.4 Model fits to experimental data for Mo-Al nano-fins 91
7.5 s- and p- polarisation reflection data for Mo-Al nano-fins 92
7.6 Model fits for hot and room temperature planar VO_2 93
7.7 Model fits for hot and room temperature nano-fin VO_2 93
8 References 94

List of figures

Figure 1 Examples of two different types of gold sponge: a) produced from Au-Ag (36 at.% Au)[27], b) produced from Au-Al (34 at.% Au). 5
Figure 2 Outline of general steps taken to produce nanoporous metallic sponges from precursor alloys[10]. 7
Figure 3 TEM micrographs of gold sponge de-alloyed at temperatures a) -20°C, b) 0°C and c) 25°C[59]. Scales are the same as the one used in c). 8
Figure 4 Periodic table of elements of the metals used to produce metal alloys and the voltage differences between the metal and aluminium. 9
Figure 5 Left: Distinct purple-pink colour of $AuAl_2$ deposited at a) room temperatures, b) high temperature, right: SEM micrograph of the rough surface of the high temperature deposited $AuAl_2$. 14
Figure 6 Left: In situ ellipsometry (measured at 70°) taken of $AuAl_2$ within the Janis ST-400 UHV Supertran system, annealed to 600K. Blue lines correspond to lower temperatures and redder lines correspond to higher temperatures Right: ramping in situ heated ellipsometry with measurements taken at 70° at 1000 nm. 15
Figure 7 Comparison of a) ε1 and b) ε2, c) colour and d) reflectivity of the as deposited and the annealed thin film of $AuAl_2$[91]. 16
Figure 8 Variations in the colour of $AuAl_2$ depending on the type of the vacancy[91]. 17
Figure 9 Comparison of the reflection of RT and HT as-deposited films and 600 K annealed sample. 18
Figure 10 SEM micrographs of left: as-deposited $AuAl_2$ thin film and right: annealed $AuAl_2$ thin film of the same sample. All scale bars are 200 nm. 18
Figure 11 XRD spectra of a) as-deposited $AuAl_2$, b) $AuAl_2$ annealed at 330°C, c) high temperature deposited $AuAl_2$. 19
Figure 12 Above: XRD spectra of deposited samples with atomic percentages of gold a) HT [27.60%], b) 600K [34.01%], c) 39.91%, d) 36.02, e) 34.68%, f) 34.54%, g) 34.07%, h) 33.21%, i) 33.05%, j) 32.62%, k) 32.48% l) 32.38%, m) 31.02%, n) 30.43%, o) 28.52%. Below: refractive index, n, values for each corresponding $AuAl_2$ composition, matching colours in both figures refer to the same compositions. 20
Figure 13 Monte Carlo simulation of morphologies formed by various aluminium levels[1]. The percentages shown correspond to the atomic fractions of the 'active' metal. 23
Figure 14 Comparison of the dielectric constants between bulk and nanoporous gold[77]. 24
Figure 15 Coarsening of gold sponge (AuAl2 was deposited at approximately 300°C then de-alloyed in 0.1M NaOH for 1 min) from a) room temperature to b) 330°C [images from the present project]. 25

Figure 16 TEM micrographs of nanoporous gold sponges displaying the ligament and pore sizes[82]. . 28
Figure 17 SEM images of nanoporous refractory metal sponges and comparison of ligament shape and size to gold. 29
Figure 18 In situ dynamic transmission measurements taken of multiple samples in various NaOH concentrations[82]..... 31
Figure 19 a) Raw i*n situ* optical transmittance data obtained for various concentrations of etchant used to de-alloy the $AuAl_2$ thin films, b) the processed data after the raw data is fitted using Thin Film Toolbox[82]. 33
Figure 20 Effect of NaOH concentration on maximum de-alloying rates of AuAl2 (at room temperature)[82]. 34
Figure 21 a) The maximum etch rates at different temperatures of NaOH to de-alloy $AuAl_2$ thin films, b) processed etch rates of varying temperatures to determine the activation energy of the system[82]. 35
Figure 22 Comparison in reflectivity of a) different types of gold[7], b) nanoporous gold sponges from either RT or HT deposited precursor alloys. 36
Figure 23 Comparison of the a) optical constants (n and k) b) dielectric constants of etched RT and HT deposited $AuAl_2$ thin films 36
Figure 24 a) Reflection data of precursor refractory metal alloys and b) the resultant sponge after de-alloying. 37
Figure 25 Refractory metal sponges of a) niobium during de-alloying on glass, b) tungsten sponge on glass, c) tungsten sponge on a thermal oxide silicon substrate, d) niobium sponge on glass after the first colour change. 38
Figure 26 a) High temperature deposited $AuAl_2$ after etching in 0.1M NaOH, b) post annealed etched sample at 50°C, c) post annealed etched sample at 100°C, d) post annealed etched sample at 325°C [modified image from publication[1]]..... 39
Figure 27 a) Psi values of the etched HT deposited samples during *in situ* heated ellipsometry, b) full spectroscopic ellipsometry of the post anneal etched HT samples at specific temperatures. 40
Figure 28 a) thermal stability measured by the change in psi whilst annealing to 100°C, b) change in psi held at 100°C[1]. 41
Figure 29 Refractive index *n* and extinction coefficients of a) HT and b) RT deposited $AuAl_2$ sponge, dielectric constants of c) HT and d) RT deposited $AuAl_2$ sponge during in situ heated ellipsometry. . 43
Figure 30 Set up of the DC magnetron co-sputtering used to construct the nanostructured thin films[114]. All scale bars are 200 nm. 49

Figure 31 Shift in the area of nano-fin growth depending on sputtering energies for V/Al at V:0.2 A, Al:0.3 A (top) and V:0.25 A, Al:0.3 A (bottom). 50
Figure 32 Spread of nanostructures and formation of the nano-fins at a) plan view, b) tilted side view and c) tilted front/back view. Samples were produced with Nb/Al with increasing Al composition from left to right. 52
Figure 33 SEM images of 20 minute deposited nano-fin Mo-Al with their respective s- and p-polarised reflectance at angle 6° for nano-fins produced at gas pressures of a) 1. 5 mTorr, b) 2 mTorr, c) 2.7 mTorr, d) 3 mTorr, e) 3.5 mTorr, f) 5.5 mTorr. All scale bars are 500 nm. 54
Figure 34 Cross-section SEM micrographs of (a) 30 and (b) 40 minute growth times of Mo-Al nano-fins. Arrow indicates the direction of the aluminium flux. All scale bars are 500 nm[114]. 55
Figure 35 Nano-fins fabricated from a range of refractory metals. Each sample was deposited for 20 minutes, except for Ru (60 minute deposition) and W (30 minutes). All scale bars are 200 nm. 56
Figure 36 Cross section SEM micrograph of Ru-Al nano-fins deposited for 60 minutes. Scale bar is 500 nm. 57
Figure 37 SEM micrographs at (a) 15,(b) 20, (c) 30 and (d) 40 minute growth times of Mo-Al nano-fins. Arrow indicates the direction of the aluminium flux. All scale bars are 500 nm [modified image from publication[114]]. 58
Figure 38 a) Laser ablated lines on silicon substrate spaced apart by 50 µm and approximately 6 µm wide, c) lines after 20 minute deposition of the Mo-Al, b) cross section view of the ablated lines d) after deposition of the nano-fins. 59
Figure 39 Left: schematic of the electrical circuit constructed to measure the electrical properties of the supercapacitors. Right: zoomed in diagram of the supercapacitor. 65
Figure 40a) Experimental set-up of the annealing chamber for in situ monitoring of the oxidation process via reflection measurements. A graphite stage with an embedded heater and thermocouple are used to control the sample temperature. A fibre spectrometer was used to observe the change in reflection. b) In-situ reflection measurements on a 50 nm thin film vanadium on a silicon substrate at 450°C, c) In situ reflection measurements on nanostructured thin film vanadium-aluminium deposited for 30 minutes. d) In-situ reflection measurements on thin film vanadium on glass annealed at 550°C. 67
Figure 41 FTIR equipped with temperature stage, and polarizers allowing it to function as an ellipsometer. 68
Figure 42 Schematic of the emission based emissometer. 69
Figure 43 Left: comparison of the discharge in the samples over time, right: comparison of the cyclic voltammetry for the thin films. 70

Figure 44 SEM images and s- and p- polarized reflectance at angles 7°, 15°, 30°, 45° and 60° of Mo-Al nano-fins at a) as-deposited, b) 670°C and c) 750°C. All scale bars are 500 nm. 71
Figure 45 In situ raw ellipsometry data observed at various temperatures. 72
Figure 46 Reflection extinction ratios calculated from s- and p- polarized reflectance data scanned at 300-2500 nm between 10-70° at (a) 15,(b) 20, (c) 30 and (d) 40 minute growth times of Mo-Al nano-fins. 74
Figure 47 SEM micrograph (left), and the optimal transmission extinction ratio (right) of selectively etched nano-fins. Scale bar is 500 nm. 75
Figure 48: Hysteresis of the VO_2 films as measured by ellipsometry (2500 nm), lighter colour is the change in psi when cooling. 75
Figure 49: Normal incidence temperature dependent emissivity of (a) planar VO_2, (b-400 nm, c-800 nm, d-1200 nm) various thickness nanostructured VO_2 samples, showing some of the possible emittance profiles. 76
Figure 50: Angular dependent emissivity ε(theta) of planar VO_2, during heating from 35 to 80°C (left) and cooling from 80° back to 35°C (right) 77
Figure 51: SEM image of 100 nm thick Planar VO_2 (500 nm Scale bar) 78
Figure 52: SEM image of a typical nanostructured VO2 thin film on glass. (Scale bar 500 nm) 78
Figure 53: Angular dependent emissivity, showing the anisotropic response at high temperature of a typical 800 nm structured film. 79

Abstract

Nanostructured thin films have diverse optical, structural, electrical and/or magnetic properties. There are comparatively few methods to produce refractory nanostructures, so in this thesis we investigated the use of cosputtering for high temperature optical applications.

Precursor alloys were produced via deposition of aluminium paired with a less reactive metal (gold initially and then with refractory metals). A specific gold alloy, $AuAl_2$ was selected due to its unique optical properties. Colour changes were observed by annealing through in situ heated ellipsometry and when optical constants were compared to simulation results, gold and aluminium vacancies were the cause of the shifts in colour and optical properties in the alloy.

A popular technique in the formation of nanostructured materials is the selective removal of a less reactive metal called de-alloying. Sodium hydroxide was selected as the etchant to remove the aluminium in the alloys. This was employed to produce nanoporous gold and refractory metal. Though there is difficulty in knowing the complete dissolution of the aluminium within the thin films. Therefore, a simple and inexpensive process utilising optical transmittance was developed to optimise de-alloying times and understand the mechanisms behind the removal of aluminium. Three stages were apparent during the in situ optical analysis, initial depassivation, bulk dissolution and then delamination. Dissolution rates were linear with hydroxide concentration, and exponential with temperature, with an activation energy of approximately 0.5 eV.

Further characterisation of these sponges yielded interesting optical properties. In situ heated ellipsometry measurements indicated that gold sponges began to alter at temperatures below 50°C. At these temperatures coarsening of gold sponges was evident, with further coarsening occurring at approximately 150°C. Refractory metals substituted the gold and sponge variants were producible, though optically they resembled the resulting metal oxide. Extended de-alloying times and cracking of the films proved difficult, though structural examination demonstrated various morphologies were possible between refractory metals.

Another type of morphology was fabricated using DC magnetron sputtering and de-alloying of the resulting nanostructures to form ‘nano-fins’. The removal of the aluminium through selective dissolution enables the nanostructure array to transmit light. The polarization spans 500 to 1100 nm and the extinction ratio significantly increases to >100. The as-deposited nano-fins have high surface area with capabilities of limited charge storage and supercapacitor properties. When produced with vanadium, it can be oxidised to form VO_2 possessing a metal-insulation transition with the opposite effect to typical VO_2.

1 Chapter 1 – Introduction

1.1 Motivation

Nanoporous metallic structures possess a range of exciting qualities. They have potential for applications in areas as diverse as chemical sensors, supercapacitors, battery anodes, drug delivery substrates, chemical catalysis, and optical absorbers and emitters[1-6] due to the significant increase in the surface area. The present thesis is focussed on the latter possibility, and in particular on nanoporous structures that can operate at elevated temperatures.

Methods for fabricating nanoporous sponges are inexpensive and simple to reproduce on a large or small scale. The main method to produce sponges is through de-alloying or selective dissolution of a precursor alloy. Extensive research into the mechanical, optical and electrical properties of sponges composed of noble metals (e.g. Au, Ag, Pt) have been conducted[7-9]. Parameters that affect sponge morphologies have also been investigated for the noble metals[10-13]. However, comparatively little is known about refractory metal sponges, which will be addressed in this thesis.

Refractory metals are well known for their high temperature stability and corrosion resistant properties. These features of refractory metals have applications in biomedical implants[14] and fusion reactor walls[15]. Oxidation of these metals alters the electrical properties to become more semiconductor-like as well as changing the optical properties. A combination of oxide and metal are useful for capacitors[16] and gas sensors[17,18]. Refractory metals oxides have also been selected and fabricated with nanoporous networks, though most are produced through template methods[19] or anodization[20-23]. Selective dissolution is another method to constructing such nanoporous networks in metals[24], which is the main process that will be investigated in this thesis.

Further research into the properties of nanoporous refractory metal networks is required, in particular development of fabrication processes to produce functional morphologies as well as analysis techniques to determine the performance of such nanostructures.

1.2 Aims

The main objectives of this project were:

- To understand the formation and underlying properties of nanoporous sponges
- To optimise de-alloying times and removal of residual metal in the sponges
- To develop analysis processes to observe the optical, structural and thermal characteristics of various metal sponges
- To compare the properties of gold and refractory metal sponges

- To determine any interesting or novel properties of these nanostructured thin films.

1.3 Outline

This thesis begins with the fabrication of the precursor alloys and the required processes to form gold sponges, as a comparison point and pathway to production of refractory metal sponges. Conditions that must be satisfied in order to form the precursor alloys, as well as basic optical results are also discussed. Following this chapter are analyses of the gold and refractory metal sponges. Optical, structural and thermal characterisation of these thin film sponges is provided. In the next chapter, a new type of nanostructure called 'nano-fins' is introduced and parameters required for its optimal growth are discussed. An examination of the mechanism by which these structures are formed is presented. Finally, potential applications that arise from these new nanostructures due to the composition and structural features of the nano-fins are discussed.

CHAPTER 2 – PRODUCTION OF PRECURSOR ALLOYS AND NANOPOROUS GOLD

Published works featured in this chapter: Tai, M., Gentle, A., de Silva, K., Arnold, M., Lingen, E., Cortie, M., 2015. *Metals* (Basel). 5, 1197–1211. and Keast, V.J., Wallace, J.W., Wrightson, C.J., Tai, M., Gentle, A., Arnold, M.D., Cortie, M.B., 2015. *J. Phys. Condens. Matter* 27, 505501.

2 Chapter 2 – Production of precursor alloys and nanoporous gold

In this chapter, the techniques used to produce precursor alloys for gold and refractory metal nano-sponges are described. These nanoporous metal sponges possess interesting optical properties that are completely different to the bulk versions. The effect of variations of parameters (either during the fabrication of the alloys or post-deposition) on the optical properties of gold alloys and sponges will also be discussed. Finally, some basic characteristics of the precursor alloys will be analysed.

2.1 Porous materials

Fine-scale, porous materials have long been of great interest to scientific researchers. One important reason for this is the interactions they may have with molecules, ions and even atoms. More specifically meso-/nanoporous materials (generally classed as sponges with holes in the range 2-100 nm) have been considered very useful as they possess large surface areas and allow or inhibit the ability for movement of atomic scale particles[25]. Depending on the production method chosen, meso-/nanoporous materials can be formulated stochastically or in ordered arrays[9,26,27]. The uniformity or design of such substances also determines the properties. If the pores are of uniform size, for example, then these materials may be used for molecular sieving. Ordered structures give rise to a resonant plasmonic response which can lead to applications in SERS[28,29]. Alternatively, stochastic arrays possess a larger range of pore sizes and different types of morphologies can be produced. Figure 1 is an example of different stochastic morphologies that may be fabricated. However, the largest factor that affects the nanostructure characteristics is the composition of the material matrix. The meso-/nanoporous materials of key interest in this thesis are metallic sponges or foams. In this thesis they will be defined as sponges, though they may also be referred to as metallic foams, meso-/nanoporous metals or a mixture of these names[8,30-34].

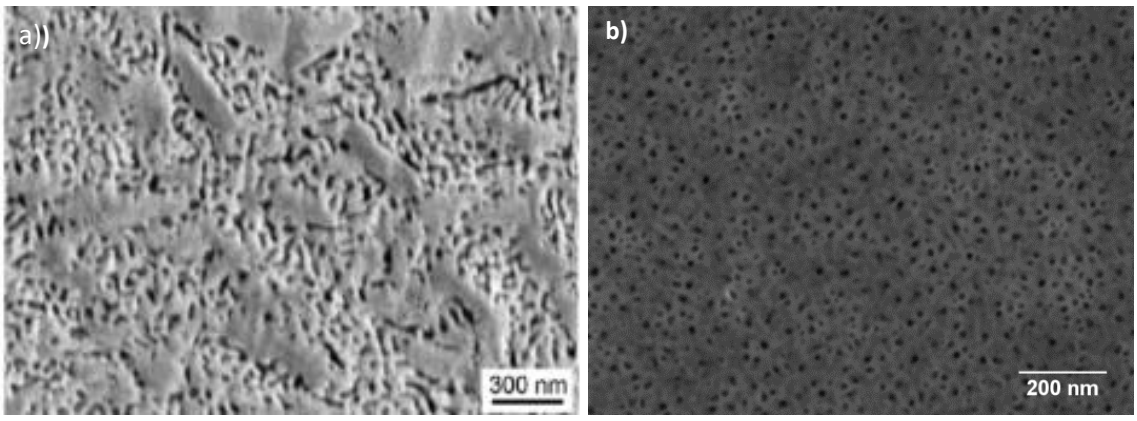

Figure 1 Examples of two different types of gold sponge: a) produced from Au-Ag (36 at.% Au)[27], b) produced from Au-Al (34 at.% Au).

2.1.1 Metallic Sponges

Multiple methods have been employed to manufacture sponges such as: template sacrifice/replication/space-holding method[35-37], powder metallurgy or sintering[38,39], anodisation[40,41], sol gel[42], hydrothermal[43] and de-alloying of alloys produced from PVD/sputtering[7,44-46], electrodeposition[47,48], melt spinning[49-51] or arc melting[12,52]. A method can be selected for the desired size or amount of meso-/nanoporous sponge required. Melt spinning or arc melting, for example, can be used to produce bulk sponges whereas anodization or PVD work best for thin films. Certain methods are more effective with specific metals due to the reactivity of the materials chosen. Therefore noble metal sponges are simple to produce with processes such as de-alloying, whereas anodization can be employed for more reactive metals that readily form oxides. Metals such as aluminium are used for anodization, as oxide layers can easily be formed when placed in an electrolyte solution under a constant voltage.

Sponges may have ordered arrays or holes or be random (stochastic). Ordered structures of metal oxides can be produced with controlled pore diameters through anodization, for example. Template sacrifice/replication/space-holding methods can be also used to produce ordered porous structures by 'filling' a template of microbeads or nanoparticles then removing the skeleton to reveal nanoporous materials. Colloidal lithography is one such technique which involves the use of nanoparticles to produce these types of nanostructures. Nanoparticles (polystyrene is a common particle chosen) are adsorbed onto the surface of a metal protecting the underlying material from ion beam etching. The nanoparticles are then removed to leave behind porous metal[53,54]. The random structure can be controlled by the salt concentration in the colloidal solution used to adhere to the surface of the material. This contrasts with most other methods (such as de-alloying) which develop stochastic morphologies and varied pore sizes. Reactive ion etching (RIE) can also be employed to produce voids in materials. One such process called 'the black silicon method' involves etching silicon in the presence of reactive gases to form voids between silicon 'spikes'[55]. Generally, however, de-alloying is the main source of production of metallic sponges due to the ease and control that it offers[48]. This method will be the main procedure discussed in this section.

2.2 De-alloying method

Various techniques may be exercised to construct precursor alloys for spongification. Spongification can occur in thin films or from bulk alloys[56]. Thin films are generally produced by physical vapour deposition (PVD) which is best suited for making films with thicknesses below 1 µm. Other processes must be used if thicknesses greater than 1 µm are needed. There are certain benefits and limitations associated with whatever technique is chosen. Fabrication of the alloy is only the beginning of the

spongification process: a subsequent de-alloying process renders the solid into porous sponge ready for application.

Figure 2 Outline of general steps taken to produce nanoporous metallic sponges from precursor alloys[10].

De-alloying is a method that allows for control over the pore sizes and achieves highly porous materials. Figure 2 displays the basic steps taken during selective dissolution of one element that readily produce 3D nanoporous structures of another element. This technique works through the removal of a more reactive metal in an alloy, where the alloy is made up of a less reactive metal and one or more reactive metal(s). The alloy is then placed within an alkali or acidic solution to enable the selective etching of the more reactive metal. Simultaneously as the reactive metal is etched away, diffusion of the non-etched metal atoms causes agglomeration[24,57,58]. These agglomerations form ligaments, commonly maintaining widths and spacings of around 1-10 nm. Therefore, two competing mechanisms promote the formation of the sponge: the first being the etching of the more reactive metal to increase surface roughness and pore formation, the other process is the surface diffusion of the noble metal to smooth and passivate[13] the surface. The physical mechanisms involved with de-alloying have yet to be fully understood, but studies comprising of simulated and experimental data have been conducted in an attempt to explain sponge formation. Erlebacher[57] has suggested that the surface diffusion at the metal-electrolyte interface: (1) moves the noble metal atoms out from porous zones, (2) smooths the surface through agglomeration and (3) creates variations in step edges.

Factors such as the de-alloying time[10], temperature[11], type[12] and concentration[13] of the solution used to selectively remove the reactive metal can affect the size of the pores and the resulting shape. Likewise, the composition[9] and type of the alloy also appears to alter the outcome of the morphology of the sponges for example in Figure 1. Several authors have proposed that these parameters affect the coarseness of the sponge. This is the case for increasing the de-alloying time as seen by El Mel et al[10]. They found that increasing the de-alloying time up to 300 minutes resulted

in larger pore sizes even across three different compositions of Au-Cu. Increasing the temperature of the electrolyte solution also results in coarsening of the nanoporous material as well as accelerating the de-alloying rate compared to a solution of the same concentration. By lowering the de-alloying temperature, pore sizes down to approximately 5 nm were achievable[59]. Figure 3 illustrates the change in pore sizes as the temperature is varied from room temperature to -20°C. This is consistent with the diffusivity of gold in a sponge given by:

$$D_s = \frac{d(t)^4 kT}{32\gamma t a^4}$$

where D_s is the diffusivity, t is the etching time, k is the Boltzmann constant, γ is the surface energy and a is the lattice parameter.

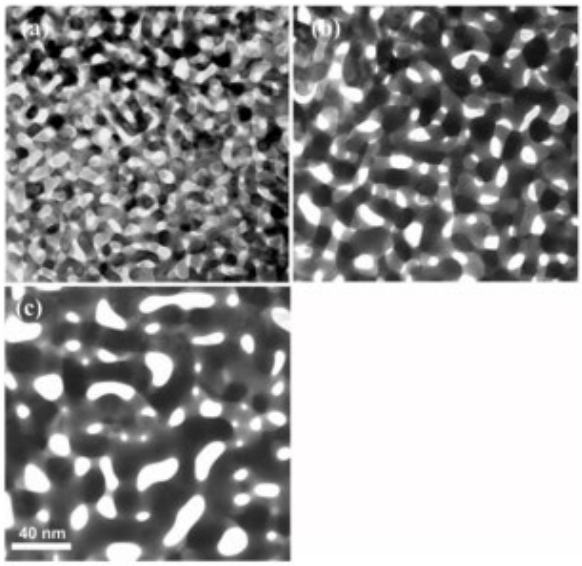

Figure 3 TEM micrographs of gold sponge de-alloyed at temperatures a) -20°C, b) 0°C and c) 25°C[59]. Scales are the same as the one used in c).

Other studies demonstrate that the nature of acid/alkali solution selected may affect the diameter of the pores for an amorphous precursor alloy. Rizzi et al. suggested a change in morphology between electrolyte solutions is purely based on the etch rate of the more reactive metal[12]. If the more reactive metal is quickly removed then the diffusivity of the more noble metal is then increased leading to coarsening.

Not only do variations in the electrolyte solution affect the morphology of the sponge but so too do the chosen metals and amount in the precursor alloy. A clear distinction between morphologies is evident in Figure 3. The sponge becomes less coarse as the atomic fraction of the noble metal is decreased. Supansomboon et al. were able to determine this coarsening and characterized it

through curvature, with high noble metal concentrations having more of a 'pin hole' appearance[9]. As the concentration of noble metal is decreased the sponge becomes a 'fibrous' type. Other studies have presented similar results[27,60]. A difference in morphology also seems to arise from the precursor alloy used before de-alloying. However, this disparity may be due to the other factors mentioned beforehand in addition to the alloy composition.

A minimum content of active metal is required in the alloy composition otherwise de-alloying does not occur: this is known as the parting limit. Alternatively, when electrochemically-assisted de-alloying is used, there may be a composition-dependent critical potential (E_c)[61].

Ideally, for de-alloying to occur:

i. The electrochemical potential difference between the two metals that the alloy is comprised of must be at least a few hundred millivolts
ii. The atomic percentage of the more reactive metal must be greater than the more noble metal
iii. The microstructure of the precursor alloy should be homogenous
iv. The speed of diffusion of the noble metal must be fast

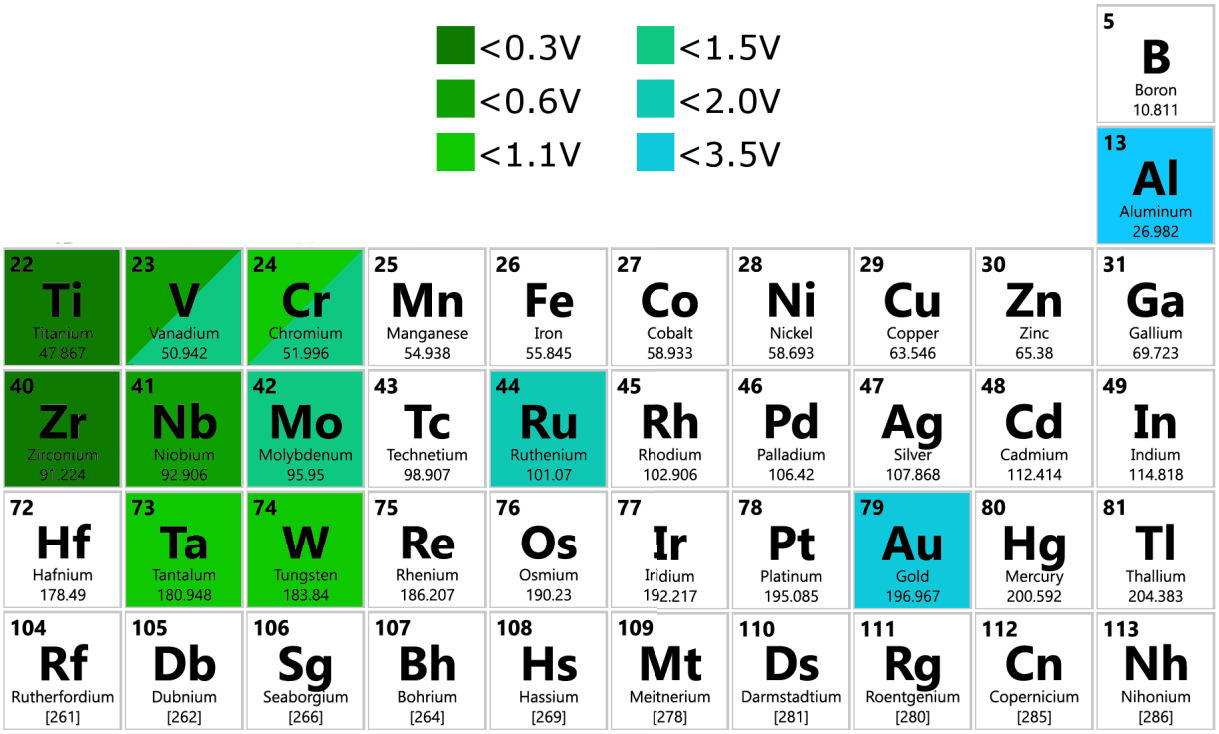

Figure 4 Periodic table of elements of the metals used to produce metal alloys and the voltage differences between the metal and aluminium.

Oxidant		Reductant	Standard Electrode Potential (V)	Difference of voltage to Al (V)
$Al^{3+} + 3e^-$	⇌	$Al_{(s)}$	-1.662	0.000
$Ti^{2+} + 2e^-$	⇌	$Ti_{(s)}$	-1.630	0.032
$Zr^{4+} + 4e^-$	⇌	$Zr_{(s)}$	-1.450	0.212
$Ti^{3+} + 3e^-$	⇌	$Ti_{(s)}$	-1.370	0.292
$V^{2+} + 2e^-$	⇌	$V_{(s)}$	-1.130	0.532
$Nb^{3+} + 3e^-$	⇌	$Nb_{(s)}$	-1.099	0.563
$Cr^{3+} + 3e^-$	⇌	$Cr_{(s)}$	-0.740	0.922
$Ta^{3+} + 3e^-$	⇌	$Ta_{(s)}$	-0.600	1.062
Tungsten			-0.580	1.082
$Cr^{3+} + e^-$	⇌	Cr^{2+}	-0.420	1.242
$V^{3+} + e^-$	⇌	V^{2+}	-0.260	1.402
$Mo^{3+} + 3e^-$	⇌	$Mo_{(s)}$	-0.200	1.462
$Ru^{3+} + e^-$	⇌	Ru^{2+}	+0.249	1.911
$Au^{3+} + 2e^-$	⇌	Au^+	+1.360	3.022
$Au^{3+} + 3e^-$	⇌	$Au_{(s)}$	+1.520	3.182
$Au^+ + e^-$	⇌	$Au_{(s)}$	+1.830	3.492

Table 1 Standard electrode potentials of the metals chosen to produce metal alloys with aluminium and the difference in the voltages compared to aluminium[62-69].

The rise in interest of sponges can be primarily attributed to their interesting mechanical[70] properties, applications in catalysts[1,2], use as capacitors[3], surfaced enhanced Raman scattering (SERS)[30,43,71], plasmonic applications[72-74] and possible applications in gas sensors[6,75-77]. Specific metals are selected for one or more of the applications listed above mainly due to the bulk properties of the metal. Hence, noble metals (Au, Ag, Pt) are chosen for catalytic purposes whereas transition metals (Ti, W, Mo, Nb) and their oxides are preferred for gas sensing applications or supercapacitors[78-81].

2.3 Precursor alloy method and Au-Al results

In this section precursor alloys in which the reactive metal is aluminium is discussed. The production of precursor alloys required the co-deposition of aluminium and noble metal of interest. Aluminium was chosen as the more reactive metal as it easily forms alloys with most metals, and is readily available, cost effective and can be removed easily. The properties of gold sponges made from such alloys is described in the present chapter. Although the fabrication of precursor alloys for making refractory metal sponges is discussed here, the properties of the refractory metal sponges made from aluminium alloys is left for later chapters. The gold sponge results have been published in *Metals*[1] and *RSC Advances*[82].

The gold sponges were made from a precursor comprised of the intermetallic compound $AuAl_2$. This bright purple substance is often known as 'purple gold' or 'purple glory'[83]. Successful fabrication of this 'purple glory' alloy was easily verified due to the bright pink-purple colour of the thin films. DC magnetron co-sputtering was used to make the precursor alloy thin films at base pressures better than 4×10^{-4} Pa (3×10^{-6} Torr). Sputtering was conducted in 2.7×10^{-1} Pa (2 mTorr) argon with 50 mm diameter gold and aluminium targets placed at a distance of approximately 100 mm from the substrate holder. Sputtering energies used during these depositions are displayed in Table 2, though these values varied due to degradation of the targets over multiple uses[82]. The substrates were at ambient temperature. $AuAl_2$ thin films were deposited on glass slides or silicon wafers. The samples on silicon wafers (with a 500 nm thermal oxide layer) were also used for scanning electron microscopy (SEM). The Si wafers had been sonicated in acetone then ethanol for 10 minutes and were also rinsed with de-ionized water then dried with nitrogen.

Metal	Current (A)	Voltage (V)	Power (W)
Aluminium	$0.360^{*}/0.300^{\wedge\#}/0.250^{\$}/0.220^{\%}$	$\sim400^{*}/\sim400^{\wedge}/\sim390^{\$}/\sim350^{\%}$	$\sim145^{*}/\sim120^{\wedge}/\sim100^{\$}/\sim80^{\%}$
Gold	0.042^{*}	$\sim350^{*}$	$\sim15^{*}$
Tungsten	$0.170^{\wedge}/0.250^{\$}$	$\sim360^{\wedge}/\sim350^{\$}$	$\sim60^{\wedge}/\sim90^{\$}$
Tantalum	$0.250^{\wedge}/0.200^{\%}$	$\sim320^{\wedge}/\sim300^{\%}$	$\sim80^{\wedge}/\sim60^{\%}$
Molybdenum	$0.250^{\#}$	$\sim320^{\#}$	$\sim80^{\#}$
Niobium	$0.250^{\wedge\#}$	$\sim330^{\wedge\#}$	$\sim83^{\wedge\#}$
Vanadium	$0.270^{\#}/0.300^{\&}$	$\sim330^{\#}/\sim330^{\&}$	$\sim90^{\#}/\sim100^{\&}$
Ruthenium	$0.200^{\#}$	$\sim350^{\#}$	$\sim70^{\#}$
Chromium	$0.250^{\#}$	$\sim330^{\#}$	$\sim84^{\#}$

Table 2 List of sputtering energies used for depositions, * energies used to produce $AuAl_2$, $^{\wedge}$ energies used to produce refractory metal sponges, $^{\$}$ energies used to produce W nano-fins, $^{\%}$ energies used to produce Ta nano-fins, $^{\#}$ energies used to produce the rest of the nano-fins, $^{\&}$ energies used for planar vanadium thin films.

A similar technique was used for the refractory metal alloys: W (99.99% purity), Ta (99.99% purity), Mo (99.99% purity) and Nb (99.95% purity) were co-deposited with Al (99.999% purity) by DC magnetron sputtering. The target dimensions were 50 mm x 3 mm (2" x 0.125") at a distance of 100 mm from the rotating stage. The base pressure of the sputtering chamber was better than 2.7×10^{-3} Pa (2×10^{-5} Torr). Argon flowed into the chamber with pressures at 3.6×10^{-1} Pa (2.7 mTorr) with varying sputtering voltages dependent on the refractory metal selected shown in Table 2. The composition target for these films were approximately 65 at.% Al and 35 at.% refractory metal. Heaters were also placed beneath the stage to deposit some samples at high temperature (HT). Two

1kW halogen lamps were placed between the stage and a reflecting casing to divert the heat towards the stage. Temperatures above 400°C could be achieved with this setup.

Energy dispersive X-ray spectroscopy (EDS) was conducted to verify the actual composition of the thin films after deposition. A Zeiss Evo microscope was used to perform the EDS measurements at 5 kV with multiple locations on the sample measured to ensure uniformity of the thin film.

The fabricated thin films were analysed using multiple techniques to discover the structural, optical and thermal properties of the alloys and their resultant sponges. Samples were structurally analysed using a Bruker D8 Discover XRD, Zeiss Supra 55VP SEM and FEI Tecnai T20 TEM. The equipment allowed the visualisation of the type of sponge formed, pore and ligament sizes, crystallinity, and alloy formation in the films. Optical properties were determined through fitting software, WVASE32, using ellipsometry and spectrophotometry data obtained from a J.A. Woollam V-VASE Ellipsometer, Perkin Elmer Lambda 950 and an Agilent Cary 7000 UMS. Ellipsometry measures the complex reflection ratios of,

$$\frac{r_p}{r_s} = \tan(\psi)e^{i\Delta}$$

where $\tan(\psi)$ is the amplitude ratio, and Δ is the relative phase shift, of the linear polarizations upon reflectance. The ellipsometer measures the reflected intensity at a range of polarizer and analyzer angles to determine the ellipsometric parameters. Psi is the amplitude ratio of the incident beam to the reflected beam and delta is the phase shift between the two. This ellipsometric data can then be analysed to yield more tangible optical properties, such as layer thickness and complex permittivity spectra. The response of parameterized optical models of the stack is fitted to the experimental data. The stack calculation is based on a matrix formulation of the fields as they propagate through specified layers. Bulk optical properties are parameterized via oscillator models, and then structure is incorporated in the form of effective medium models in layer stacks with graded density and/or composition. Additional spectrophotometer data was collected in the wavelength range 300-2500 nm at incident angles of 7°, to enable high quality estimation of effective material properties. This range was selected to match the range of the ellipsometer and 7° is the lowest angle the detector can be positioned without blocking the incident beam.

2.3.1 Formation of nanoporous structures

In this section the dissolution process will be discussed briefly with observed results of the nanoporous structures discussed later in the chapter. Nanoporous structures were produced by the selective removal of one metal constituent in the precursor alloys. Typically the aluminium was

mostly removed using NaOH solution which readily and easily dissolves aluminium. This leaves behind a spongy network of noble metal. For example, 0.1M NaOH de-alloyed $AuAl_2$ samples in a few minutes. The speed at which sponges were formed was vastly greater for gold than for the refractory metal alloys, therefore the concentration of the NaOH was increased to 1 or 2M for refractory metals and the temperature increased in some cases to 40°C. Despite this increase in concentration, the refractory metal samples still required a few hours to de-alloy. Careful timing was also necessary as excess or prolonged exposure of the alloys in solution could cause the metal to delaminate from the substrate.

Using an in-situ monitoring technique, optimal de-alloying times were determined and used to ensure most of the Al was removed during the etching process. This technique monitored the de-alloying process in cuvettes within a USB2000 Ocean Optics Spectrometer which repeatedly scanned the transmitted light at wavelengths of 300-800 nm. Sponge formation and monitoring will be detailed in the following chapter. For the remainder of the current chapter, the focus will be on the properties of precursor noble alloys.

2.4 Noble metal alloy results and discussion

Although this thesis is primarily concerned with metal nanosponges, the precursor alloy out of which the sponge was made is also of interest in some cases. This was particularly the case for the $AuAl_2$ precursors, which exhibited a rich and interesting set of properties. In particular, it was found that the optical properties of the precursor were controlled by the manner in which it was deposited. This phenomenon will be described in the next sections.

Alloys of gold possess unique colours ranging from yellow to red to pink to yellow-green. Some intermetallic compounds of gold, however, have even more vivid colours. One such compound is $AuAl_2$, commonly known as 'purple gold/glory/plague' with the name derived from its deep purple appearance[83]. The presence of this compound is readily determined just by eye. There has been some interest in using $AuAl_2$ to beautify objects such as jewellery[83]. This purple colour arises from the reflectance spectrum where there is a large decrease in the green region (~550 nm)[7,84,85]. This dip is attributed to a combination of interband transitions and a low energy bulk plasmon[86]. Further studies have shown that the compound possesses a dielectric function that can be considered for applications in plasmonics[87]. Strangely, $AuAl_2$ was initially considered as an unwanted compound ('purple pest') formed between Au and Al in electrical junctions which degraded the conduction and toughness leading to failure[88]. Although it is brittle, single-phase $AuAl_2$ displays structural and mechanical properties that are suitable for its use in coatings to shield materials prone to oxidation[89].

When $AuAl_2$ is deposited as a thin film coating at room temperature, the colour is initially a fainter pink or grey. It has been suggested that this faded colour is caused by defects[90] and vacancies[91] during deposition of the film. The vibrant colour is only exhibited once the film has been annealed or when the alloy is deposited at high temperatures[92] (HT). However, HT deposition of $AuAl_2$ causes crystals to form on the surface of the film producing rougher films[1,93], as depicted below in Figure 5.

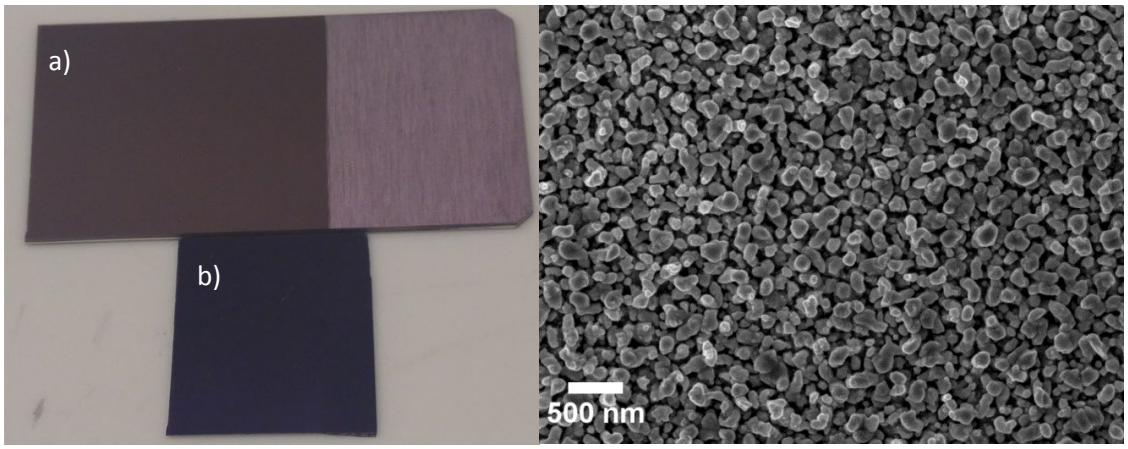

Figure 5 Left: Distinct purple-pink colour of $AuAl_2$ deposited at a) room temperatures, b) high temperature, right: SEM micrograph of the rough surface of the high temperature deposited $AuAl_2$.

2.5 Effect of defects and annealing on $AuAl_2$ optical properties

The reduced colour intensity of $AuAl_2$ that has been deposited at room temperature can be attributed to the defects that arise from sputtering the thin film. Removal of the defects by annealing led to development of the expected purple colour. This colour change was predicted using DFT calculations by varying types of defects/vacancies within the $AuAl_2$ structure (the DFT was conducted by Assoc. Prof. V. Keast) and compared to experimental results of the dielectric constants when annealed. A darker purple film was produced when the temperature within the chamber was increased to approximately 400°C. After HT deposition, the samples were left in the chamber to cool to prevent oxidation. The colours of the HT deposited sample and the room temperature (RT) sample then annealed samples differ. After annealing, the colour of the sample deposited at RT was enhanced but not to the dark purple in Figure 5. For comparison, the more pink-purple coloured slide displayed in Figure 5a) was sputtered at room temperature in the same conditions. The darker appearance of the sample deposited at high temperature was attributed to light scattered by the $AuAl_2$ particles shown in Figure 5, which is a different source of colour change than the removal of defects from annealing.

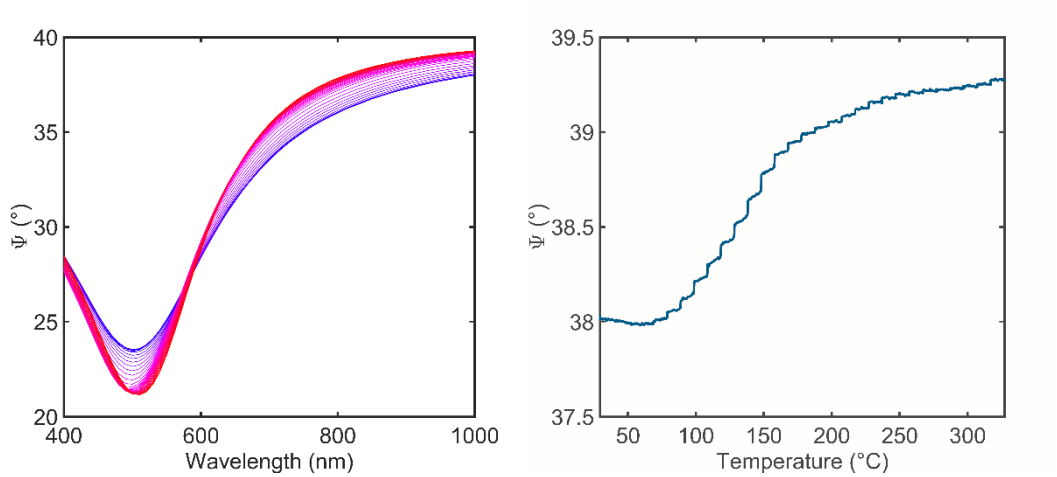

Figure 6 Left: In situ ellipsometry (measured at 70°) taken of $AuAl_2$ within the Janis ST-400 UHV Supertran system, annealed to 600K. Blue lines correspond to lower temperatures and redder lines correspond to higher temperatures Right: ramping in situ heated ellipsometry with measurements taken at 70° at 1000 nm.

An $AuAl_2$ sample was annealed within a Janis ST-400 UHV Supertran chamber at pressures better than 10^{-7} Torr. The temperature was elevated from room temperature to 600K and spectroscopic ellipsometry measurements taken when the temperature stabilised. A full spectroscopic scan was conducted between 300-2500 nm in 10 nm intervals at 65-75° at every 10K steps. Psi was measured in 30 second intervals during the annealing process at 1000 nm at an angle of 70°. Figure 6 illustrates the changes in psi of $AuAl_2$ as the sample was annealed to 600K. These changes in psi over the annealing process are related to the more apparent purple-pink colour of $AuAl_2$ and the decrease in the trough at approximately 550 nm is related to the reflectivity dip in Figure 7. This raw data was then used to calculate the ε1 and ε2 found in the figures below. These results were published in *Journal of Condensed Matter Physics*[91].

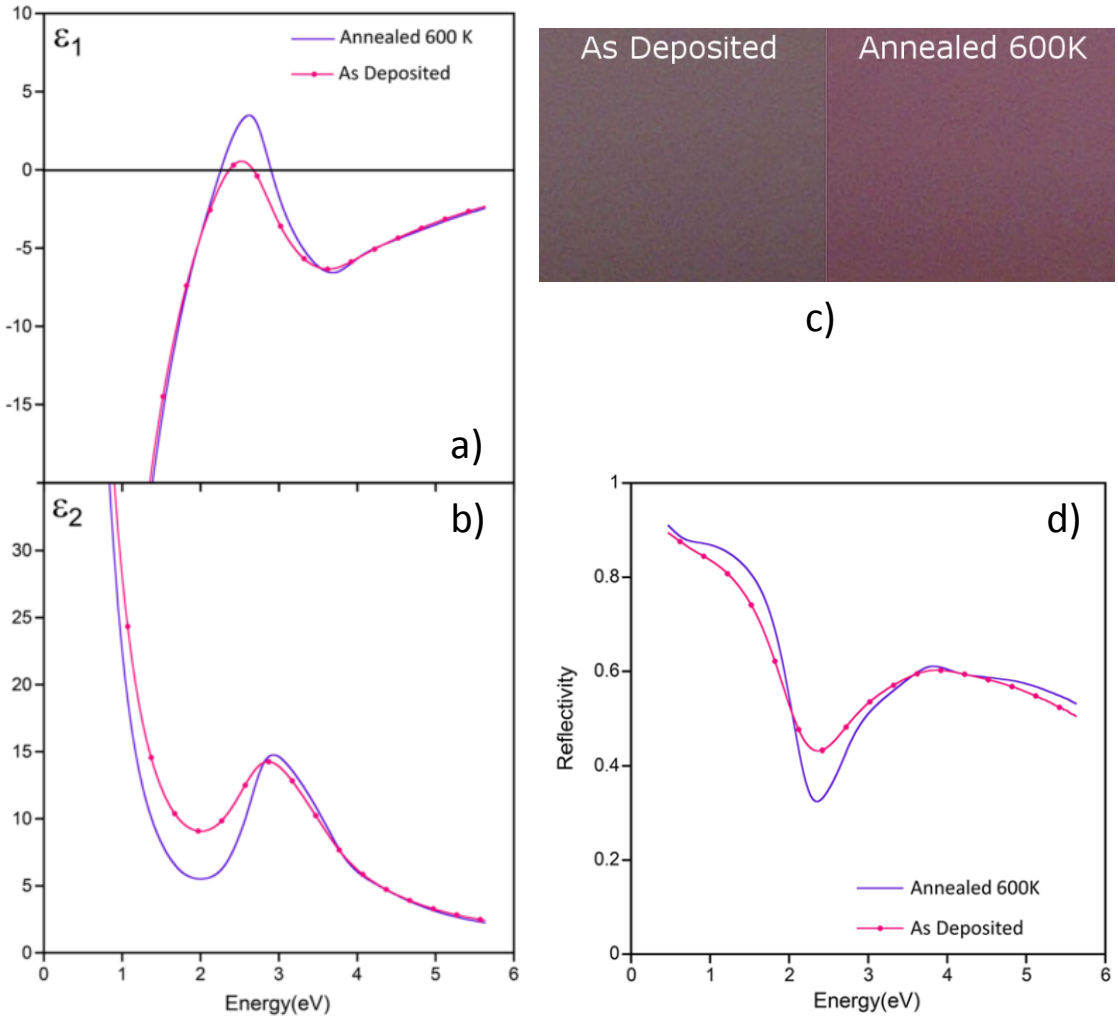

Figure 7 Comparison of a) ε1 and b) ε2, c) colour and d) reflectivity of the as deposited and the annealed thin film of $AuAl_2$[91].

ε1 and ε2 shown here and later on in the chapter are the real and complex relative permittivity. The changes in the energy dip in the reflectivity spectrum are associated with different vacancy types. In this study, both Al and Au vacancies were investigated, as well as the colour change associated with the changing vacancy. It was revealed that the dip at around 2.2eV decreases as the $AuAl_2$ sample was annealed Figure 7.

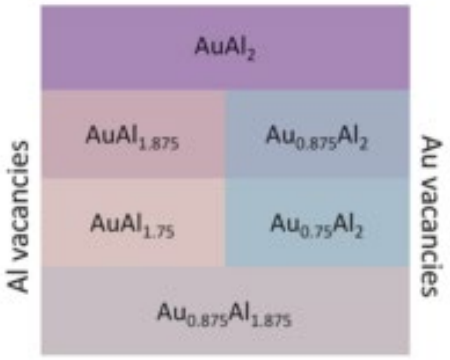

Figure 8 Variations in the colour of $AuAl_2$ depending on the type of the vacancy[91].

The thin film sample produced was composed of 65.9 at.% Al and 34.1 at.% Au (or $AuAl_{1.93}$) and satisfactorily matched the DFT calculated optical properties of $AuAl_{1.85}$. After annealing the sample to 600 K, the thin film sample becomes very similar to the expected, vacancy-free $AuAl_2$. This change in colour demonstrates that the presence of vacancies will influence the colour of sputtered thin films. In Figure 8 a pinkish hue is correlated with Al vacancies where as a blueish hue correlates with Au vacancies. These colours can be readily seen by the human eye and serve as a convenient check on the quality and stoichiometry of $AuAl_2$ thereby reducing the need for performing a more laborious technique such as EDS. The similarities between the as-deposited film and the calculations for the case of an Al vacancy suggest that the sputtered thin films were similar to that of ones produced by Furrer et al. In their investigation, the films displayed similar flattening of the reflectivity dip[90]. They also conducted Au ion irradiation which caused a downwards shift in energy at the reflectivity dip, indicating similar results to what was found by Keast et al. Calculated energies of vacancy formation further suggest the as-deposited films contain Al vacancies as these possess lower energies than Au vacancies.

A comparison of the different types of $AuAl_2$ samples is provided in Figure 9 and it should be noted that the compositions of gold and aluminium for the HT (27.60 a.t.% Au) and RT (34.07 a.t.% Au) deposited films differ, however they do both appear purple. The difference arises due to the surface roughness from deposition of Au and Al at elevated temperatures, which produces a darker purple film.

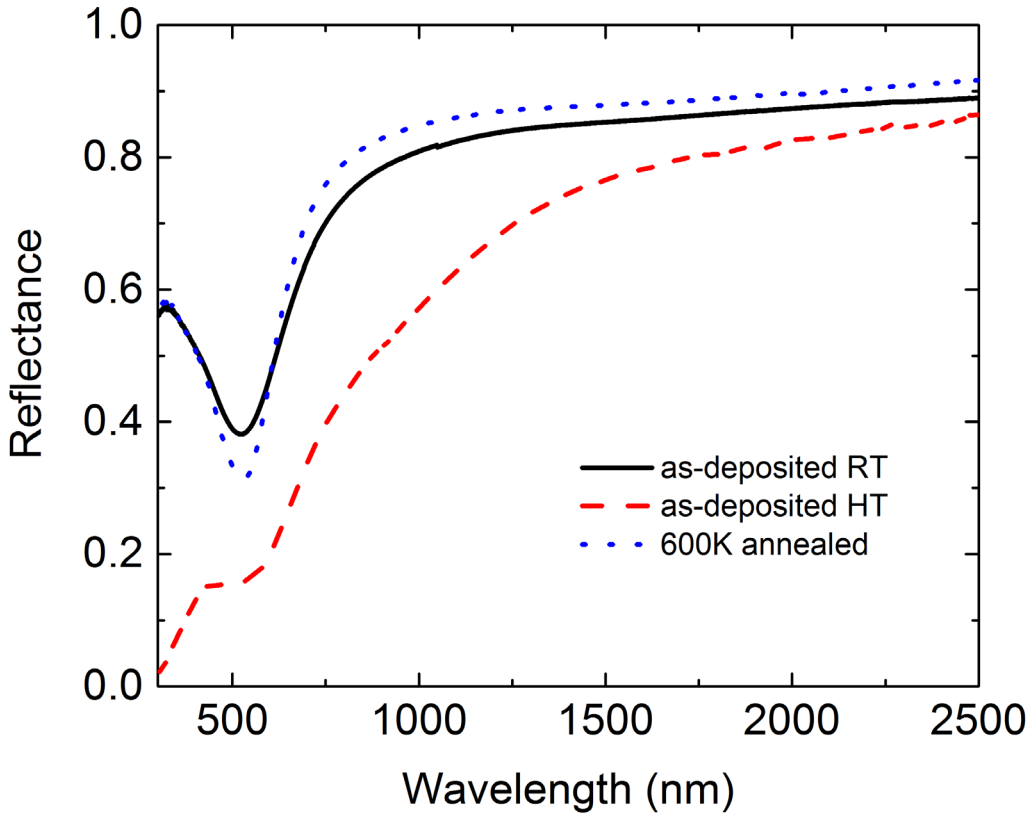

Figure 9 Comparison of the reflection of RT and HT as-deposited films and 600 K annealed sample.

2.6 Structural characterisation of precursor alloys

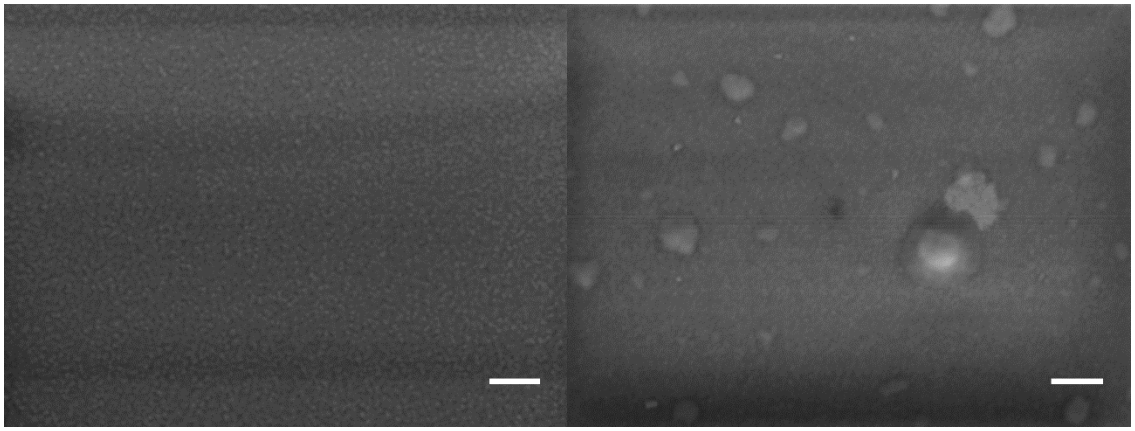

Figure 10 SEM micrographs of left: as-deposited $AuAl_2$ thin film and right: annealed $AuAl_2$ thin film of the same sample. All scale bars are 200 nm.

The $AuAl_2$ films fabricated were uniform as deposition occurred on a rotating stage. This method produces equal thickness films in all areas. Figure 10 conveys the uniformity of these films even when annealed to 600 K. The small grains can be seen in the left image of Figure 10 where as for the

right image, larger aggregates appear to have formed. As mentioned before, the colour of the films can be changed by heat treatment due to removal of vacancies and defects. Through annealing the sample has become more reflective at wavelengths >550 nm, and the dip has deepened and blue shifted.

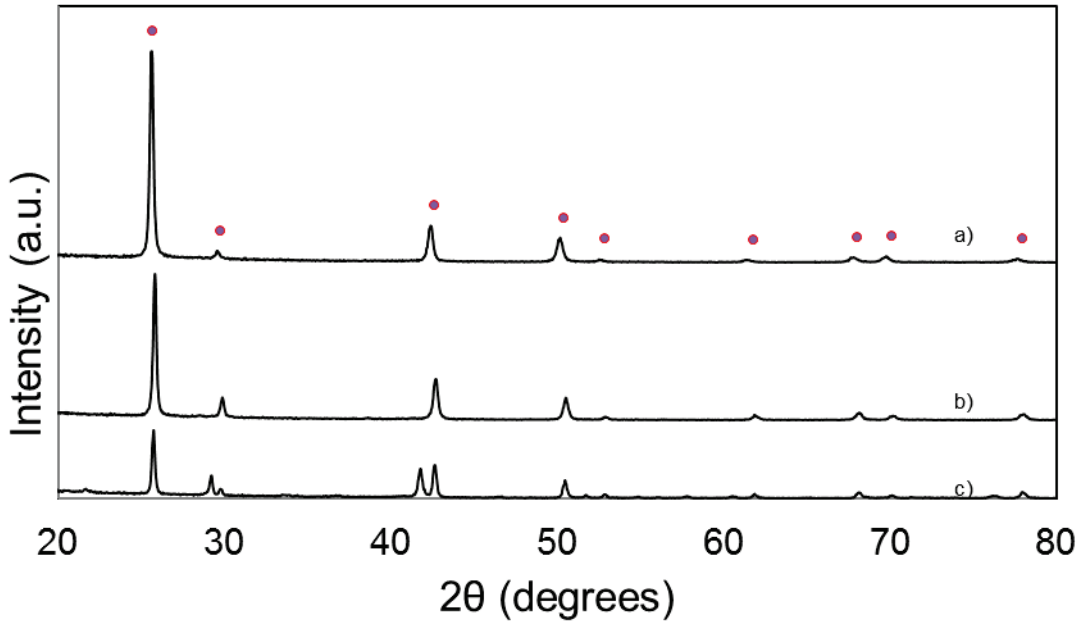

Figure 11 XRD spectra of a) as-deposited $AuAl_2$, b) $AuAl_2$ annealed at 330°C, c) high temperature deposited $AuAl_2$.

The XRD diffraction spectra in Figure 11 illustrates the presence of $AuAl_2$ in as-deposited samples. When the deposited samples were annealed, producing a change in colour, the diffraction peaks remained the same with slight broadening of the peaks. The significant difference is in the high temperature deposited samples possessing additional peaks. An analysis of the additional peaks by Prof. M Cortie indicated that the new phase was cubic with a lattice parameter of about 3.06 Å and a presumed p m -3 m space group. It does not match any of the known phases in the Au-Al phase diagram and may correspond to a previously unknown phase formed only at relatively high temperatures.

However, an analysis of the optical properties of various $AuAl_2$ samples with different compositions of gold and aluminium did not exhibit any consistent trends that occurred as the accelerating voltages were decreased for aluminium, which increased (or decreased) Al content in the alloys. In Figure 12 the corresponding refractive index, n values for the XRD measurements are depicted with most of the samples possessing a peak in between 450 and 500 nm as well as varying in position, intensity and broadness. The 600K sample, having been annealed and discussed previously with a colour most similar to $AuAl_2$ exhibits a much sharper and narrower peak at approximately 450 nm. In

comparison, other compositions possess different *n* values to those of the 600K sample, either with a lack of a peak in the 450 nm region or a lesser peak towards 500 nm.

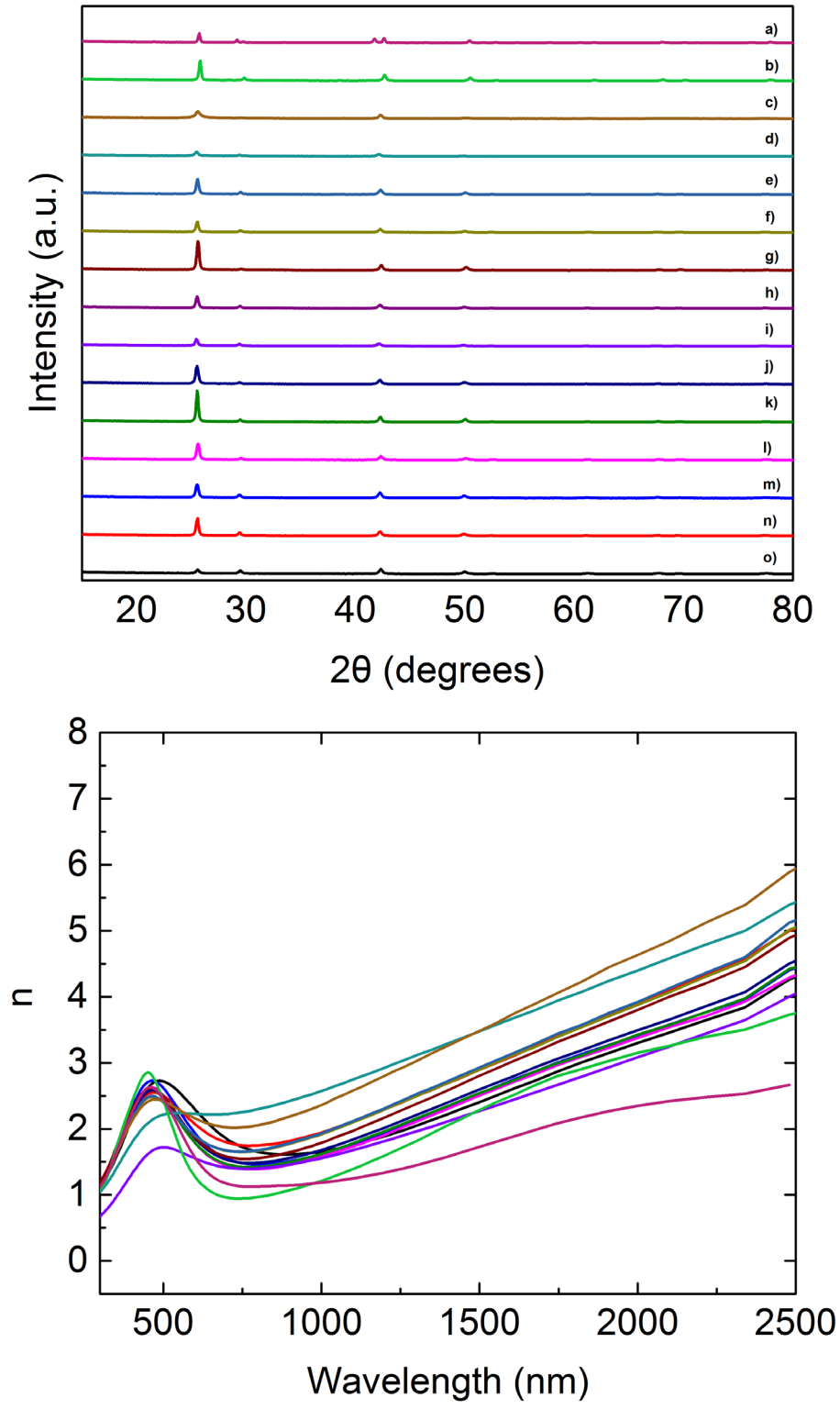

Figure 12 Above: XRD spectra of deposited samples with atomic percentages of gold a) HT [27.60%], b) 600K [34.01%], c) 39.91%, d) 36.02, e) 34.68%, f) 34.54%, g) 34.07%, h) 33.21%, i) 33.05%, j) 32.62%, k) 32.48% l) 32.38%, m) 31.02%, n)

30.43%, o) 28.52%. Below: refractive index, n, values for each corresponding $AuAl_2$ composition, matching colours in both figures refer to the same compositions.

The optical technique described previously in Experimental Methods was used to find optimal de-alloying times for the $AuAl_2$ and the refractory metal precursors. The increase in de-alloying times for the refractory metals may be mostly attributed to the low diffusion rates of these metals, which restricted access and movement of the NaOH ions to etch the aluminium within the alloy. However, the correct alloy composition was required to avoid complete etching and removal of the thin film layer from the glass slide. If aluminium concentration was too great the de-alloying time would reduce, but the thin film was more likely to detach itself from the glass slide. Conversely, with too little Al, de-alloying would not occur or the resultant sponge would contain small or non-existent pores. If the thin films were de-alloyed for too long, detachment of the film from the substrate occurs but if the film remains, there was a chance of most of the film to be cracked apart.

2.7 Summary

Spongification of precursor alloys requires specific conditions to be met. This work has confirmed that $AuAl_2$ is a very suitable precursor for making nanosponges as it is readily prepared and simple to recognise due to its colour. Production of thin film alloys through magnetron co-sputtering can be further refined through annealing, thereby further developing the purple-pink colour of the thin films. Changes in the optical properties of these alloys may be observed through ellipsometry and relate to movement of vacancies and defects. Refractive metal sponges were also fabricated with the same method used for $AuAl_2$ samples, though stronger concentrations of NaOH were used as the diffusion and etch rates were considerably reduced.

CHAPTER 3 – CHARACTERIZATION AND FEATURES OF DE-ALLOYED PRECURSOR ALLOYS

Published works featured in this chapter: Tai, M., Gentle, A., de Silva, K., Arnold, M., Lingen, E., Cortie, M., 2015. Metals (Basel). 5, 1197–1211. and Tai, M.C., Gentle, A., Arnold, M.D., Cortie, M.B., 2016. RSC Adv. 6, 85773–85778.

3 Chapter 3 – Characterization and features of de-alloyed precursor alloys

The primary themes of this chapter are the optical and morphological properties of metallic sponges. The optical properties are of interest due to the change in colour of the sponges (e.g. gold sponges appear dark or in some cases almost black compared to the colour of bulk gold) and the ability to change that colour by controlling the morphology. Optimisation of the optical and structural characteristics and applicability of SERS for gold sponges as well as metal oxide sponges will be discussed in this section.

3.1 Tuning the characteristics of nanoporous gold

Various morphologies may be produced during or post fabrication of the metallic sponges. Figure 13 depicts simulations of various morphologies produced by altering the initial composition of the precursor alloy.

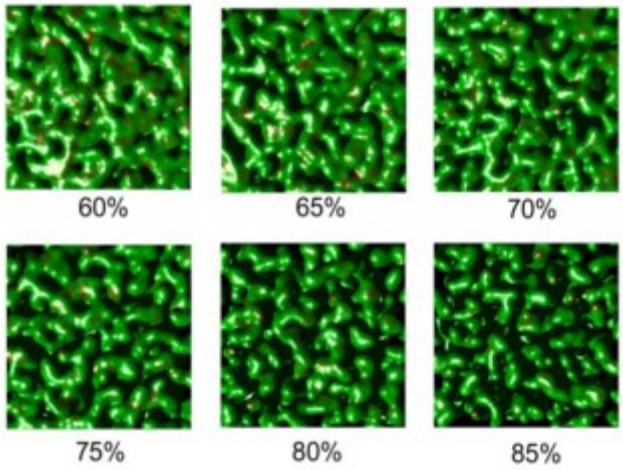

Figure 13 Monte Carlo simulation of morphologies formed by various aluminium levels[1]. The percentages shown correspond to the atomic fractions of the 'active' metal.

3.1.1 Alterations in size of sponges after de-alloying

During the de-alloying process, the thickness of the alloy precursor may decrease[94]. Studies suggest that within the de-alloying process, surface diffusion may not be the most significant mechanism which leads to shrinkage as the movement of atoms from the bulk to the surface begins to decline. Therefore shrinkage would cease once dissolution has reached deep into the material. Alloy contraction, if it occurs, can reach up to 30 vol.%, but it does not occur to that extent in all cases[13,51]. Studies have indicated that the volume of the sponge can be relatively unchanged through electrochemical methods. Senior et al. successfully maintained the mechanical integrity of a gold sponge through optimisation of the Au-Ag composition, de-alloying potential and the electrolyte

temperature[95] while Sun et al. were able to produce bulk gold sponge at the millimetre scale with no major cracking and no volume change[96]. This was only achieved a few microns into the surface of the alloy as further de-alloying caused cracks to appear. A two-step galvanostatic de-alloying method was established in a solution of diluted acid for up to 70 hours before being placed into stock acid solution for another 10 hours. The potential during the galvanostatic etch imposed the oxidation of gold which in turn allowed surface diffusion to prevent tensile stresses and cracks to arise[96]. In another study, Sun et al. produced nanoporous gold with no cracks, in the form of thin films as opposed to their previous work with bulk gold sponges[97]. Various parameters can be controlled to produce sponges with desired properties.

3.2 Optical properties

The study of sponges has been ongoing for decades due to the unique properties and functionality of the material. Research has been conducted on the mechanical, electrical, morphological and optical properties of sponges. Introducing porosity into a metallic system in the form of sponges yields interesting optical properties.

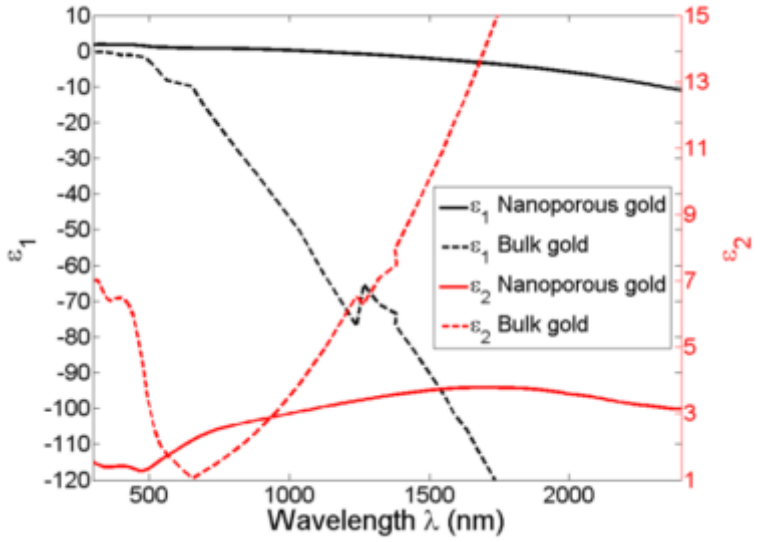

Figure 14 Comparison of the dielectric constants between bulk and nanoporous gold[77].

Many metal sponges are dark coloured regardless of the colour of the solid precursor. For example, for $AuAl_2$ the alloy appears purple to the eye but when de-alloyed the colour can change to very dark, almost black[33]. This is similar for $PtAl_x$ as a flat spectral response is displayed for the reflectance for mesoporous gold and platinum[7]. Bulk gold generally is highly reflective as opposed to the highly absorptive nature of nanoporous gold at long wavelengths. A common explanation for the absorption is a distribution of localised plasmon resonances (due to a distribution of local

morphologies) which is particularly prominent at long wavelengths[98]. Comparing the dielectric constants of bulk and nanoporous gold, Figure 14, reveal that at wavelengths in the visible range, nanoporous gold has values close to zero for ε_1. However, as the wavelengths move towards the near infrared region nanoporous gold becomes more metal-like. In this wavelength region (<1700 nm) ε_2 is also significantly smaller for nanoporous gold than in bulk gold[77].

3.2.1 Surface structure

Surface structures contribute to the overall optical properties of sponges, factors such as roughness and porosity cause different effects depending on the magnitude of these properties. The roughness of the sponge can also affect the optical effects of the material. Surface plasmons may arise due to the nanostructure or surface roughness, not only from the porosity of the sponge[73]. Sardana et al. formulated gold sponges to determine the relationship between porosity and plasmonic response. Control of the porosity can affect the surface plasmon polariton (SPP) dispersion relation[28]. Nanoporous gold possesses features from both bulk metal films with propagating surface plasmon resonance (SPR) excitations and nanoparticles with localised SPR excitations[99]. Tuning of the porosity can also alter the complex refractive index *n* and *k*[100]. Spectroscopic and ellipsometric data were compiled and a Lorentz-Drude model used to fit the results. It has also been found that when samples are deposited at high temperatures, the alloys as well as the sponges possess surface roughness and scatter visible light.

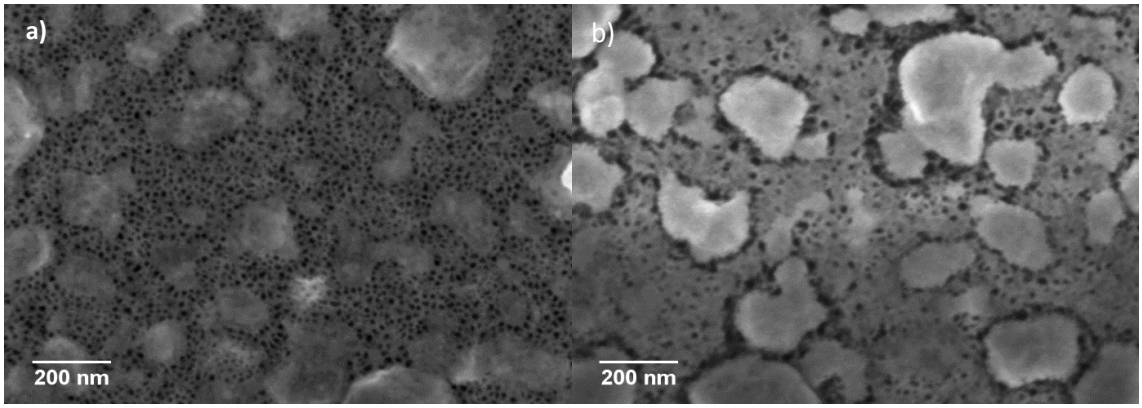

Figure 15 Coarsening of gold sponge (AuAl2 was deposited at approximately 300°C then de-alloyed in 0.1M NaOH for 1 min) from a) room temperature to b) 330°C [images from the present project].

3.2.2 Pore size

Managing pore sizes are essential for optimising the optical properties of sponges[101]. Other studies have found experimentally and computationally, that the ligament-to-pore-size ratio affects the plasmonic peaks of gold sponges. A link was observed between the increase in ligament diameter and a red-shift at long wavelengths in the transmission spectra[102]. However, once ligament sizes

increased further, a blue-shift occurred. Therefore control over the morphology of the sponge greatly affects the optical response. Post-annealing of gold sponges coarsen the material and also affects optical properties such as the optical constants, n and k[1]. Figure 15 is an example of coarsening after the material has been de-alloyed, however, it appears that a complete dissolution had not occurred as crystals can be seen which are possibly made up of the precursor alloy.

3.2.3 Residual reactive metal

Even residual reactive metal leftover from incomplete de-alloying can result in changes to the absorption spectra[101]. The residual metal can also affect the properties of the sponge, including applications of the SERS effect[103]. This was tested by de-alloying Au-Ag with varied levels of excess Ag within the sponge. Adjusting de-alloying conditions also alters the pore sizes. In order to rectify this, the gold sponges were annealed to increase the pore sizes but not at temperatures high enough to increase surface roughness. A higher SERS signal was obtained for samples with greater amounts of remaining silver.

3.2.4 Applications for SERS

Nanostructured noble metals are of interest for use in SERS due to their SPRs and this is also evident for sponges. For example SERS enhancements of up 10^5 for rhodamine 6G (R6G) and greater than 10^6 for crystal violet (CV) have been achieved on gold sponges. The pore size was at a minimum (5-20 nm) for these intensities to occur[71] which is in contradiction to Kucheyev et al. who had previously suggested that a relatively large average pore size of approximately 250 nm would provide the greatest enhancement[29]. Nevertheless, the current view is that reduction of pore size increases the SERS signal. There is also a realisation that roughness is the main factor that causes an enhancement[71]. Similar to roughness, Qian et al. showed a signal increase in nanoporous gold through fracturing the surface[104]. Roughness was simulated by slicing the surface of the sponge with a micrometer knife to produce 5-10 nm protrusions and ligament tips. This was compared with a sample that had gold nanoparticles deposited onto it and they determined that the enhancement was similar. It can be concluded that the enhancement effect arises from nanosized protrusions from the nanoparticles/ligament tips. This may explain why a more intense signal was found by Kucheyev et al. even though pore size was increased.

However, pore size may not be the only factor that affects the SERS effect in nanoporous metals. Optimisation of both the ligament and pore size can lead to even greater SERS intensities[105]. This paper revealed that the electroless plating can increase ligament size as well as decrease pore size in gold sponges. Though an enhancement was produced when the pore size to ligament ratio was lower than 1, the pore size dependence only occurred for the 514.5 nm laser not when it was

changed to a 632.8 nm laser due to plasmon excitation from the laser. Other factors have been tested to determine whether they affect the SERS enhancement in nanoporous gold[106]. Studies have indicated that measurement temperature plays a role in the signal enhancement in gold sponges. A temperature range from 80K to 300K was measured in conjunction with Raman scattering and a greater signal was obtained from lower temperatures. No peak shifts were apparent either which meant that the R6G spectrum was unchanged during the temperature variations. Thus, the largest enhancements transpire when the temperature is low, the surface is rough and when the pore size to ligament ratio is small.

3.3 Metal oxide sponges

Most metal sponges can be readily oxidized and these oxide sponges possess interesting optical applications. For example, nanoporous titania (TiO_2) has a substantial bandgap and hence does not absorb in the visible wavelength range, and was assessed as non-emissive colour filters in conjunction with photo-excited dye molecules (Alizarin, Alizarin Red, Purpurin, Fluorescein, Fluorescein Disodium Salt (FDS) and Eosin Y). Ultrafast electron-transfer between the dye and the nanoporous material was able to supress the autofluorescence of the dye[107]. Other selective filters have also been investigated using Indium Tin Oxide (ITO). By producing stacked layers of nanoporous and dense ITO, specific wavelengths in the visible region were reflected and specific wavelengths were transmitted[108]. By increasing the number of stacks of nanoporous and dense ITO, the performance of the red, green and blue colour filters could be increased. However, metal oxide sponges are more typically exploited for their high surface area and electrochemical capabilities. For example, nanoporous transition metal oxides have been widely selected as sensors for hydrogen[76] or nitrogen dioxide[6] gas due to the abundance of oxidation states that these metals possess, which can cause adsorption of the gas molecules to the surface of the metal oxide.

3.4 Structural characterisation of new metal sponges

Much of the literature surveyed so far has focussed either on noble metals (particularly for plasmonics applications), or on catalyst metals. High-temperature operation of these sponges is yet to be extensively investigated. This next section will focus on high temperature properties and how the spongification techniques developed for the noble metals can be applied to refractory metals. Recipe variations were necessary for successful production of these sponges and analysis of the resulting morphology were captured using the Zeiss Supra 55VP SEM and FEI Tecnai T20 TEM.

Since noble metal sponges are the starting point of the investigation, the structure of the gold sponges produced will first be described, before going on to outline the other types of sponges.

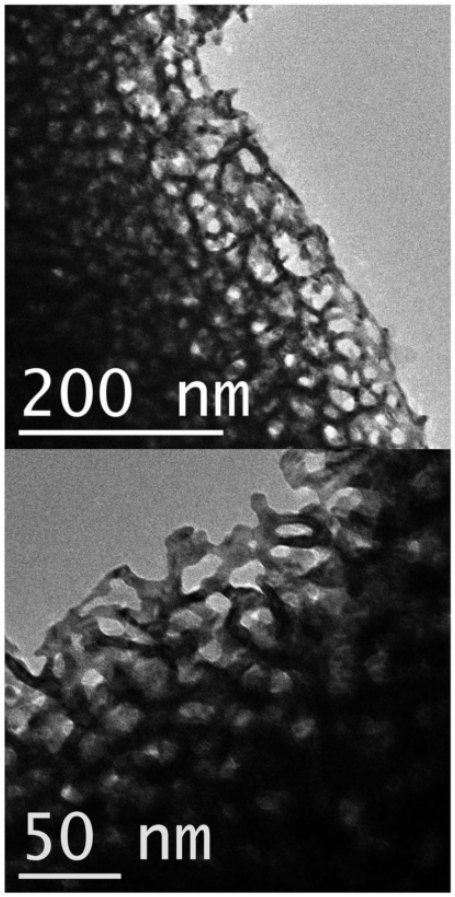

Figure 16 TEM micrographs of nanoporous gold sponges displaying the ligament and pore sizes[82].

As seen in Figure 16, pore sizes of the gold sponge were approximately 20 nm in diameter with ligament sizes of 5 nm. Samples were specially prepared by de-alloying the samples until the film had detached from the surface of the substrate. The floating film in solution was flushed with deionised water before being 'scooped' onto lacey carbon TEM grid. Multiple grids were prepared in case the thickness of the floating sections of the film were too thick to be viewed under the TEM.

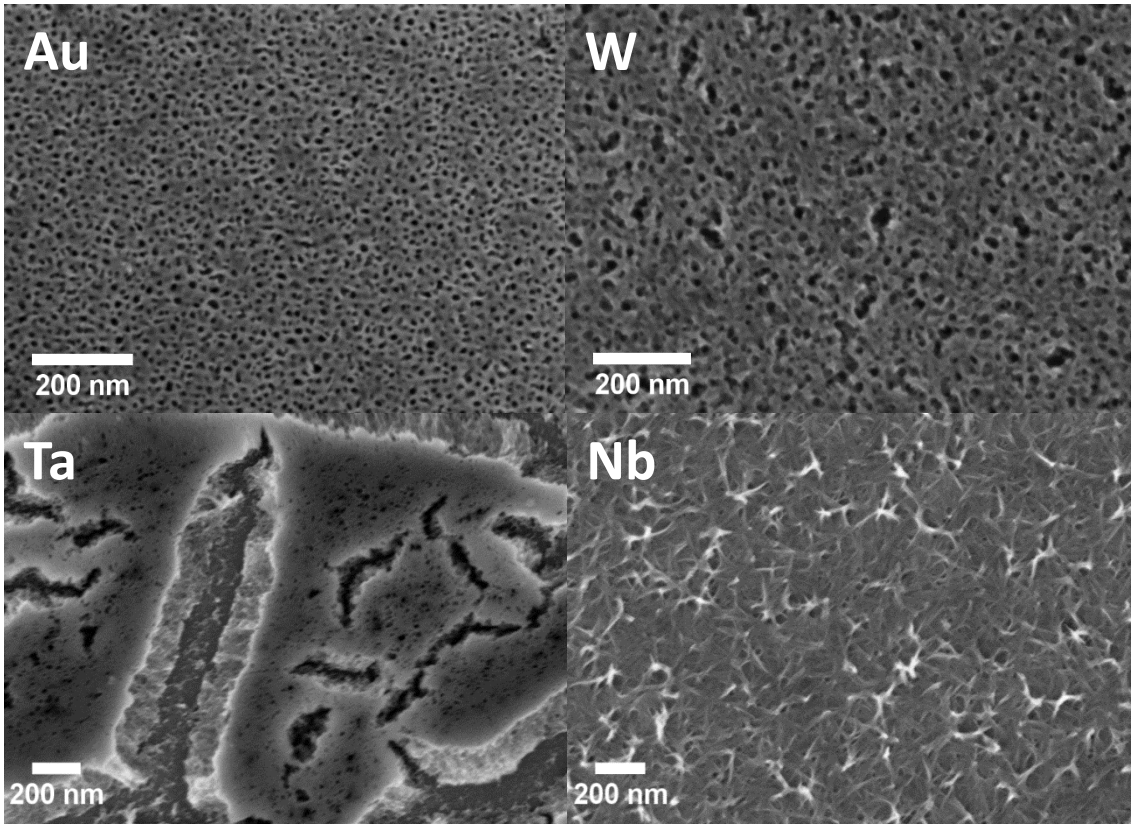

Figure 17 SEM images of nanoporous refractory metal sponges and comparison of ligament shape and size to gold.

As mentioned before, the nanoporous metals were formed through chemical etching with NaOH. Firstly to confirm this process would occur the electrochemical potential differences between the refractory metals and aluminium were checked and found to be greater than a few hundred millivolts suggesting that spongification would be possible. When gold sponges were fabricated only low concentrations of NaOH (0.01-0.2M) were needed and the process of de-alloying took only minutes, whereas for the refractory metals more concentrated (1-2M) NaOH was needed. At times it was also necessary to apply a higher temperature to increase the rate of dissolution for the refractory metal precursors. Even with these changes, de-alloying still took hours to complete. Figure 17 compares the SEM micrographs of diverse achievable nanoporous metals. Molybdenum was also tested and was expected to produce a sponge due to the potential differences well exceeding a few hundred millivolts, however a sponge could not be produced even though the thin film changed colour.

The different structures depicted in Figure 17 indicate the discrete structures that can be produced from some refractory metals. Niobium sponges possess the most peculiar structure compared to the other nanoporous metals illustrated in Figure 17. The morphology appears web-like with ligaments randomly stacked on top of one another rather than the interconnected pores found for nanoporous gold, tungsten and tantalum. The tantalum sponge shows signs of considerable cracking, with large

crevices and even islands of sponge on the substrate. The SEM image of the tantalum sponge demonstrates extreme cracking, implying imminent film delamination from the substrate. The tungsten sponge most closely resembles that of the gold sponges with discrepancies in pore sizes. The surface of the gold sponges seem more uniform to that of the refractory metal sponges, and the pore size is both smaller and more uniform. This difference may be due to cracking and slow diffusion rates in the case of the refractory metals which leads to larger pore sizes.

3.5 Dynamic transmission technique to understand and optimise de-alloying kinetics

A unique and simple procedure was developed to prevent major cracking or complete destruction of films as they separated from the substrate during de-alloying, and provides information about the kinetics during de-alloying. The operating principle is that optical transmission spectra can be fitted to effective medium models to monitor the etching rate and estimate the appropriate stop point. The results presented here contributed to a publication[82] which developed the technique using Au sponges.

Samples were de-alloyed in 10 mm path length quartz cuvettes within a USB2000 Ocean Optics Spectrometer with transmission cuvette accessory attached which repeatedly scanned the transmitted light from wavelengths of 300 to 1000 nm at 0.5 second intervals. The cuvettes were filled with NaOH at room temperature (concentrations 0.2M, 0.15M, 0.1M, 0.05M, 0.03M and 0.01M), which etched away the aluminium in the alloys. Experiments that investigated the effect of temperature on etch rate were performed with a quartz cuvette in contact with a Peltier temperature stage, set to 50°C, 40°C, 19°C, 12°C and at room temperature (~23°C) with 0.1M NaOH. The temperature of the solution was monitored with a K-type thermocouple.

The compositions of the precursor thin films had been measured beforehand using energy dispersive X-ray spectroscopy (EDS). Thin film samples were placed onto conductive carbon tape with additional copper tape used for earthing. EDS was carried out on a Zeiss Evo microscope at 5kV. Multiple areas were analyzed to confirm that films were consistent in composition. Deposited films were confirmed to be $AuAl_2$ (approximately 69.2 ± 1 at.% Al and 30.8 ± 1 at.% Au for the first series of samples and 68.2 ± 1 at.% Al and 31.8 ± 1 at.% Au for the second series). The films displayed a distinctive purple colour indicating that they were substantially comprised of $AuAl_2$ (this compound is also known as 'purple gold' or 'purple glory'.[83]) Optical measurements were conducted on a PerkinElmer Lambda 950 and a J.A. Woollam VASE Ellipsometer. Samples of both the $AuAl_2$ precursor and the nanoporous sponge were measured in both machines to verify instrument accuracy as well as provide enough data for good model fits.

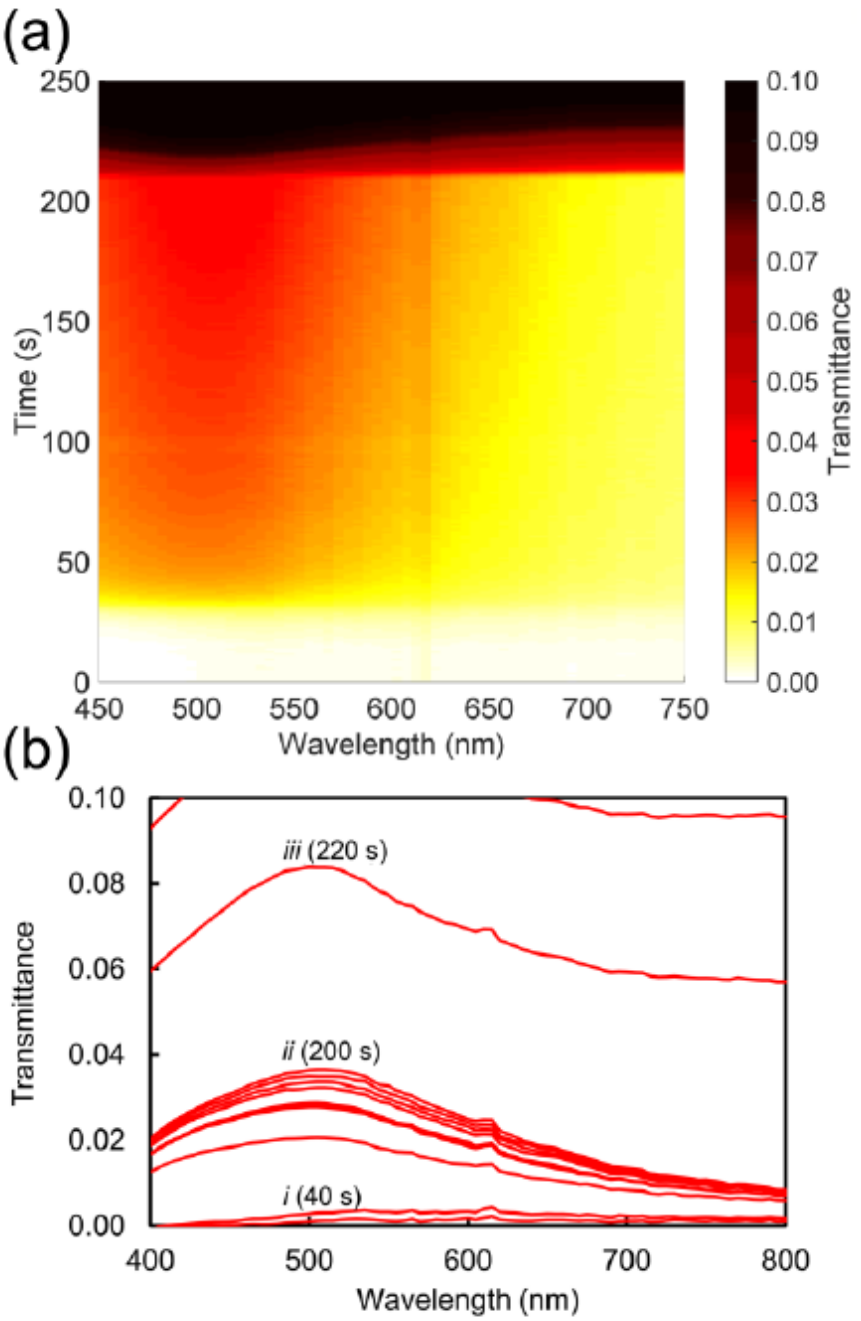

Figure 18 In situ dynamic transmission measurements taken of multiple samples in various NaOH concentrations[82].

An optical model was constructed to extract the thickness of the de-alloyed layer from the transmittance spectra. First, individual oscillator equations for each material were fitted using the WVASE32 software to the ellipsometer data for pure samples of glass, gold, as-deposited $AuAl_2$ and completely de-alloyed Au nanosponge. From the oscillator equations, optical constants $n(\lambda)$ and $k(\lambda)$ were obtained (these are provided, for convenience, in Appendix 1, Appendix 2, Appendix 3 and Appendix 4). The refractive indices of pure H_2O were also used in the model for the aqueous phase as the NaOH concentration was less than 0.2 M. These optical constants were then used to build a

composite thin film stack model using Griesmann's freely available Optical Thin Film Toolbox, (software available from sites.google.com/site/ulfgri /numerical/thin-films). The stack comprised of 4 layers with the first being water, followed by a 1 mm glass substrate, a variable thickness of $AuAl_2$, a variable thickness of nanoporous Au and, finally, another layer of water. The nanoporous Au layer was placed at the top of the stack since, as mentioned, the de-alloying front proceeds inwards from the corroding liquid phase into the solid alloy. The optical model was then iteratively fitted to the measured transmission spectra to estimate the average time-dependent thicknesses of the $AuAl_2$ and nanoporous Au layers of the stack. The mean squared error was generally better than 10^{-6} for most fits prior to the mesoporous gold layer eventually detaching from the glass. Certain constraints were placed onto the thickness fitting to deter the software from producing non-physical results. For example, at t=0 the thickness of the nanoporous Au layer was set at 0 nm, and the starting thicknesses of the $AuAl_2$ layer was set at 160 nm (which was the thickness of the as-deposited film measured by profilometry). The thickness was also not permitted to become negative or the $AuAl_2$ layer to gain thickness after it had de-alloyed. The mesoporous layer was also set to always increase in thickness or stay the same thickness, only until after the $AuAl_2$ layer was zero would it then decrease in thickness to simulate the mesoporous gold layer being removed from the substrate.

The gold sponge produced had the so-called 'foamy' morphology[9]. Foamy sponges are comprised of interpenetrating metal ligaments that define roughly spherical pores, very much like a bathroom sponge. This is distinctly different from the nanoporous sponges produced by de-alloying Au-Ag solid solutions, which consist of a bi-continuous, vermicular morphology of pores and ligaments.

The overall characteristics of the dynamic transmission spectra during dissolution were as follows: initially the transmittances of the films are close to zero due to the thickness of the opaque $AuAl_2$ films, however the dissolution of Al renders the films more transparent as time passes. This is evident in a transmission peak forming at ~500 nm corresponding to the formation of nanoporous gold as presented in Figure 18. Finally, there is an abrupt change at t > 200 s caused by the nanoporous gold film detaching from the substrate.

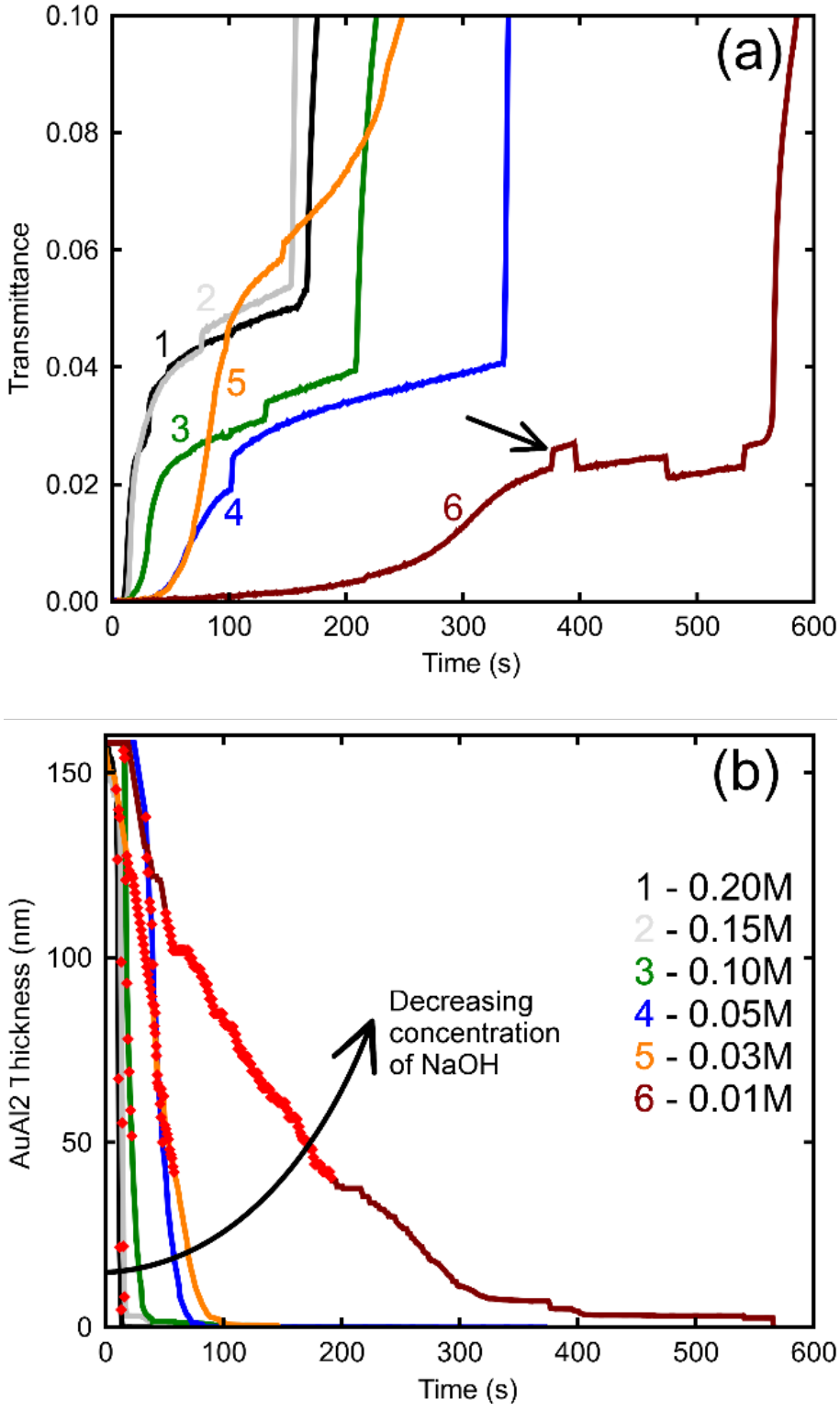

Figure 19 a) Raw *in situ* optical transmittance data obtained for various concentrations of etchant used to de-alloy the $AuAl_2$ thin films, b) the processed data after the raw data is fitted using Thin Film Toolbox[82].

There is an initial incubation period before transmission rises, saturates, and rises again as seen in Figure 19a). This is consistent with breakdown of initial surface passivation, followed by bulk dissolution (formation of porous gold), and then finally the film detaching itself from the glass

substrate. The arrow in the figure indicates bubble formation under the film as it begins to delaminate from the substrate. These abnormalities do not have a great effect on the thicknesses determined by the model as they occur after the sample has already completed de-alloyed. Nevertheless, an attempt was made to minimize the formation of bubbles by placing the sample in the cuvette vertically, allowing bubbles that formed to rise up and escape. The etch rate can be derived from Figure 19b, which illustrates the bulk dissolution rates of the alloy at the prescribed NaOH concentrations. The passivation-breakdown time is evidently concentration-dependent, but the main focus in understanding production of porous gold is the bulk etch rate, which requires further analysis.

The relatively linear areas shown by red dots in Figure 19b were used to determine the maximum rate of de-alloying. Figure 20 illustrates that the maximum etch rates were approximately linear with concentration of NaOH and, therefore, that a first-order chemical reaction is occurring. The small deviations from linearity observed in Figure 20 could be due to fitting inconsistencies and the random nature of de-alloying and morphology of sponges.

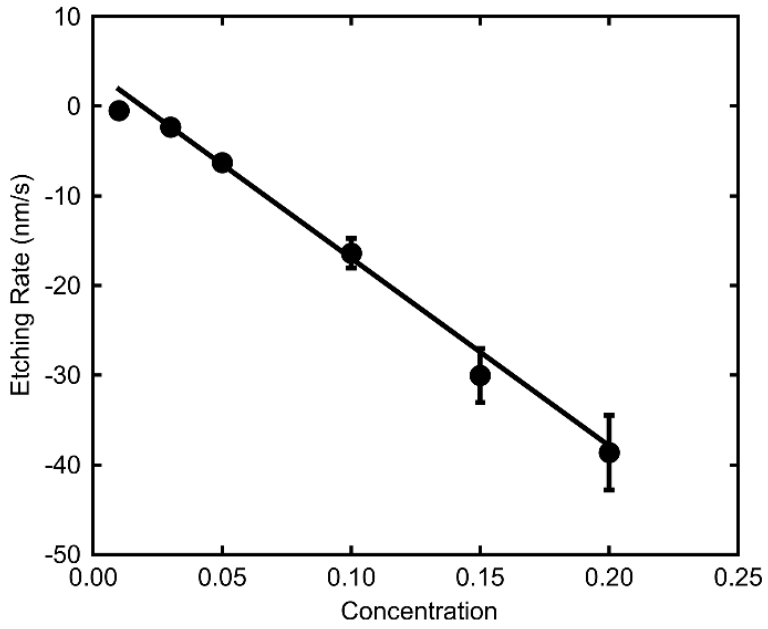

Figure 20 Effect of NaOH concentration on maximum de-alloying rates of AuAl2 (at room temperature)[82].

The effect of temperature (at a concentration of 0.1 M NaOH) is examined in Figure 21a. In this case, an exponential increase in the dissolution rate with increase in temperature is found. An Arrhenius plot was made to obtain the activation energy graphically as depicted in Figure 21b. The activation energy was calculated to be 46.5 ± 6.4 kJ/mol (0.48 ± 0.07 eV). The activation energy for dimer diffusion of gold on aluminium surfaces has been approximated to be 0.82 eV for jumps and 0.24 eV for exchanges[109] and so neither are a good match for the observed E_a. On the other hand, the E_a for

dimer diffusion of aluminium on aluminium surfaces has been reported to be 0.54eV and 0.40eV for jumps and exchanges respectively.[109] The activation energy dissolution of aluminium in sodium hydroxide can also be found in the literature, and is reported to be 0.59eV.[110] Therefore, a better match of activation energy is found here for processes involving Al rather than those involving Au, suggesting the rate limiting factors here involve movement and dissolution of Al.

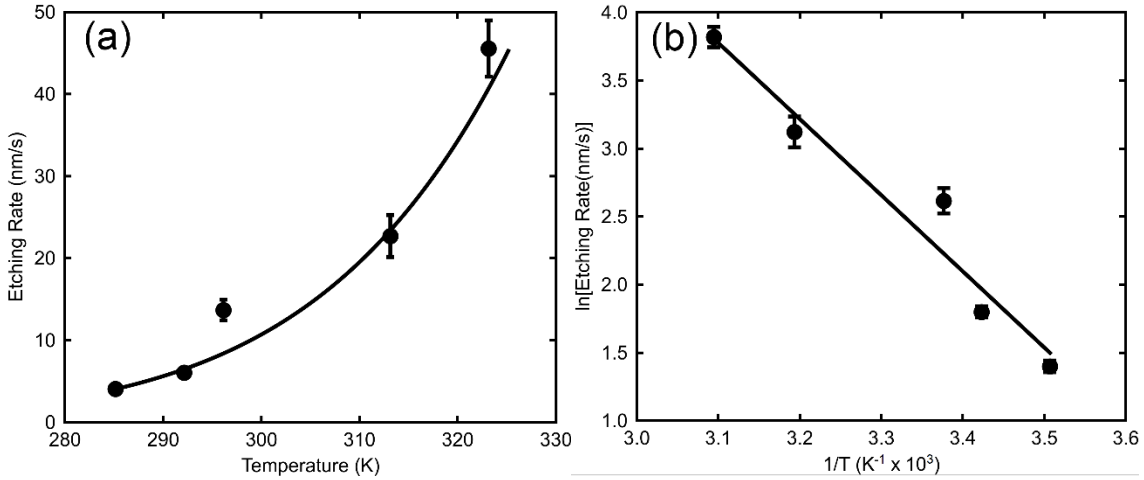

Figure 21 a) The maximum etch rates at different temperatures of NaOH to de-alloy $AuAl_2$ thin films, b) processed etch rates of varying temperatures to determine the activation energy of the system[82].

3.6 Optical properties of the nanoporous metals

Nanoporous metals may possess optical properties very different to that of the precursor alloy. There have been examples of these sponges exhibiting very dark films due to absorption of light from the pores or in the case described in this section, they retain most of gold's optical characteristics. Refractory metal sponge's optical properties have not been observed in depth as much as gold sponges have been. For this section of the chapter, the optical properties for both the gold and refractory sponges produced will be discussed.

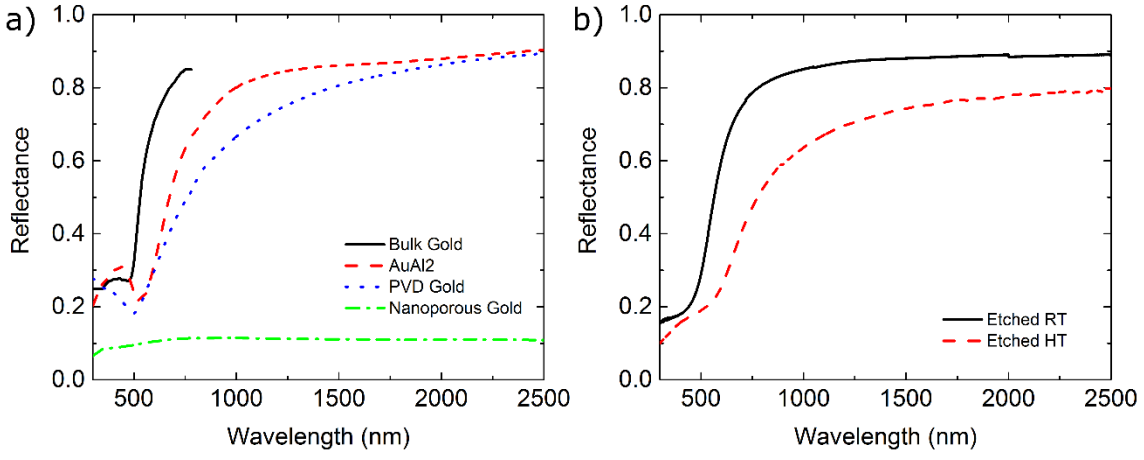

Figure 22 Comparison in reflectivity of a) different types of gold[7], b) nanoporous gold sponges from either RT or HT deposited precursor alloys.

The reflection data shown in Figure 22 addresses the differences in the two types of sponges produced. The sponges produced earlier by Cortie et al. display a flat spectral response throughout all wavelength ranges illustrated in Figure 22[7]. The reflection measurements of PVD gold and $AuAl_2$ are very similar with $AuAl_2$ being more reflective in the visible to NIR range. Similarly the etched RT deposited thin film has similar flatness across the visible to NIR range at just below 90% reflection. The fabricated gold sponges appear gold rather than the dark colour which are the more commonly observed type of sponges. This is due to different structural network of the gold sponges constructed in this investigation, resembling pinhole sponges rather than fibrous ones.

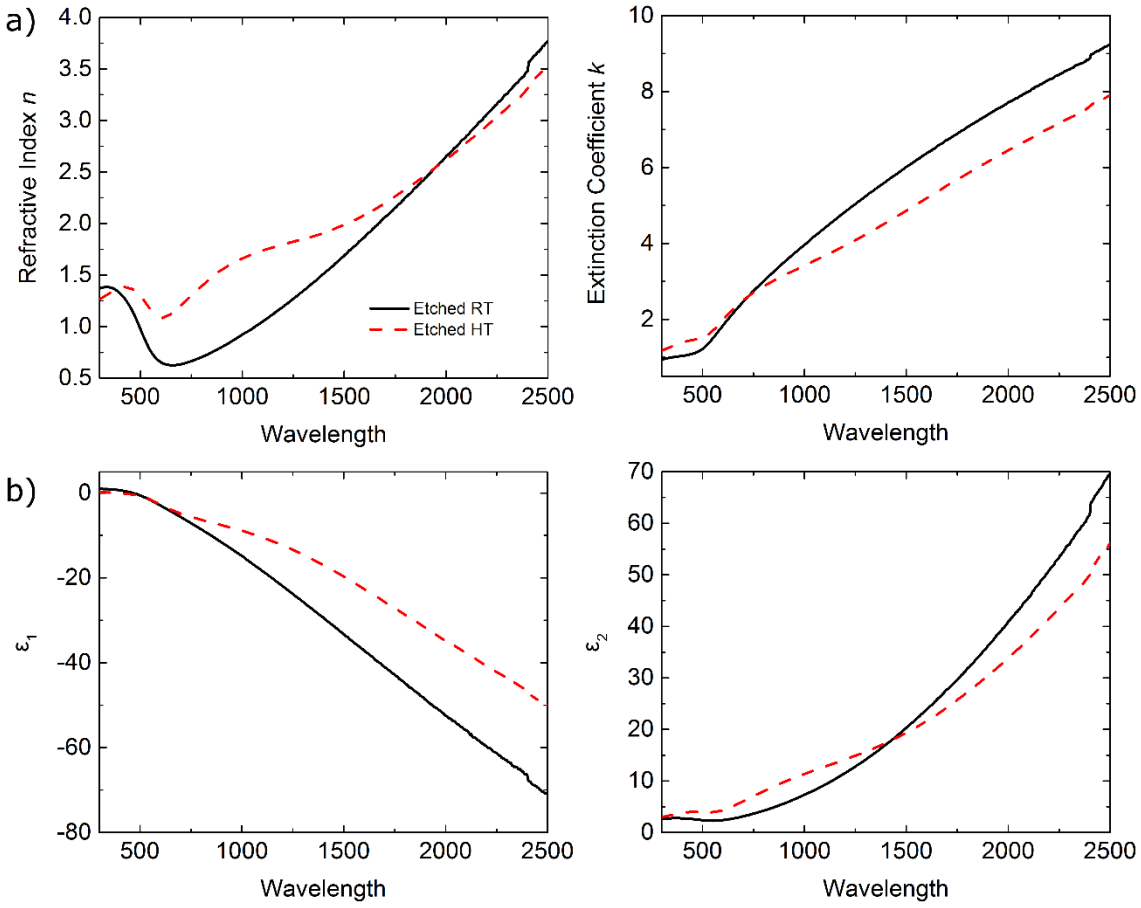

Figure 23 Comparison of the a) optical constants (n and k) b) dielectric constants of etched RT and HT deposited $AuAl_2$ thin films

Once again, the HT deposited sample is darker than the RT deposited sample even when etched due to the surface of the sponges retaining some roughness and crystals of $AuAl_2$. The decrease in the low visible wavelengths is much sharper for the etched RT sponge than the HT as the film colour remains a dark gold colour, though this discrepancy is most likely due to scattering from the

roughness of the films. Further information is provided by evaluating the optical constants and dielectric constants displayed in Figure 23.

Negative ε_1 values as well as an increasing ε_2 suggest the sponges possess metallic properties. There are slight differences between the two etched alloys. Both sponges had similar ε_1 values in the visible range with a greater decrease for the RT sponges which implies a better conductor due to more a uniform sponge morphology. ε_2 were also similar in each sponge with the RT sponge lower than the HT sponge in the visible range with a swap in position at approximately 1425 nm. An examination between the ratios of the dielectric constants for both sponges verify the lossy nature of these conductive materials. The largest differences appeared in the refractive index *n* within the visible region. The room temperature sponges possessed a broader dip starting at approximately 550 nm which coincides with a reflectance drop at that wavelength. This dip in *n* also appears in the HT sponge though the drop in the reflectance is much smaller. However, once again both sponges are similar in the NIR region. Further evidence of the metallic nature is the high *k* values consistent with negative permittivity, a defining feature of metals. The large *n* and *k* values also denote a highly reflective metal.

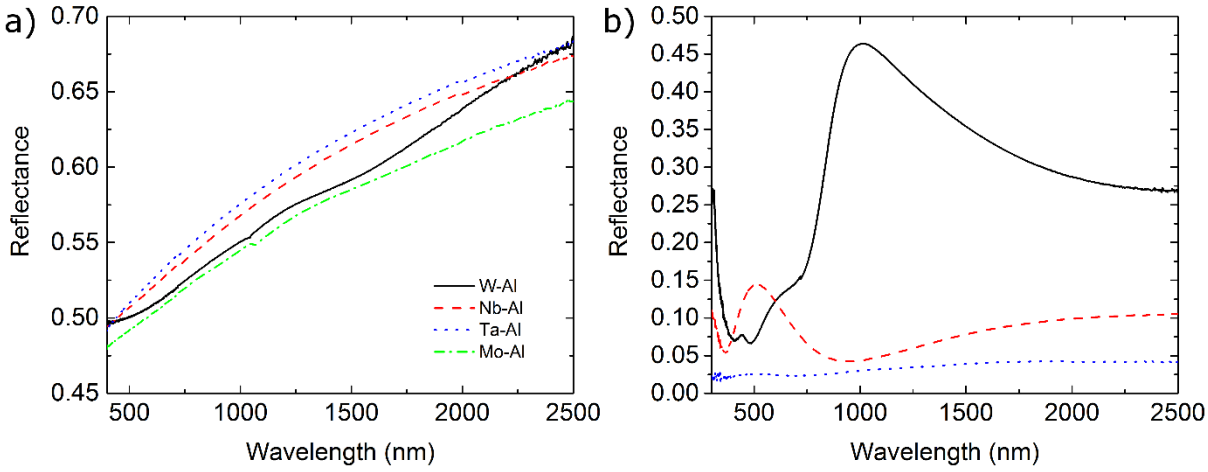

Figure 24 a) Reflection data of precursor refractory metal alloys and b) the resultant sponge after de-alloying.

The most significant difference from precursor alloy to the sponge was seen in the HT sample. The change was from a poor conductor low refractive index thin film to a conducting metallic sponge. This occurs for both RT and HT $AuAl_2$, though a more significant change was apparent for the HT sample. Conversely the changes in the RT precursor alloy to sponge appear to blue shift the position of the peak in the refractive index at approximately 500 nm and causes a steeper incline of *n* after the dip at 550 nm. Overall, for both the precursor alloys the conductivity increases after de-alloying due to the removal of the less conductive element.

Optical properties of refractory metal sponges are revealed in Figure 24. The refractory metal precursor alloys formed with aluminium did not have significant differences between the reflection characteristics apart from greater magnitude for some samples, with the shapes of the spectra all relatively linear. The more interesting optical properties occurred after de-alloying with various structures produced as shown earlier in this chapter. These spectra resemble oxides formed from these refractory metals, though spongification had occurred. Images of the films in Figure 25 depict the oxides formed after de-alloying, with the precursor alloys initially possessing a grey-silver colour. This oxidation process occurs after the selective dissolution of aluminium as well as some of the metal and oxide. The refractory metals are also etched due to the concentrations of NaOH selected[111-113]. It has been demonstrated that low concentrations of sodium hydroxide can passivate the natural oxide layer formed on these metals, though with sufficient strength further oxidation can occur as well as etching of the metal. This also explains the colour changes between the niobium samples presented in Figure 25a and d. Longer exposure to sodium hydroxide would further increase the thickness of the oxide in addition to dissolve the metal resulting in a greater interference pattern and more translucent film.

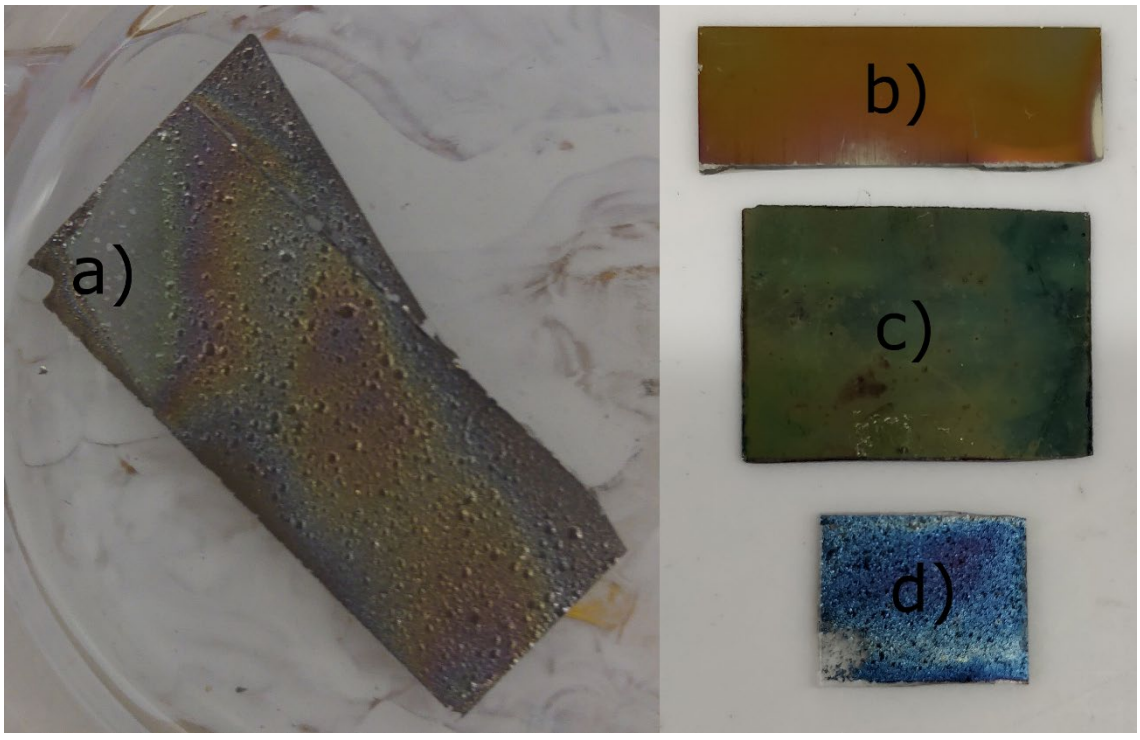

Figure 25 Refractory metal sponges of a) niobium during de-alloying on glass, b) tungsten sponge on glass, c) tungsten sponge on a thermal oxide silicon substrate, d) niobium sponge on glass after the first colour change.

3.7 Thermal stability of gold nanoporous sponges

The same apparatus was used to observe the optical changes in $AuAl_2$ samples by in situ heated ellipsometry (Chapter 2) were used for the sponges. The results have been published[1]. An etched HT deposited thin film sample is depicted below: it reveals that the rough surface and large crystals remain even after selective dissolution. The crystals persist due to incomplete dissolution, but interconnected pores and ligaments are formed around them. The etched HT deposited samples were annealed to ~325°C in increments of 10°C with a full spectroscopic scan at angles 60-75° in 5° intervals which will be referred to as the "step" results. As temperatures increased, continuous measurements at 1000 nm were taken at 70° which will be called the "ramp" results. Each image in Figure 26 was viewed by the SEM at various temperatures based on the optical shifts in the sponges at certain temperatures. These shifts in the optical properties were also observed through the ramp data obtained during the experiments in Figure 27. The temperatures were selected to find transition temperatures. There are two main transitions that occur during the annealing process. These changes occur due to the coarsening and breakdown of the sponge with the pores aggregating together and cluster around the crystals such as in Figure 26c, d and to some extent, b.

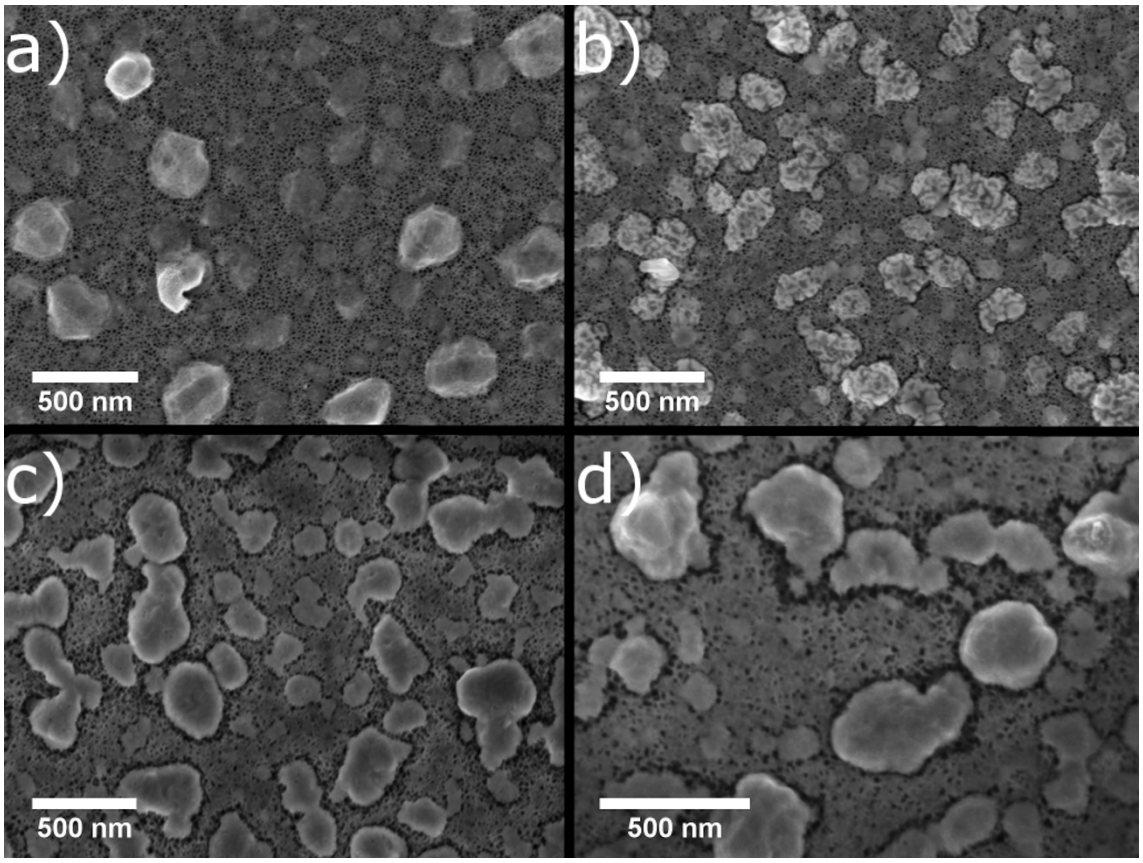

Figure 26 a) High temperature deposited $AuAl_2$ after etching in 0.1M NaOH, b) post annealed etched sample at 50°C, c) post annealed etched sample at 100°C, d) post annealed etched sample at 325°C [modified image from publication[1]].

Closer observations of the *in situ* heated ellipsometry ramp data in Figure 27 indicate two temperatures of critical change in psi. The first and slowest change, occurred at approximately 50°C with a linear decrease before plateauing at around 160°C. This transformation corresponds to the structural differences between Figure 26a, b and c, where the sponge begins to coarsen. The coarsening entailed the amalgamation of pores and crystals. The second transition occurs at approximately 250°C and was more sudden, almost an immediate change once the temperature was achieved. Further temperatures were not explored as 325°C was the maximum temperature possible with this system. The SEM image shown in Figure 26d reveals a sponge with fewer pores with them aggregated along the edges of the crystals. It also shows larger crystal structures. This may be explained as the result of higher temperatures leading to increased diffusion which resulted in movement of gold atoms. When the crystals are compared between Figure 26a and d, the crystalline, faceted appearance is lost at the elevated temperatures, culminating in more rounded crystals. Overall the transitions in the optical data relates to structural changes of the crystals and coalescence of the pores. The slow transition from room temperature to approximately 150°C was investigated further to clarify the temperature required for this transition in the optical data.

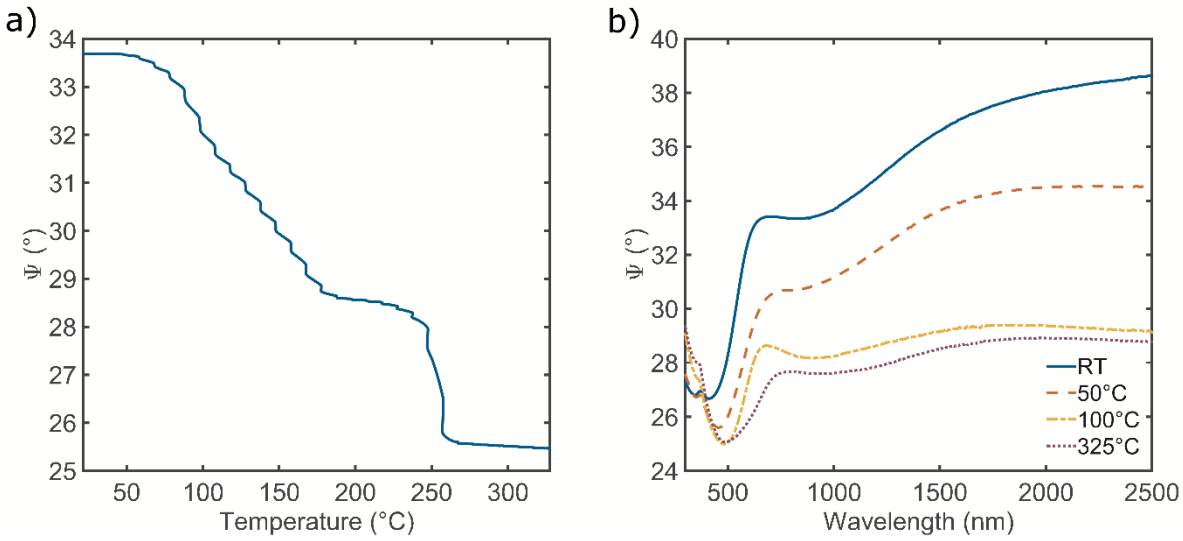

Figure 27 a) Psi values of the etched HT deposited samples during *in situ* heated ellipsometry, b) full spectroscopic ellipsometry of the post anneal etched HT samples at specific temperatures.

Figure 27b) also shows the change in the HT sponges across all measurable wavelengths in the ellipsometer. These were post annealed measurements and verify the permanent change that has happened. The relative shapes of the plots are similar with the most significant change being the position of the dip, initially at ~450 nm shifting to ~500 nm. It should be noted that the 50°C sample was placed in the oven for over 65 hours to observe whether the slow optical transition at the beginning of Figure 27a was achievable at lower temperatures. It is evident that the psi values for

the 50°C sample had reduced much more than the ramped in situ heated ellipsometry. This indicates that the coarsening of gold sponges ensues even at low temperatures, suggesting with longer exposure at low temperatures can still cause this shift. For the 325°C sample the sponge seemed to revert back to the first transition for psi as the post anneal graph (Figure 27b) psi values match the values prior to the last transition.

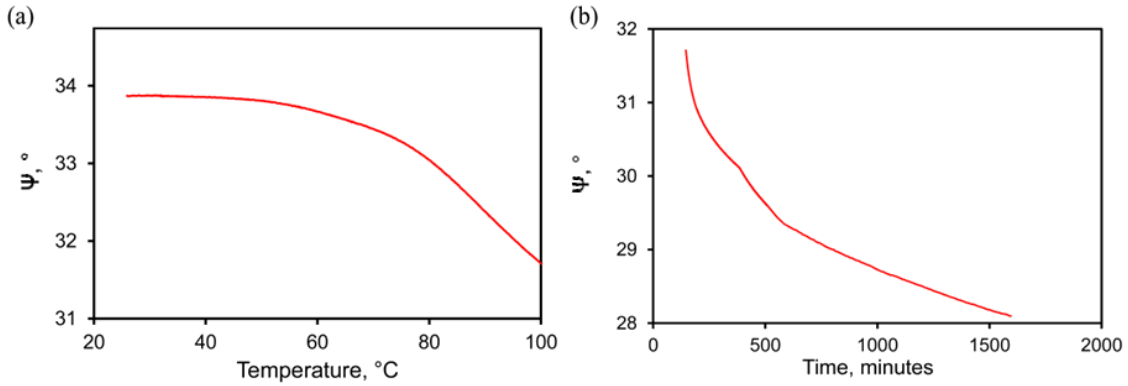

Figure 28 a) thermal stability measured by the change in psi whilst annealing to 100°C, b) change in psi held at 100°C[1].

Another investigation was conducted within the *in situ* heated ellipsometry apparatus to observe changes in psi resulting from structural changes (sponge coarsening). The sample was annealed up to 100°C and held at that temperature for approximately 24 hours. Figure 28a depicts the ramp of the temperature from room to 100°C and b illustrates the variation of psi as it is held at maximum temperature. Though the transition is very slow, psi continues to decrease readily after 50°C is passed. This process begins to speed up after 80°C and finally, rapidly increases once the temperature has reached 100°C. The transition decreases exponentially as time passes and after 400 minutes the continual decrease in psi slows down significantly. Further change would probably have continued if the sample was left in the chamber for a longer time as psi continues to slowly decrease.

This method was also employed for a RT sponge and the optical constants *n* and *k* are compared in Figure 29. The optical data reveals a stark difference between the two sponges where *n* increases for the HT sponge, it decreases with the RT sponge as the temperature was raised. Furthermore, there were negligible variations in *k* for the RT sponge with it remaining high, but for the HT sponge, *k* decreases. The *k* values for both samples were initially very similar and only the HT sponge varies at all. Examination of the dielectric constants of these sponges demonstrated the nature of these films as they were annealed. For the HT sponges, the refractive index increased and the extinction coefficient decreased. A positive ε_1 which is given by the increases to the value in Figure 29a. Conversely for the RT sponges, ε_1 becomes slightly more negative (Figure 29b) with slow decrease in

the ε_2. Most of these alterations resemble shifts of the peaks in the optical constants to longer wavelengths.

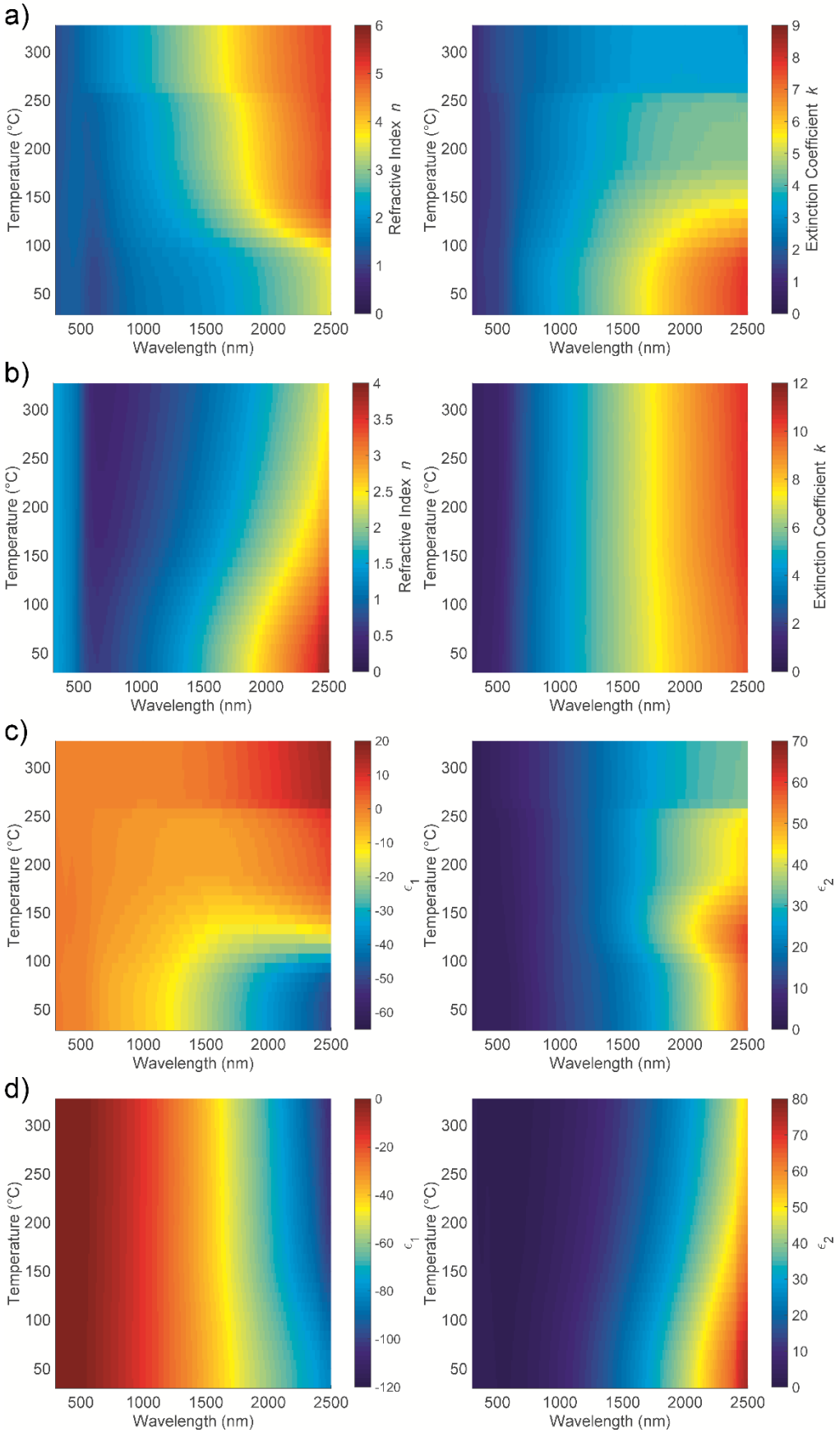

Figure 29 Refractive index *n* and extinction coefficients of a) HT and b) RT deposited $AuAl_2$ sponge, dielectric constants of c) HT and d) RT deposited $AuAl_2$ sponge during in situ heated ellipsometry.

3.8 Summary

Gold sponges possess unique optical properties with the thin films discussed in this chapter having properties quite different to those of bulk Au, due evidently to their high surface area and 'pinhole' structure. These nanostructures were made possible with chemical etching of precursor alloys with NaOH. Refractory metal sponges were also producible with this same method of de-alloying. In this case some types of film (tungsten and tantalum) showed a similar morphology to gold but in other case (niobium) there was a unique network morphology. The etching protocols for these sponges were more aggressive with the use of more concentrated alkaline solution and extended soak times. Within this dissolution process, the refractory metals formed oxides as a side effect of the concentration of NaOH selected. The nanoporous refractory metals were visually similar to that of their oxide counterparts.

An optical model based on *in situ* transmittance measurements made during the de-alloying process could be successfully used to monitor the de-alloying kinetics of $AuAl_2$ in NaOH solutions. The available evidence indicates that the rate is limited by movement of Al atoms and not by surface diffusion or movement of the Au atoms.

Experiments investigating the thermal stability of HT deposited gold sponges revealed low temperature thresholds for permanent coarsening of the sponges. Temperatures as low as 50°C were able to begin the process, though prolonged periods of time were necessary to reproduce the same transitions that occur at higher temperatures. However, for RT deposited sponges the opposite effect (decrease in n and k rather than an increase as was seen for the HT samples) was observed, with optical constants compared between the prepared samples. For both sponges, annealing the samples to 300°C resulted in optical changes to the sponge, with stark transitions for the HT sponges at 150°C and 250°C and lesser changes at 150°C-200°C for the RT sponges. These results indicate that relatively low temperatures can significantly alter the optical effects of these sponges. Thermal stability of nanostructured refractory metals will be discussed in later chapters.

CHAPTER 4 – FORMATION AND MORPHOLOGIES OF REFRACTORY METAL 'NANO-FINS'

Published work featured in this chapter: Tai, M.C., Gentle, A.R., Arnold, M.D., Cortie, M.B., 2018. Nanotechnology 29, 105702.

4 Chapter 4 – Formation and morphologies of refractory metal 'nano-fins'

In the process of preparing refractory metal sponges (Chapter 3[114]) a slight modification of the experimental process yielded a very interesting new nanostructure. These 'nano-fins' were deposited by DC magnetron sputtering with no rotation and are relatively ordered. In this chapter the factors that can cause nanostructure formation during sputtering, some conditions necessary for the formation of the new nanostructures, and preliminary evidence of their optical polarization will be discussed.

As noted previously, nanostructured refractory metal coatings are of great interest due to their potential for optical[115-117], mechanical[14,22] and electrical[3,16] applications. In particular, there is a strong motivation for preparing polarizing coatings from refractory materials[118,119]. This is because the complexity of current optical systems and exposure to harsher environments and higher temperatures may cause the degradation of commercial polymer polarizers.

Although polarizing metal coatings can be prepared by deposition onto a suitable template[120], it may be more attractive to fabricate nanostructured porous films using glancing angle deposition (GLAD)[121,122]. With this method, many different structures can be formed with columns tilted or perpendicular to the substrate[123-125] and there is no need to apply a template first. An even broader range of structures can be created by additionally varying substrate angle[126] and/or rotating the stage[127,128]. An important example is serial bi-deposition (SBD), an extension to the GLAD technique whereby the azimuth angle is rotated at specific angles to construct more defined columns with greater anisotropy[129]. These sculptured thin films possess high polarization due to increased structural anisotropy as the columnar structures align in the plane of the film[130]. Previous studies have outlined the applications of such films due to the range of different materials featuring these unique optical and structural properties [127,129,131-139]. Over the years more methods have been researched and optimization of the attributes achieved. Various methods have been employed to produce multiple types of nanostructures ranging from tilted columns to square spiral or helical columns[139-143]. Today, even with the increasing ability to directly engineer many different nanostructures, obliquely angled deposition remains a useful method in the construction of these films. This process is still performed due to the ease, efficiency, precise nanoscale control and the ability to produce these films on a large scale[142-144].

Electron beam evaporation applies a high power electron beam to melt a desired material in high vacuum. This results in a highly directional, low energy, vapour stream impinging on the substrate.

Nanocolumns form due to a phenomena known as self-shadowing or ballistic shadowing. Surface diffusion, which in thermal evaporation can be enhanced by heating the substrate, also plays a role in the aggregation of nanocolumns. Surface diffusion must be limited to allow the formation of columns. Self-shadowing increases the likelihood of columns whereas surface diffusion fills in the voids produced[145]. Evaporated source material arrives onto the surface and deposits randomly on the substrate. As the atoms aggregate the shadowing effect becomes the major driving force for columnar growth. The columns will begin to grow as the material will be deposited onto it and less onto shadowed area. Thus voids are created throughout the thin film. Eventually only the tips of the columns will receive flux and large defined columns can be generated[143]. In general, these nanostructured thin films are most easily produced by electron beam evaporation; however refractory metals are difficult to evaporate due to their high boiling points. Instead, sputtering can be used to form columnar films provided that angular spread is restricted[146,147]. Angular spread of the deposited material is generally controlled by the substrate. The movement/rotation, height/distance from target source or tilt of the stage may be altered to tune the angular spread. One or more materials have been deposited simultaneously to form columnar thin films in this way, with the column tilt favouring incoming flux of the material placed at an oblique angle to the substrate. El Beainou et al. revealed that co-sputtering of W-Cu at oblique angles results in the metal closest to the substrate dominating the other but with the slanted columns still apparent when the input power is shifted, though with high Cu power these columns are less distinct[148]. With or without rotation, these columnar structures can be produced, either tilted or perpendicular to the substrate. Yahya et al. developed columnar structures of Ti-Ta with a combinatorial GLAD technique on static and rotated substrates[149]. That investigation found that, on the static substrate, the column tilt was more significant and more fanned out structures were formed along the thickness gradient. In general, both self-shadowing and crystal-formation[150] can contribute to the shape of the columns, and there are tantalising observations of structures that seem to require both processes. In particular self-assembled triangles, somewhat reminiscent of those produced by chemical synthesis, appear haphazardly in oblique deposits[151].

Oblique angle deposition, as utilised in this chapter, is distinguished from GLAD by deposition angle closer to the normal: the growth resulting from sputtering single metals at these angles is often tightly-packed[152]. However, it has been observed that sputtering elements with disimilar atomic radii can produce tilted columns that grow towards the element with the smaller radius[153,154].

Further investigations have suggested that the incorporation of directional flux and large size difference between the atoms in a bimetallic structure cause lattice strain in the material, thus

producing tilted columns[155,156]. Lamas et al. were able to produce a stress model for YSZ (oxide) films to predict the tilt angle of the columns formed. While we believe that this mechanism could contribute to the results shown here, the different conditions used here lead to growth that is sparser, is more ordered, and has more complex texturing, suggesting that other mechanisms are important.

In the remainder of this chapter we outline efforts to obtain a basic understanding of the conditions required for formation of the newly observed nano-fins.

4.1 Fabrication of nano-fins

As in other chapters of this thesis, metals were co-deposited on glass and silicon substrates. The glass slides were sonicated in detergent water for 20 minutes and rinsed with deionized water finally being dried with nitrogen gas. The silicon substrates were cut from wafers and sonicated in acetone for 10 minutes then ethanol for 10 minutes and rinsed in deionized water. Finally, they were dried with nitrogen gas.

We investigated many combinations of elements, but most central to this chapter were refractory metals combined with Al. Molybdenum (99.98%)/ vanadium (99.999%)/ tantalum (99.95%)/ tungsten (99.95%)/ chromium (99.9%)/ niobium (99.9%)/ ruthenium(99.9%) and aluminium (99.95%) targets with diameters of 50 mm were DC magnetron co-sputtered in a high vacuum chamber at base pressures better than 2.0×10^{-5} Torr (2.7×10^{-3} Pa). The substrate stage was placed in between and approximately 130 mm vertically from the two targets. The targets are spaced 150 mm apart from one another at a 37° angle to the stage normal at the centre of the target, leading to an angular spread (30°–46°) due to the physical dimensions of the target. It is important to note that deposition at these angles would usually be expected to form dense grains rather than the distinct fins observed here. The deposition was sputtered in argon with a pressure of 2.7 mTorr (0.36 Pa) controlled by a valve and baffle on the turbo pump.

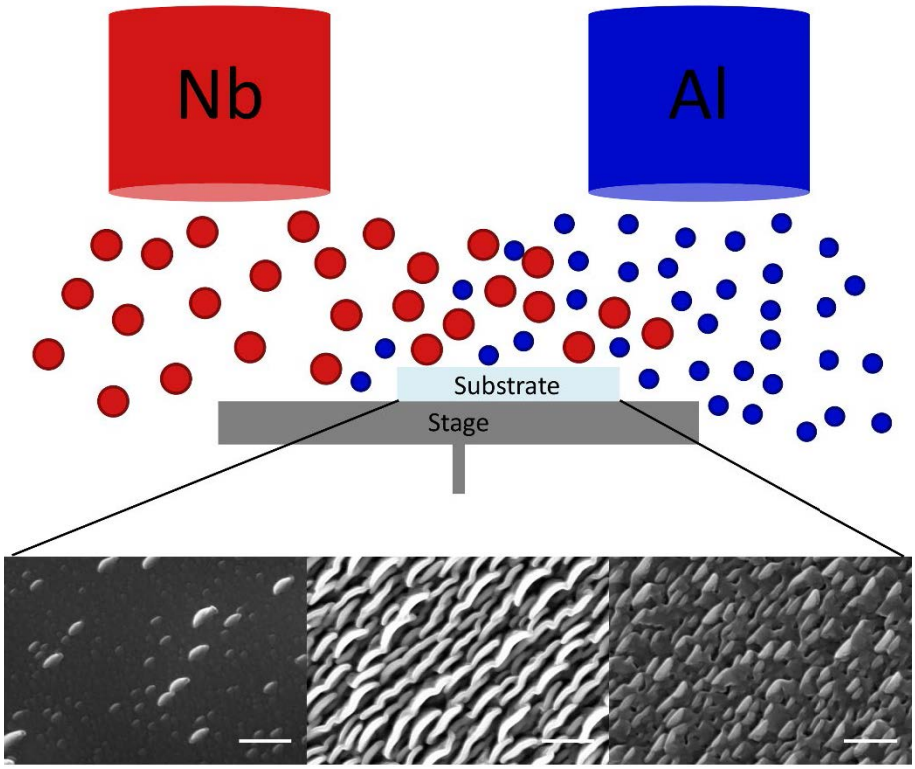

Figure 30 Set up of the DC magnetron co-sputtering used to construct the nanostructured thin films[114]. All scale bars are 200 nm.

For example, Mo–Al nano-fins were sputtered at currents and accelerating voltages of ~320 V (0.25 A) an ~370 V (0.3 A) for the molybdenum and aluminium targets respectively. The samples were deposited for a minimum of 20 minutes in ambient temperatures to ensure formation of the nano-fin structure. During deposition the stage was stationary and aligned to be parallel to the targets just as depicted in Figure 30. It was noted that having a stationary stage was vital in the creation of the nano-fins as rotation of the stage yields uniform, more reflective thin films.

4.2 Analysis of nano-fins

The nano-fins deposited on the silicon substrates were used for imaging with the Zeiss Supra 55VP SEM in plan and cross-section view. The sputtered samples on silicon were scored with a diamond pen on the backside to avoid damage to the surface of the films. EDX was performed to estimate the elemental composition for these nanostructures in a Zeiss Evo SEM. Reflection optical measurements were conducted in an Agilent Cary 7000 UV/VIS/NIR UMS for s- and p-polarisations (relative to the growth plane of the nano-fins) at angles of 6°, 15°, 30°, 45° and 60° for the samples that were deposited in different gas pressures. The nano-fins were aligned vertically and incidence angles were swept horizontally across the structures. Extinction ratios were obtained by dividing the polarised reflectance data obtained in the same system at 10-85° at 5° intervals. However, only up to

70° is shown in this chapter as the spot size increases significantly at high angles which produces errors in the reflectance measurement.

4.3 Conditions for construction of nano-fins

4.3.1 Alterations of sputter energies during film deposition

As mentioned before, a stationary stage was required for the formation of the refractory metal nano-fins. Other deposition conditions were investigated to determine the parameters controlling the formation of these nanostructures. The spread of the co-sputter area was observed by placing a glass slide lengthwise on the stationary stage. The zone of formation is illustrated in Figure 31 where the powers were changed for the vanadium target from 0.2 A, ~370 V to 0.25 A, ~375 V. Furthermore, arrays of nano-fins only formed in distinct areas of the substrate, corresponding to satisfaction of the required conditions of angle and flux. Adjustments of current and voltage altered the range of the nano-fin formation and the size of the area. The zone of formation was always closest to the aluminum target and stretched from that side and slowly attenuated in the direction of the refractory metal target. Increasing the refractory metal current caused the nanostructures to be deposited towards the aluminum target and vice versa.

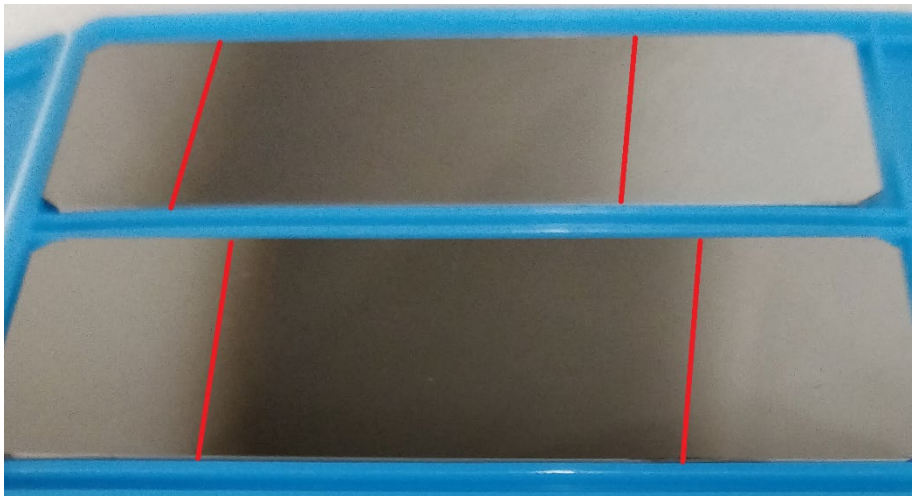

Figure 31 Shift in the area of nano-fin growth depending on sputtering energies for V/Al at V:0.2 A, Al:0.3 A (top) and V:0.25 A, Al:0.3 A (bottom).

During deposition, the fabricated structures were curved (concave side) towards the refractory metal flux. Surprisingly, in this investigation the nano-fins grew toward the larger sized radii metal. This was possibly caused by the fact that the substrate was positioned closer to the aluminium target so that the refractory metal flux was at a sharper angle. Figure 32 illustrates the shapes in

plan view and the resemblance of these nanostructures to fins. However, the zone often shifted with different materials and so this tilt towards the refractory metal is not completely understood.

4.3.2 Position of substrate

Adjustments of accelerating voltages and currents of the two metal targets indicated similar results to that of the spread of growth as seen in Figure 32. The first two images in Figure 32a present a lack of growth and a scarce amount of produced fins. With increased Al, structures similar to that of typical nano-fins were created. However, these nanostructures appear to have identical base structures yet lack the thickness of the typical fins with gaps or voids. Figure 32b reveals tilted views of the nano-fins which confirms the scarcity of the fins with high Nb composition further proving the lack of thickness/height of the fins.

Higher concentration of Al illustrated in Figure 32b produced less more rod-like columns. There was also less distinct separation between the structures as there were many more voids with the fins. Multiple different sized fins developed and do not coalesce to form full sized fins. The tilted front/back view in Figure 32c displays the different shapes of the fins. While the typical nano-fins were rectangular, the higher Nb composition appeared more trapezium-like and finally in the high Al composition area were more rounded edges. On either side of the zone of formation we observed underdeveloped nano-fins (either scarcity of fins or lack of thickness combined with voids). This underlines the importance of placement of the substrate in order to maximise area of fin occurrence.

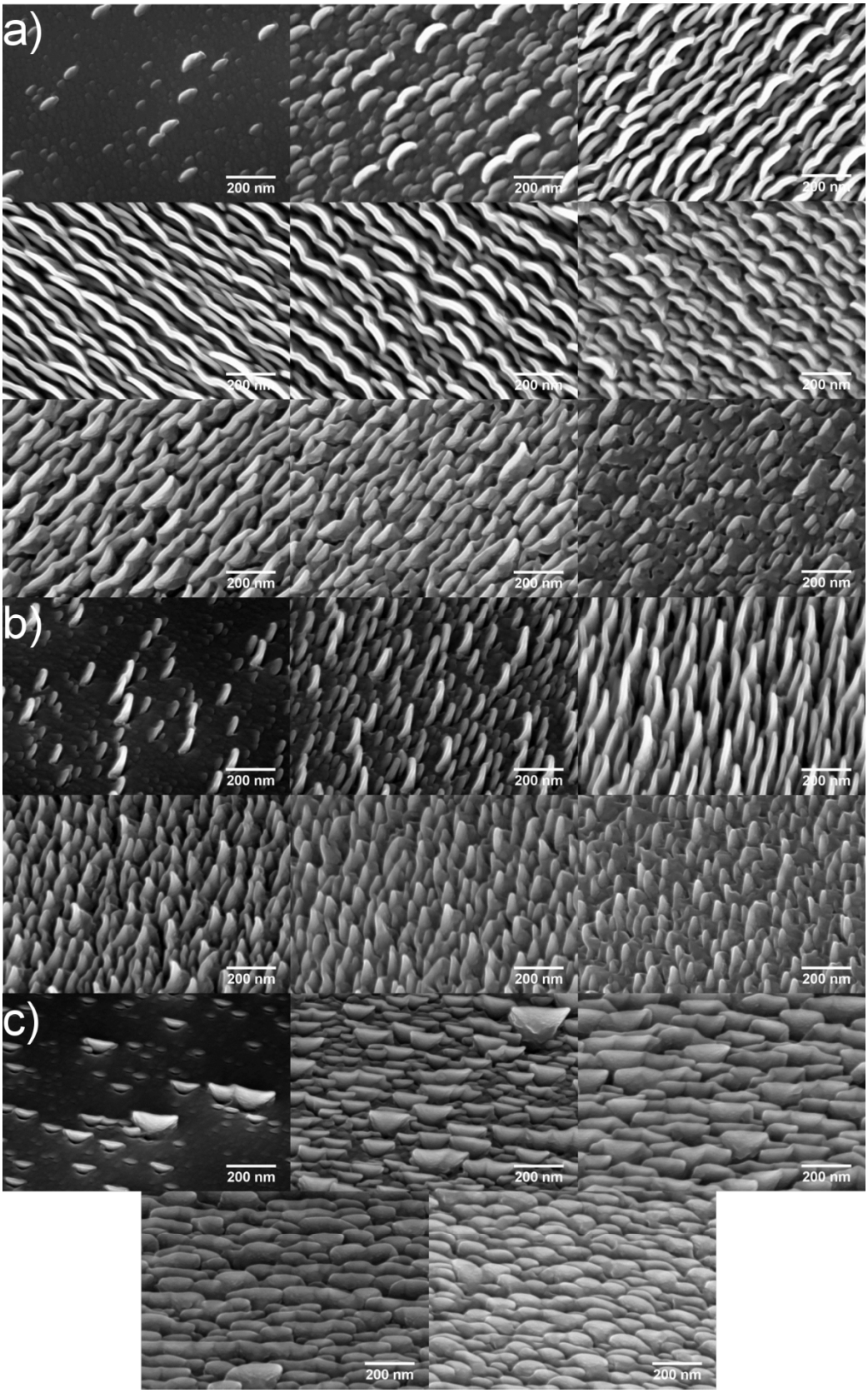

Figure 32 Spread of nanostructures and formation of the nano-fins at a) plan view, b) tilted side view and c) tilted front/back view. Samples were produced with Nb/Al with increasing Al composition from left to right.

4.3.3 Gas pressures within sputter chamber

Similarly, alterations of the gas pressure of the system during deposition also affected the growth of nano-fins and are portrayed in Figure 33. The SEM images reflect the scarcity of the nano-fins with reduced gas pressures as mainly the silicon substrate was observed in Figure 33a. This result was observed in the reflection data where there was a lack of differentiation between polarisations. Even pressures with close to a standard growth contained areas of no growth as seen in Figure 33b. This emphasises that conditions must be finely tuned to obtain abundant fin development. Slight increases in the gas pressure (Figure 33c, d and e) did not appear to affect the formation of the fins, with the only noticeable differences of greater tilting and larger fins. The normal recipe used to produce these films resulted in a coating that could act as a polarizing filter for light due to enhanced ordering and coverage of the fins. The reflectance also reduces significantly from the 2 mTorr film to the 2.7 mTorr film due to the formation of the nanostructures. The tilt of these films as discerned in Figure 34, indicates the anisotropic nature of these films. Optically the 3 and 3.5 mTorr samples were very similar and possess almost identical morphologies as well. The most substantial difference occurred once the argon pressure was approximately double the original nano-fin recipe illustrated in Figure 33f. Then, the nano-fins are reduced in size and the curve on one side of structures are less prominent. The packing density also decreases with areas between the voids being filled with more fins or larger fins coalesced.

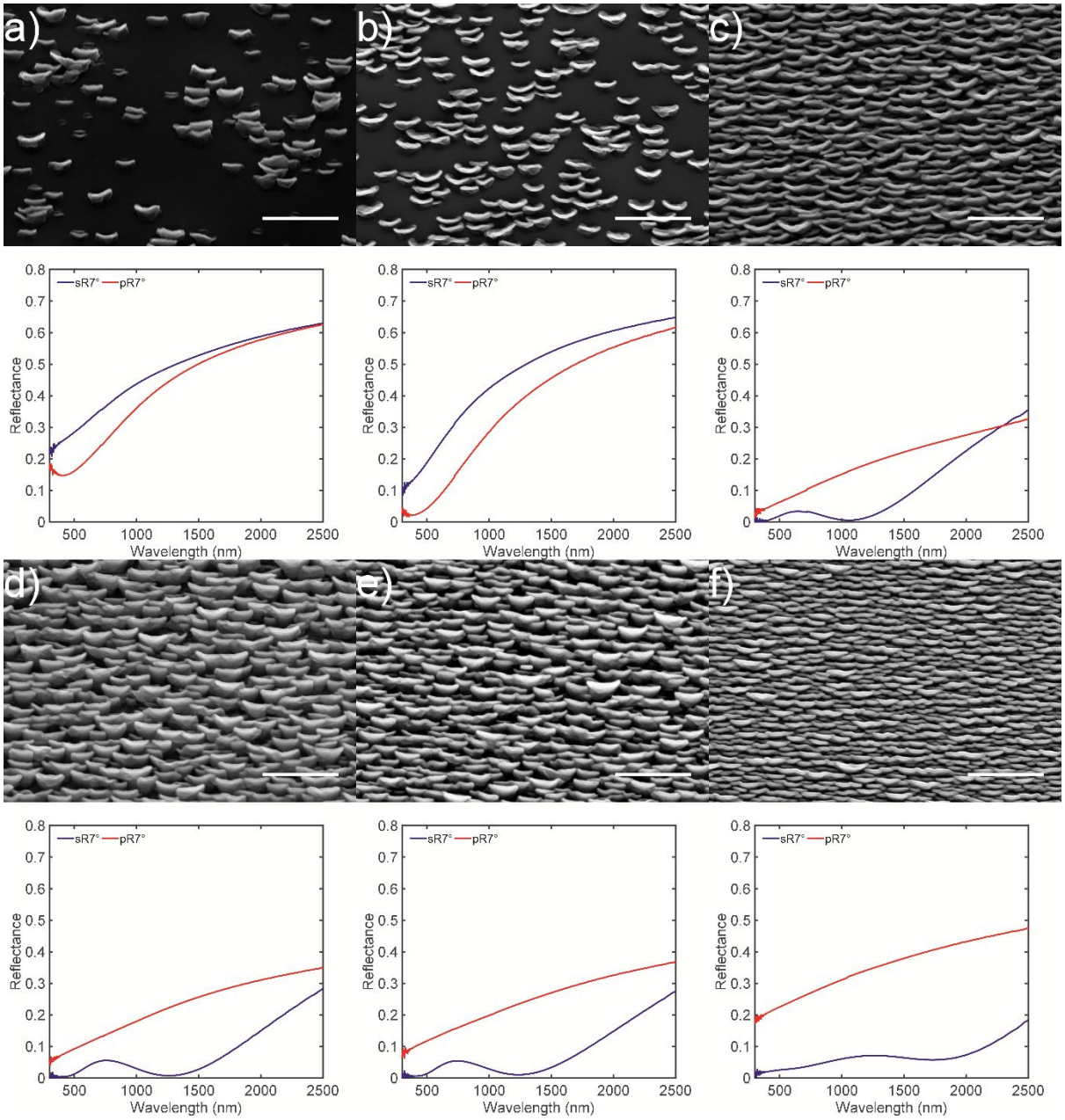

Figure 33 SEM images of 20 minute deposited nano-fin Mo-Al with their respective s- and p- polarised reflectance at angle 6° for nano-fins produced at gas pressures of a) 1. 5 mTorr, b) 2 mTorr, c) 2.7 mTorr, d) 3 mTorr, e) 3.5 mTorr, f) 5.5 mTorr. All scale bars are 500 nm.

The nano-fins are packed more closely together for the 5.5 mTorr sample, which suggests increased ordering of the film. This could be caused by high thermalization of the sputtered atoms due to a reduced mean free path which produces straighter columns and denser films[157]. Improved ordering and density shifts in the fins also improved the polarisation ratio for reflection with an increase in the p-polarised reflectance. The s-polarised reflectance also smoothens and becomes a flatter response than previously encountered for other pressures. All the films grown in varying gas pressures have the underlayer as previously discussed and were approximately within 350-450 nm in

total thickness. Once again, through slight variations in gas pressures, the thicknesses as well as the density/order of these nano-fins can develop or form few fins across the whole substrate. With this knowledge these films may be optimised to maximise polarisation effects or surface area.

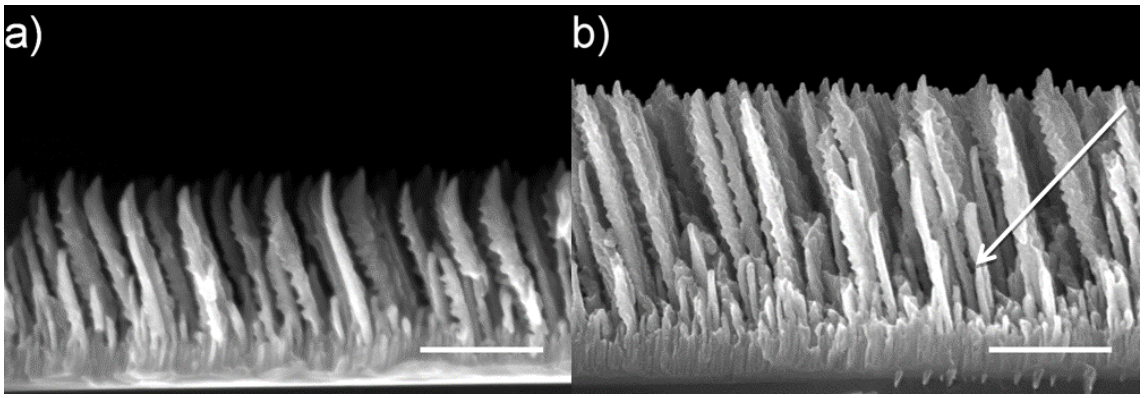

Figure 34 Cross-section SEM micrographs of (a) 30 and (b) 40 minute growth times of Mo-Al nano-fins. Arrow indicates the direction of the aluminium flux. All scale bars are 500 nm[114].

It was noted that the development of a relatively dense layer of ~200 nm thickness preceded nano-fin formation, Figure 34. This could also be seen visibly on samples deposited on glass with the backside appearance resembled a continuous thin film of Mo-Al alloy. The cross section SEM depicts the multiple heights of the fins and the packing density of the nanostructures. Attempts were made to determine the composition of the underlayer, however due to the large spot size of the electron beam for EDS, only the elements in the underlayer were confirmed.

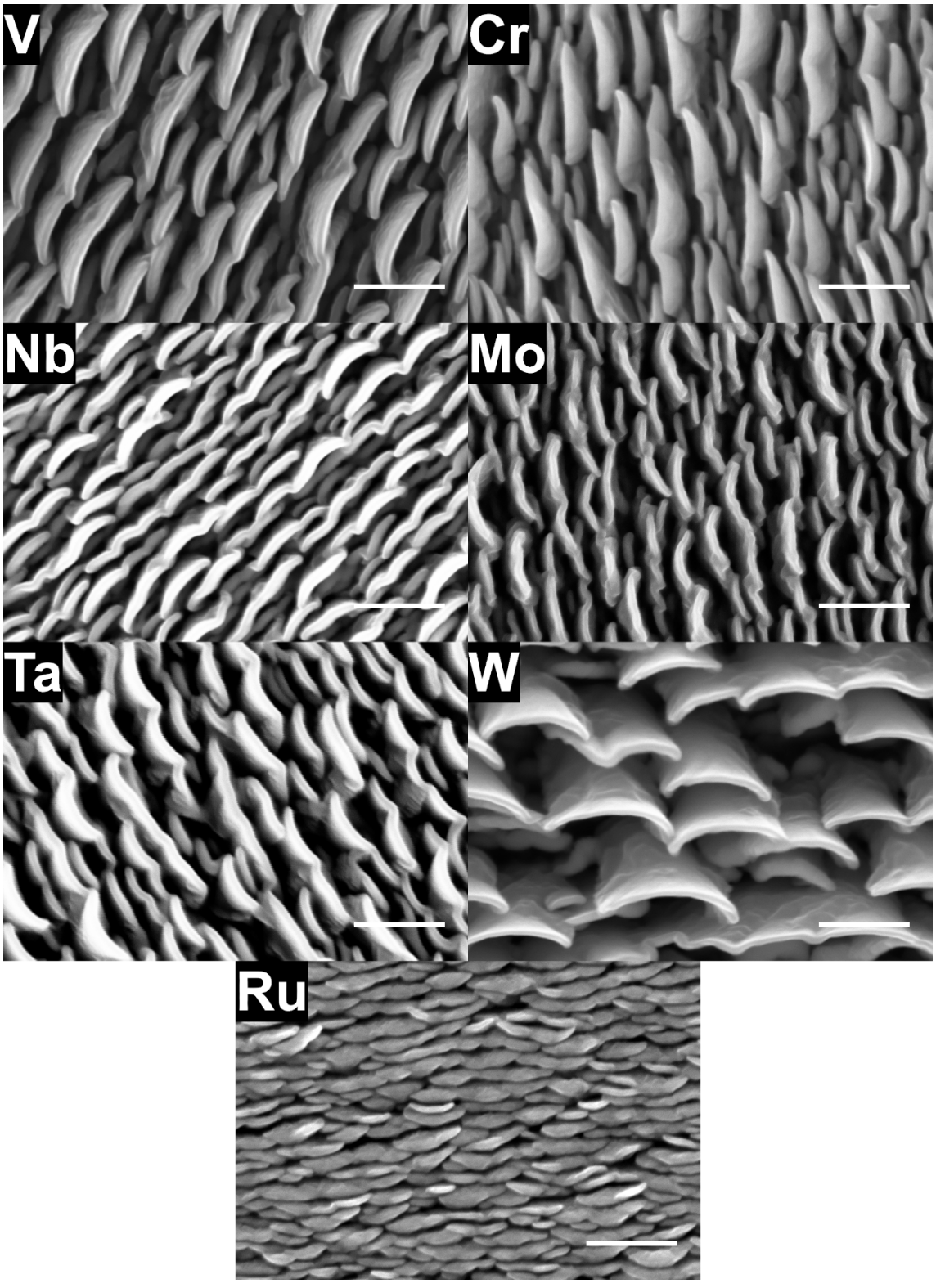

Figure 35 Nano-fins fabricated from a range of refractory metals. Each sample was deposited for 20 minutes, except for Ru (60 minute deposition) and W (30 minutes). All scale bars are 200 nm.

4.3.4 Choice of refractory metals to produce nano-fins

Other refractory metals were tested to determine whether nano-fins would still form. Coatings made with refractory metals such as tantalum, molybdenum, niobium, tungsten, chromium, vanadium and ruthenium are portrayed in Figure 35 as well as nickel, iron, titanium, zirconium and platinum (no image obtained yet). Most of the refractory metal nano-fins assume analogous morphologies with a curved face and varying heights. The nanostructures in Figure 35 for the W sample are much larger than the other samples most likely due to an extended deposition time. Also, different powers were used for each metal in order to produce these structures and the deposition rates differ between each element. Conversely, the Ru sample possesses a unique fin network compared to all the other refractory metals. Figure 36 reveals the nanostructure had shorter and thicker fin-like structures with each piece more closely packed together. The 'fins' in the Ru/Al sample also appear to be of very similar heights. The Ru-Al nano-fins displayed in Figure 36 seem to possess no visible underlayer and resemble the thin columns than the regular nano-fins formed with other refractory metals.

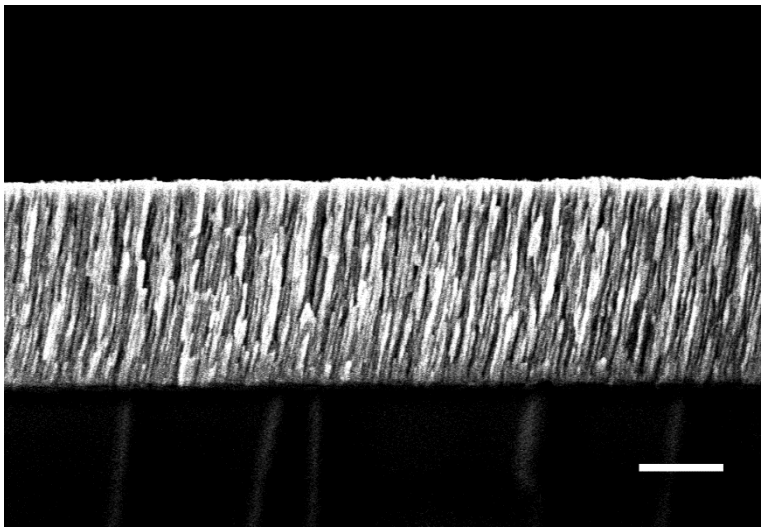

Figure 36 Cross section SEM micrograph of Ru-Al nano-fins deposited for 60 minutes. Scale bar is 500 nm.

4.3.5 Variations of structure with growth times

An investigation into the development of this underlayer and evolution of the nano-fins was performed through a growth study to understand when the structures began to appear. This growth study was done by sputtering onto silicon substrates at times 2, 5, 10, 15, 20, 30 and 40 minutes.

The thin films were then analysed optically (spectrophotometer) and structurally (SEM). The formation of the nanostructures were evident even 5 minutes into the deposition though very sparse. With progressing growth times, the nano-fins developed more readily with the difference between 10 and 15 minutes being the most significant. At 15 minutes (Figure 37a) these features

were abundant but had yet to attain high aspect-ratio. The nano-fins developed further into larger structures with amalgamation of neighbouring columns to form taller features as seen in the 20 minute sample (Figure 37b). At 20 minutes the film reached 'maximum height' and no longer developed directly upwards but began to more heavily tilt in the direction of the molybdenum flux. Longer sputter times produced thicker structures causing greater self-shadowing effects forcing greater angular tilt of the nano-fins.

For the nanostructures fabricated at 30 and 40 minutes (Figure 37c and d) the columns began to fold over and were very similar in appearance. Figure 34 portrays the differences in both films with thickness/height of the samples being the most obvious. The under layer can also be seen in both images resembling structures grown by oblique angle deposition though with much greater column density more typical for the deposition angles expected.

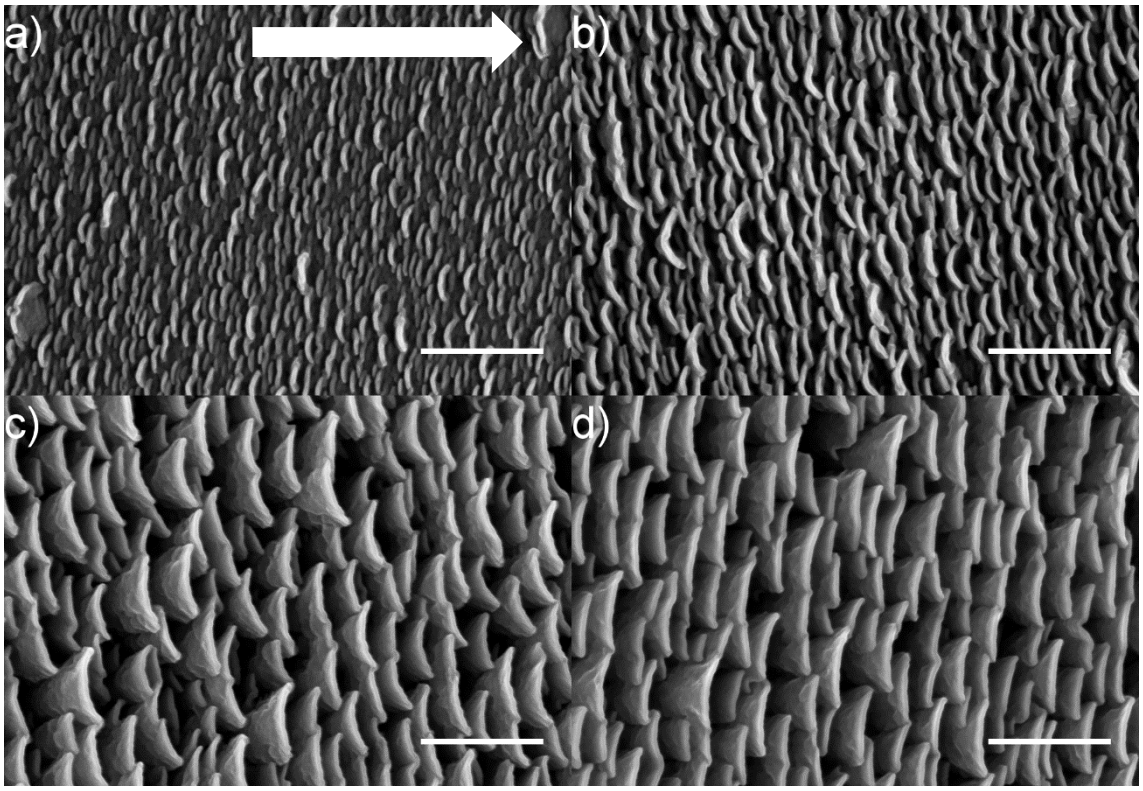

Figure 37 SEM micrographs at (a) 15,(b) 20, (c) 30 and (d) 40 minute growth times of Mo-Al nano-fins. Arrow indicates the direction of the aluminium flux. All scale bars are 500 nm [modified image from publication[114]].

4.3.6 Attempts at different combinations to replicate nano-fins

As noted previously, refractory metals were selected as initial data suggested that high density, heavy metals were required to bond with aluminium to be able to form these fin networks. To confirm this hypothesis, other light metals of similar density to Al were substituted, such as silicon with molybdenum to observe progression of the nanostructures. The SEM images obtained and the

colours of the films did not resemble any of the typical refractory metal nano-fins (Appendix 5). Deposition of one metal (e.g. just molybdenum or aluminium) was investigated to determine whether nano-fins or similar nanostructures would form. Some structures were formed but seemed to reflect crystal growth rather than fin-like structures in the case for either metal (molybdenum or aluminium). Two refractory metals (Nb-Mo) were also co-deposited with the described technique. These samples did not develop structures similar to nano-fins though the structures that were formed resembled those of sputtered molybdenum on a stationary stage. Al-Al was also deposited to determine whether aluminium is the sole driving force to producing nano-fins, however, no structures were formed during stationary stage co-sputtering of Al.

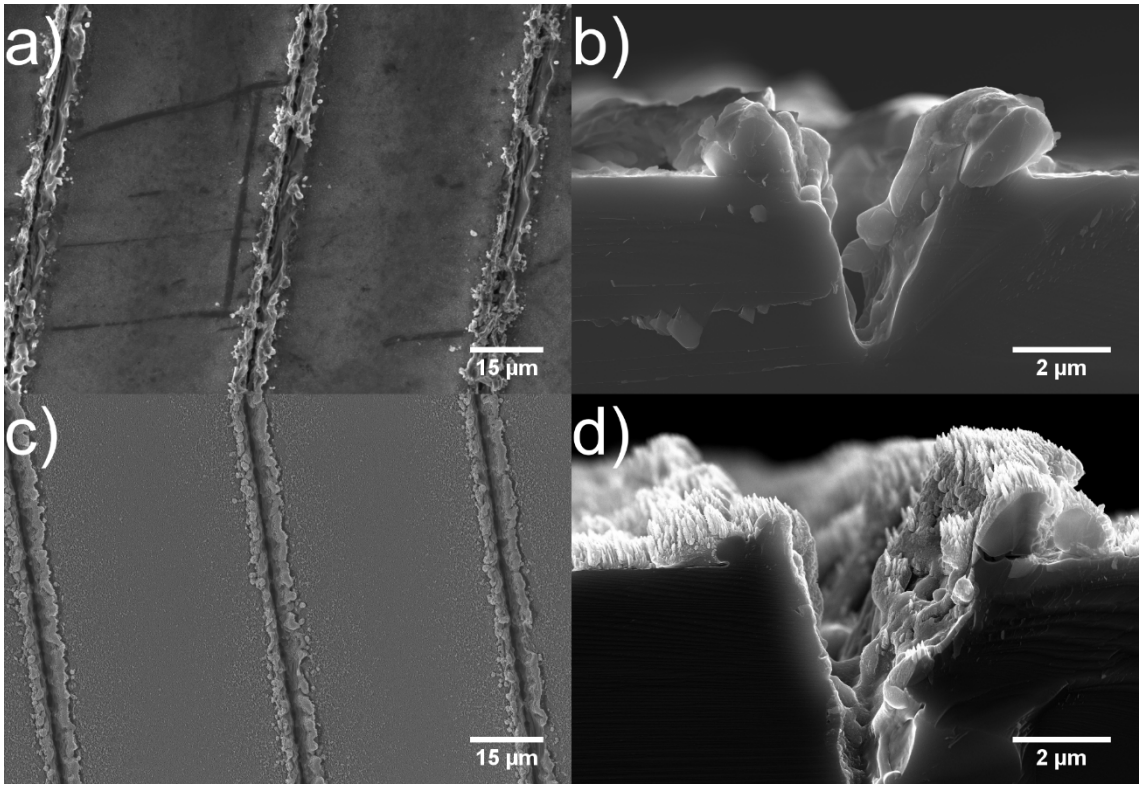

Figure 38 a) Laser ablated lines on silicon substrate spaced apart by 50 µm and approximately 6 µm wide, c) lines after 20 minute deposition of the Mo-Al, b) cross section view of the ablated lines d) after deposition of the nano-fins.

4.3.7 Necessity of co-sputter deposition

Further confirmation that both a refractory metal and aluminium was necessary for the growth of these morphologies was obtained by depositing onto grooved Si substrates, in this case conveniently created with Laser Ablation Inductively Coupled Plasma Mass Spectrometry (LA-ICP-MS). The method involved the creation of 10 lines, 10 mm long, spaced at 50 µm increments, and ablated 10 times using an 8 µm spot moving at 32 µm/s. These lines are presented in Figure 38a as-etched and after deposition in Figure 38c. The cross section views of the lines in Figure 38b and d, exhibit the conical shape of the laser ablated lines. The plan view images also illustrate some of the ablated

silicon re-deposited next to the lines rather than being completely vaporised by the laser. Co-deposition of Mo and Al, as described previously in this chapter, was then performed with the results exhibited in Figure 38c. The nano-fins developed as normal on the silicon substrate and formed on the redeposited silicon produced from the ablation of the lines (Figure 38d). The SEM images also indicated the flux of both metals are necessary as no nano-fin development occurs on the sides of the walls in the ablated lines. Nano-fins were formed throughout the substrate either around the redeposited silicon sites or in areas where a simultaneous flux of both metals is available. If significant shadowing or structures obstruct the incoming flux of one metal, no structure is formed. Within the cavity there was no nano-fin growth providing further evidence that two metals at opposing directions are required for nano-fins to develop.

4.4 Summary

Fabrication of the unusual refractory metal nano-fins was systematically investigated, and the structure was successfully reproduced for a variety of refractory metal elements. Various conditions had to be met in order for the films to grow. Variations in the deposition conditions may significantly affect the shape, size and development of the refractory metal nano-fins. Positioning the substrate to receive both metal fluxes simultaneously was an essential requirement. Altering the gas pressures during deposition also resulted in changes in the shape or development of the nano-fins. The refractory metals chosen provide similar structures, with the exception of ruthenium which generated more closely packed fins. Follow-up work, perhaps using cross-section TEM in combination with elemental analysis techniques could provide valuable information for the exact formation mechanism. Reflection optical measurements indicate the polarizing capability of these films. They also reveal how thickness and changeable deposition conditions may affect their optical features. The specifications described in this chapter demonstrate the tunability of the reflectance and surface area of the ‘newly’ discovered refractory metal nano-fins. Further optimizations of the optical and structural features as well as possible applications of these films will be discussed in the next chapter.

CHAPTER 5 – PROPERTIES OF VARIOUS AS-DEPOSITED AND SELECTIVELY ETCHED REFRACTORY METAL NANO-FINS

Published works featured in this chapter: Tai, M.C., Gentle, A.R., Arnold, M.D., Cortie, M.B., 2018. Nanotechnology 29, 105702. and Gentle, A., Tai, M., White, S., Arnold, M., Cortie, M., Smith, G., 2018. New Concepts in Solar and Thermal Radiation Conversion and Reliability Vol. 10759, p 107590L–10759–10.

5 Chapter 5 – Properties of various as-deposited and selectively etched refractory metal nano-fins

The previous chapter described how a remarkable 'finned' nanoscale metal shape could be made by magnetron sputtering. In the present chapter, the optical and electrical properties of these nanostructured films, demonstrating their use as refractory polarizers, switchable thermal emitters, and capacitors will be explored. Some of the work in this chapter has already been published, specifically the work on refractory polarizers[114] and that on switchable emitters[158]. The basic concepts and motivation for these applications, then any specific measurement techniques necessary, and then wrap-up with an assessment of their performance in the selected applications will be presented.

5.1 Capacitance of the refractory metal nano-fins

Waning fossil fuels and a desire to reduce carbon emissions to alleviate global warming concerns has encouraged electricity production from renewable sources. Due to most renewable sources producing inconsistent power (e.g. the sun sets, wind doesn't blow all the time), stored power can provide constant electricity for areas that rely on intermittent power generation. The main types of energy storage are batteries, however they have long charge and discharge times[159]. Supercapacitors possess rapid discharge/charge times and may be used in applications such as regenerative braking or compact storage devices in electronic circuits. Whereas the ability of a capacitor to store energy is very limited, it can provide a valuable buffering of power. Capacitor charge may be stored either electrochemically (Faradaic), electrostatically (non-Faradaic) or a hybrid of both processes. Carbon-based supercapacitors are generally classed as electric double-layer capacitors (EDLC) caused by the Helmholtz layer whereas metal-oxide capacitors are considered pseudocapacitors. In the latter, a charge develops through electrochemical means (oxidation and reduction of the metal oxide layer)[160].

5.1.1 Types of capacitors

Pseudocapacitors typically have high theoretical capacitance which implies superior energy density in comparison to EDLCs. Electrochemical pseudocapacitance has recently received much attention with various studies involving the use of transition metal oxides[78-81]. Transition metal oxides such as RuO_2[161], MnO_2[162], NiO[163] and Co_3O_4[164] are often selected as the material of choice due to their high specific capacitance values and reversible redox reactions. RuO_2 is mostly selected as it possesses high specific capacitance, however the other materials have been rising in popularity as they are cheaper than ruthenium and provide similar specific capacitance.

The ability to produce high surface area nanostructured thin films grant may facilitate the fabrication of capacitors capable of charging and discharging quicker than the average commercial capacitor. Besides the nano-fin structure already mentioned, achieving high surface area is possible through selective etching of precursor alloys[4,44,165,166]. Other methods for producing high surface area nanostructures include: coating/templating/transferring to a nanoporous material[3,167,168], electrodeposition/anodization[169] and powder/liquid mixtures[170,171].

Refractory metals are well known for their high temperature stability and corrosion resistant properties (although not necessarily both properties simultaneously). These features of refractory metals have led to applications as diverse as biomedical implants[14] and fusion reactor walls[15]. Oxidation of these metals alters the electrical properties to become more semiconductor-like as well as changing the optical properties. In some cases this is deliberate: a combination of oxide and metal are useful for capacitors[16] and gas sensors[17,18], for example. Nanoporous metals of the refractory metals and others, whether oxidized or not, have also found significance in capacitors[3], sensors[4] as well as catalysis[1,5] due to the significant increase in the surface area. However, most nanoporous metals that have been produced are comprised of noble metals (Au, Ag, and Pt)[7-9]. Refractory metals oxides have also been selected and fabricated with nanoporous networks, though most are produced through template methods[19] or anodization[20-23]. Selective dissolution is another method to constructing such nanoporous networks in metals[24].

Refractory metal polarizers have also been applied for extreme ultraviolet[172,173] regions, however in this chapter the viability of these structures as broadband polarizers in the visible spectrum will be discussed.

5.2 Radiative cooling

Research into radiative cooling has been conducted for many decades[174-178], though due to increasing energy costs and the need for more renewable energy sources, recent advancements in day-time sub-ambient cooling[179-181] have led to many groups searching for materials that allow low temperatures to be attained in full sunlight. A typical strategy is to aim for very high solar reflectances, rather than optimisation of the radiative aspects of the cooling surface. The main focus here will be on broader aspects of control of radiative cooling, but the measurement techniques discussed are applicable to various radiative cooling applications. Metal nano-fins not only extend the range of effective refractive indices for impedance matching, but could also offer strong angular response, both of which are desirable properties for absorption and emission control. For some applications certain angles or even wavelengths are desired to be absorbed or reflected. In the case of solar absorbers, wavelengths within the solar range must be absorbed whereas longer thermal

wavelengths should be reflected. Solar absorbers also possess broad angular selectivity to take in as much light as possible.

The application of switchable optical properties has also been a growing area of research, with materials such as vanadium dioxide (VO_2) being widely studied. Great efforts have been made to control the solar properties of coatings and alter the transition temperatures through various means (including doping and strain)[182,183] as well as some work on modulating the infrared emission[184-186]. Oxidation of vanadium nano-fins to produce thermochromic VO_2 is therefore a natural avenue of investigation in this thesis.

Here the various measurement techniques required to accurately determine the optical/thermal response of such systems will be discussed. These measurement techniques apply to both switchable and non-switchable emissive surfaces.

5.2.1 Emissometers

Broadband emissometers[20,187] measure integrated reflectance of a black body using a thermopile. This method holds the sample at room temperature, while the reflectance from a heated cavity around 80°C is measured with a thermopile. The blackbody spectral distribution at 80°C rather than 25°C can cause a shift in attained emittance when samples have sharp spectral features, as is often the case for radiative cooling. There are various embodiments of such systems, but typically such measurements of specular surfaces yields the near-normal incidence emittance. Conversely for a diffuse sample a reasonable approximation of the hemispherical-normal emittance is measured, which is the reverse of the flow that is measured with an integrating sphere (normal-hemispherical reflectance).

5.3 Electrical measurements on Mo-Al and Ru-Al nano-fins

The samples used to investigate the capacitance were fabricated using the same process as for the optical work. The nano-fin samples were compared to deposited solid films of the same elemental composition (Ru, Mo, Al, Ru-Al and Mo-Al). Electrical values were measured in the experimental set-up demonstrated in Figure 39 in an electrolyte solution up to 1 M of NaCl. An electrical setup, shown in Figure 39, was constructed using a Yokogawa GS610 power supply, controlled via a LabVIEW script to control the output voltage as well as read and store the current. Samples were initially charged until they stabilized and charged for a further 300 charges for complete stabilization with the capacitance calculated using the LabVIEW script. Cyclic voltammetry tests were conducted with another LabVIEW script. Voltages were cycled between -1.5 – 1.5 V and scanned at a rate of 50

mV/s, using the same solutions in the experimental set up as before. Morphological characterisation and the thicknesses of the films were viewed in plane and cross section SEM by a Zeiss Supra 55VP.

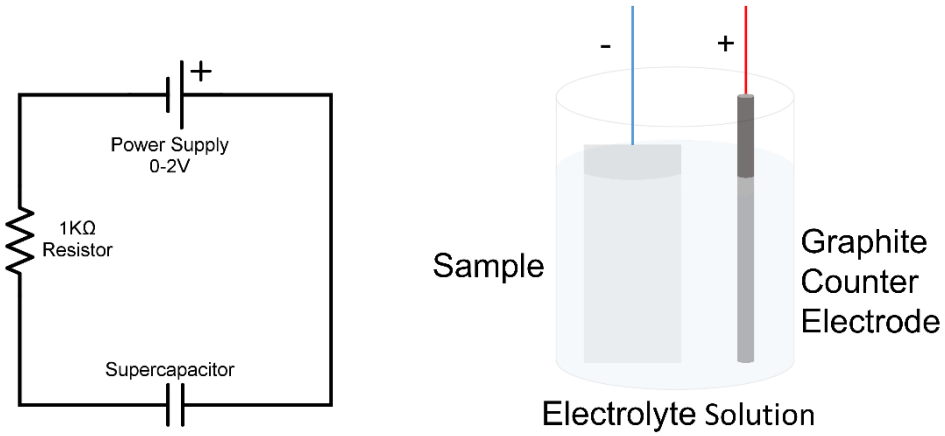

Figure 39 Left: schematic of the electrical circuit constructed to measure the electrical properties of the supercapacitors. Right: zoomed in diagram of the supercapacitor.

5.3.1 Capacitance and longevity

Each sample was charged for over 300 charge-discharge cycles and after the first few cycles the nanostructured thin films became very stable. Further cycles were tested for the nanostructured films, with the stability of the films at holding charge exceeding 1000 cycles. Charge-discharge curves were fitted with a double exponential:

$$V_{capacitor} = A + Be^{Dt} + Ee^{Ft} \qquad (2)$$

where A is the DC offset, B and E are the voltages and D and F are the 1/RC values (R is the resistance of the current limiting resistor (1067Ω) circuit and C is the capacitance value of one of the exponentials). Equation 2 was used to determine the capacitance of the thin films within a LabVIEW script.

5.4 Temperature stability tests

The Mo-Al nano-fins were tested in an annealing chamber with *in situ* optical monitoring. The samples were annealed from 670°C to 1000°C. This chamber and a schematic will be discussed in more depth later in this chapter.

The etched nano-fins were analysed with a J.A. Woollam V-VASE Ellipsometer in reflection and transmission ellipsometry. Thermal stability studies were also observed in the ellipsometer fitted with a Janis ST-400 UHV Supertran system at high vacuum (better than 10^{-8} Torr) and temperatures

elevated to 700 K from room temperature at a rate of 10 K min^{-1} with a full spectroscopic measurement performed at 300, 500 and 700 K.

5.5 Surface modifications on the nano-fins

Various techniques were employed to modify the nano-fins depending on the selected refractory metal. In most cases, the applications that were investigated would require chemical etching and removal of the Al in the nano-fins. The nanostructured films were produced by selectively etching the nano-fin precursor alloy in 1 M NaOH for approximately 15 minutes. The samples were then rinsed with deionised water and dried with nitrogen. Further surface modifications were conducted, specifically oxidation of the vanadium nano-fins to produce VO_2.

5.6 Fabrication and oxidation process of VO_2

The VO_2 surfaces were produced via DC magnetron sputtering of metallic vanadium followed by an oxidation process. Planar and nanostructured VO_2 were fabricated and compared.

5.6.1 Preparation of vanadium thin films

Metallic vanadium thin films of 50 nm thickness were sputtered from a 50 mm, 99.99% purity vanadium target in a 2.7 mTorr Argon atmosphere at room temperature, in a vacuum chamber with base pressure of $1x10^{-6}$ Torr, using a quartz crystal thickness monitor to ensure thickness repeatability. Vanadium was deposited using sputtering energies shown in Table 2. Thicknesses were calibrated via ellipsometry prior to oxidation.

5.6.2 Nano-fin V-Al

The nano-fin structured V-Al was produced by DC magnetron co-sputtered in a high vacuum chamber at base pressures better than 2.0×10^{-5} Torr with a similar recipe as described in the previous chapter. Sputtering energies for nano-fin V-Al is shown in Table 2. Samples were deposited at various time lengths of 20-60 minutes (thicknesses ranged from 250 to 1200 nm) to determine optimal thicknesses and tunability of thermal emission.

5.6.3 Oxidation of metallic precursor

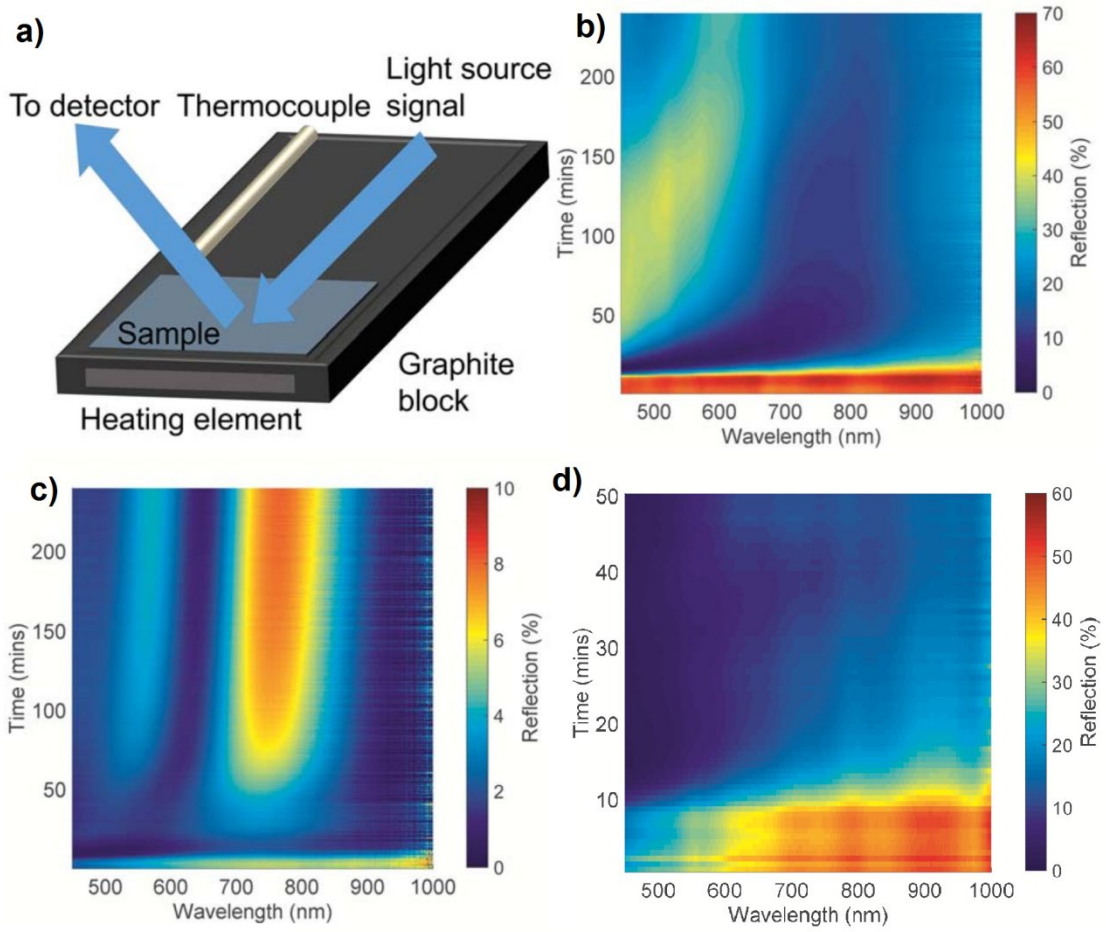

Figure 40a) Experimental set-up of the annealing chamber for in situ monitoring of the oxidation process via reflection measurements. A graphite stage with an embedded heater and thermocouple are used to control the sample temperature. A fibre spectrometer was used to observe the change in reflection. b) In-situ reflection measurements on a 50 nm thin film vanadium on a silicon substrate at 450°C, c) In situ reflection measurements on nanostructured thin film vanadium-aluminium deposited for 30 minutes. d) In-situ reflection measurements on thin film vanadium on glass annealed at 550°C.

Each of the samples was oxidized in an annealing chamber with in-situ optical monitoring. The chamber was first evacuated with a scroll pump with the pressure controlled via a computer controlled flow controller. Ambient air was introduced to a stable pressure of 0.3 Torr, and once stable the sample stage was increased to a preset temperature and maintained for the duration of the oxidation process. In situ reflection measurements were taken by an Ocean Optics USB2000 every minute throughout the oxidation process. For the reflectance measurements a 5 mm diameter collimating and 25 mm diameter collection lenses (Ocean Optics 84-UV-25) were used, leading to a 10 mm diameter sampling area. The light source and detector were each positioned at 15° either side of normal incidence to the sample.

As V_2O_5 is the most stable vanadium oxide if annealed at atmospheric pressure, to attain VO_2 a lower partial pressure of oxygen must be used. A range of pressures and oxidation temperatures were investigated. The most repeatable films with good switching properties were attained with an atmospheric pressure of 0.3 Torr and a temperature between 450°C (250 minutes) and 550°C (20 minutes). At 450°C, even annealing for up to 24 hours was tested and the typical transition behaviour in VO_2 still persisted.

5.7 Infrared optical analysis techniques

5.7.1 Infrared Ellipsometry

The use of ellipsometry within the infrared spectral range has added benefits for the characterization of specular surfaces. The FTIR spectrometer was retro-fitted (by Dr Angus Gentle) with two stepper controlled infrared wire grid polarizers to allow a custom written LabVIEW program to conduct temperature dependent, multi-angle ellipsometry across the infrared range. A limitation was that the samples must be specular in nature and a specific size for large angles due to the large beam/spot size.

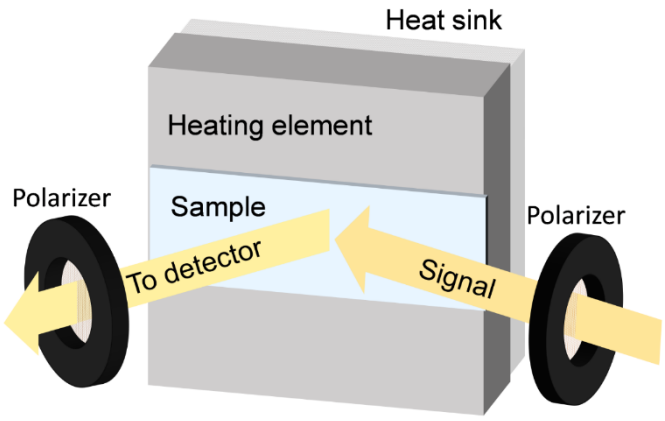

Figure 41 FTIR equipped with temperature stage, and polarizers allowing it to function as an ellipsometer.

5.7.2 Thermal Emission measurement

Utilising a calibrated infrared thermopile and a temperature-controlled stage, it was possible to determine the emittance of a surface. Generally infrared thermopiles are limited to the 7-14 μm to match room-temperature emission which conveniently matches the spectral range of the "sky window". This means that temperature dependent sky window emittance, $\varepsilon_{skywindow}(T)$, could easily be determined. An infrared detector was fixed onto a goniometer to allow for the emittance to be measured across a range of emission angles as well as temperatures. Computer control enabled sweeps through either sample stage temperature or emission angles, or scans across a range of

angles throughout a series of temperatures. Full mapping and analysis of the thermal emission from a surface was automated.

It is important to take into account both the sample temperature and reflected temperatures at each angle in order to accurately determine the emittance of the surface being tested. The selected infrared sensor returned temperatures measured in Kelvin, therefore Equation 1 was used to determine the emittance of the sample at each angle ε(θ) and temperature.

$$\varepsilon = \frac{T_{IR}^4 - T_{reflected}^4}{T_{sample}^4 - T_{reflected}^4} \quad (1)$$

The results presented here use a CALEX PMU201 PyroMiniUSB infrared thermometer with 20:1 optics with a normal incidence spot size of approximately 10mm. Measurements corresponded to, $\varepsilon_{skywindow}(T)$ due to the spectral response of the detector.

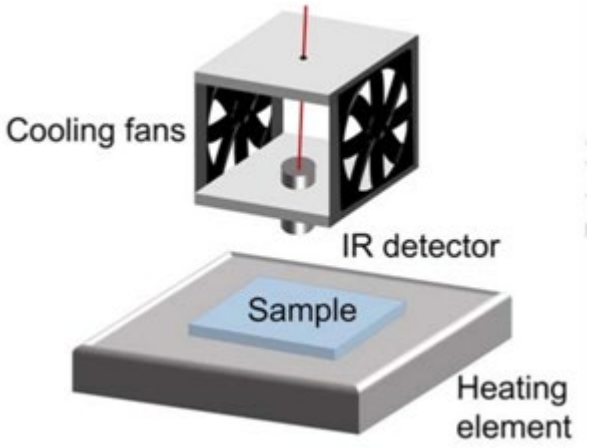

Figure 42 Schematic of the emission based emissometer.

Thus by determining the emissivity of a surface at various temperatures, the integrated thermal power radiated from a surface can then be calculated via Stefan–Boltzmann law, $P_{out} = \varepsilon \sigma T^4$.

5.8 Electrical properties of the nano-fins

As discussed in previous chapters, refractory metals are relatively corrosion resistant implying that when these thin films are placed within a NaCl solution, a passivation layer is formed which protects the metal. This also explains the stability of these 'supercapacitors' for thousands of cycles. Figure 43 depicts the differences in capacitance of various films, with the nanostructured samples capable of

holding more charge due to the nano-fins which means the surface area greatly increased compared to the uniform thin film molybdenum. The cyclic voltammetry measurements can also explain whether a reduction-oxidation reaction causes the ability to hold charge in the thin films. The cyclic voltammetry results in Figure 43 do not show any pronounced faradaic redox peaks which are typical indications of reduction-oxidation reactions. This suggests that a charge develops from surface adsorption of ions only. The combination of a high surface area and the native oxide formed over a conductive backbone in the nano-fins provided a larger enhancement than from typical uniform thin films. This also explains the longevity of these supercapacitors as there is not structural or chemical changes but rather just adsorption of ions. A double exponential (Equation 2) can also be explained by initial charge dissipation from the ions adhered to the surface of the nano-fins and then the next layer of ions within the nano-fins. This charge transfer method is very similar to that of batteries. Once the thin films were removed from the salt solution they were rinsed and dried to be tested again for stability with some charge retained in the thin film (the retention of charge can be seen compared to initial charge in Appendix 6).

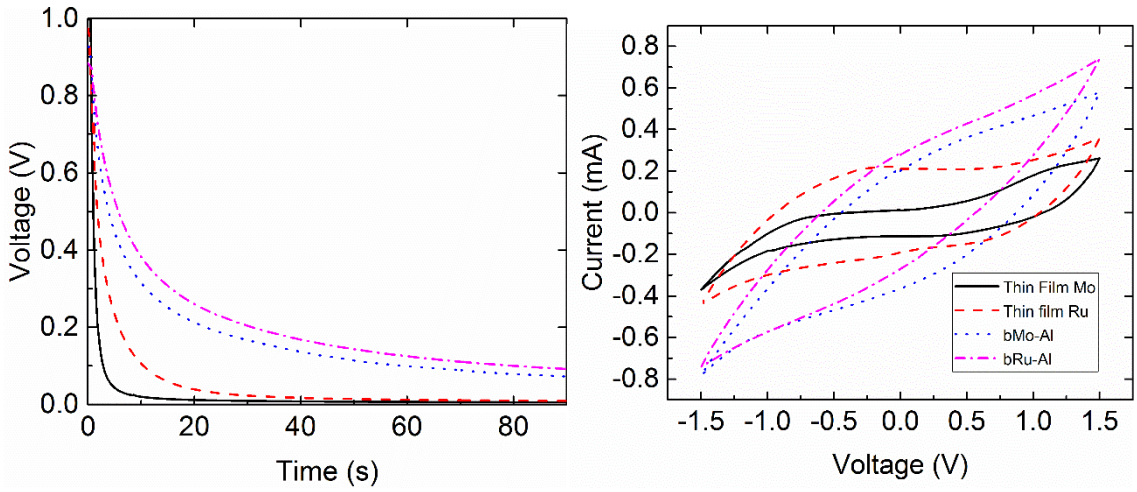

Figure 43 Left: comparison of the discharge in the samples over time, right: comparison of the cyclic voltammetry for the thin films.

Ruthenium and its oxides are widely accepted to be the most optimal supercapacitor material. This metal was selected and compared to molybdenum as the nano-fins were first produced with this refractory metal. Firstly, uniform thin films were compared to the nano-fin counterparts (Figure 43). For the ruthenium samples, a four times enhancement from the uniform ruthenium thin film (0.73 mF/cm^2) to the nanostructured Ru-Al (2.75 mF/cm^2) was found. Molybdenum had a much more significant enhancement, with an increase of over 22 times from the uniform thin film (0.097 mF/cm^2) to the nano-fin molybdenum (2.16 mF/cm^2). However, the absolute capacitance of the ruthenium was greater than the molybdenum but due to the high cost of ruthenium compared to

molybdenum, it would be most cost efficient to utilise molybdenum nano-fins as supercapacitors. The nano-fin molybdenum electrodes have a capacitance three times higher than the planar ruthenium reference electrodes, demonstrating the use of molybdenum nano-fins as electrodes in "sea-water" supercapacitors.

5.9 Optical and thermal properties of refractory metal nano-fins and resultant etched nano-fin

Since the nano-fins consist of refractory metal and could be expected to operate at elevated temperature, in this section stability of the coatings and the likely changes in their optical properties at elevated temperatures are investigated. As elevated temperature will promote oxidation and this will obviously also change the optical properties, samples were tested under vacuum conditions in order to focus only on structural changes driven by metal diffusion. The properties of the coatings is also strongly influenced by whether and how any prior Al content had been removed. Therefore, effect of the dissolution of Al on the resulting properties is also investigated.

5.10 Thermal stability of the Mo-Al nano-fins

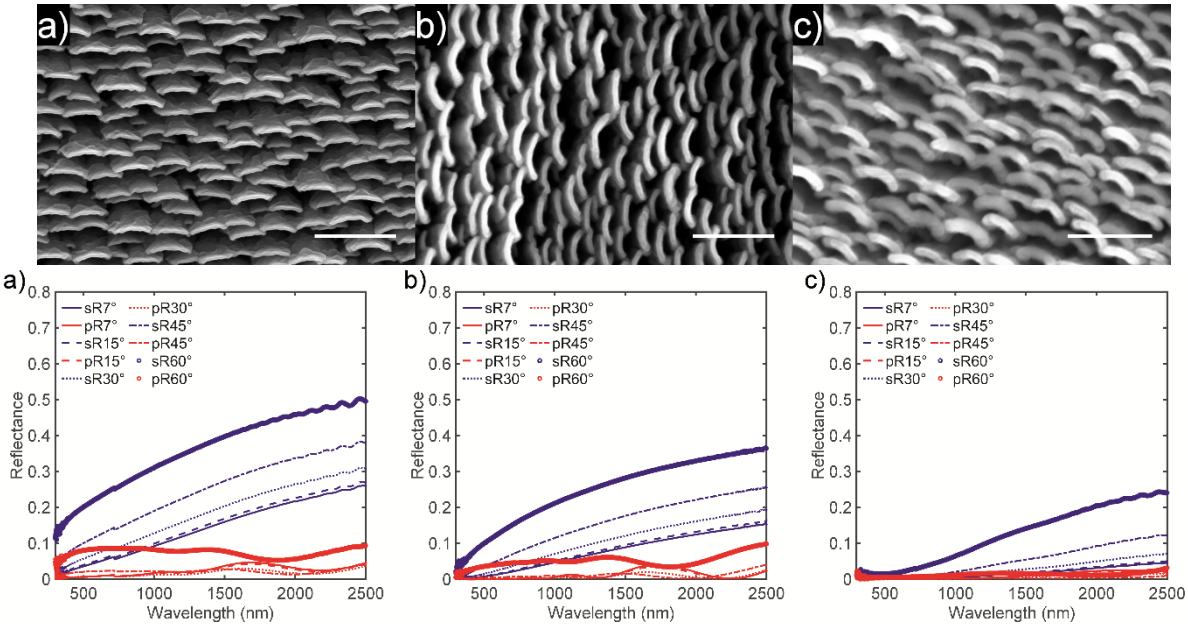

Figure 44 SEM images and s- and p- polarized reflectance at angles 7°, 15°, 30°, 45° and 60° of Mo-Al nano-fins at a) as-deposited, b) 670°C and c) 750°C. All scale bars are 500 nm.

Figure 44 shows the changes in the morphology and reflectance of these Mo-Al nano-fins as temperatures are increased up to 700°C. The temperature was taken further to 1000°C but a SEM micrograph could not be obtained as the sample was destroyed at such high temperatures. Between the as-deposited and 670°C annealed samples, the reflected p-polarized measurements are almost identical, with slight variations at lower wavelengths. The nanostructures in Figure 44a and b, are

similar though the 670°C annealed sample is slightly thicker with rounded edges. The most evident changes are with the 750°C annealed sample (Figure 44c). Structurally, the nano-fins are much thicker and more curved with more rounded edges. Both the reflected s- and p-polarized light decrease with the reflected p-polarization below 5% reflection. This decrease in the reflectance could be due to oxidation of the nano-fins (due to weak vacuum) or simply just diffusion of the atoms.

5.11 Thermal stability of etched Mo-Al nano-fins

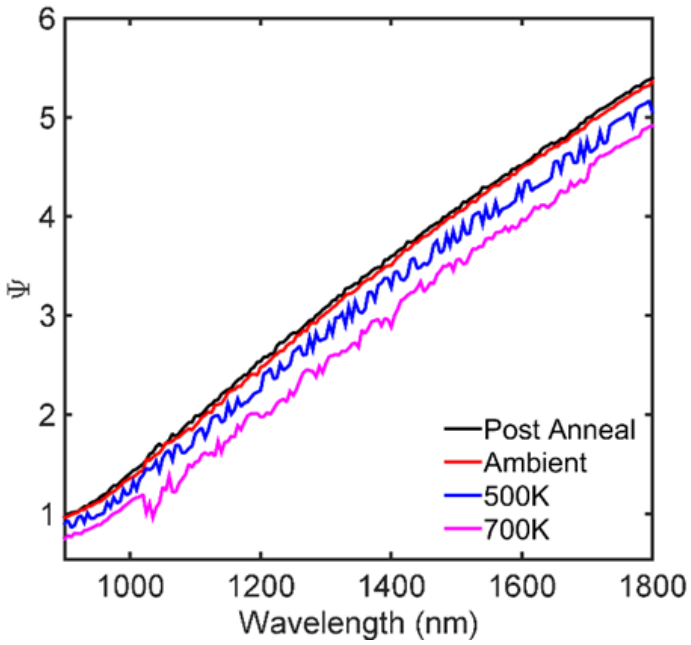

Figure 45 In situ raw ellipsometry data observed at various temperatures.

Residual molybdenum within the underlayer possesses a high melting point (2623°C), suggesting the etched nano-fins would be thermally stable. To confirm this, the thermal stability of the etched nano-fins, was tested by heated ellipsometry and the optical changes as temperature increased. The sample was heated from room temperature (295K) to 700K at high vacuum with pressures $<10^{-8}$Torr. The maximum annealing temperature was limited by the melting point of the glass substrate. Figure 45 depicts the change in Ψ as the temperature increases at wavelengths above 950 nm. An optical model was generated in WVASE32 to understand the changes in Ψ at high temperatures. The residual metal after de-alloying was determined by EDS to be primarily molybdenum. The refractory metal nano-fins were measured via ellipsometry and spectrometry, with the optical constants fitted using a Gaussian-Drude model to determine the 'bulk-like' optical properties of the under layer which consisted of Mo-Al. This previous base-layer Mo-Al model was used in conjunction with a biaxial Bruggeman effective medium approximation to simulate voids within the molybdenum nanostructures. By only altering the resistivity in the Drude model, the changes in Ψ caused by the

heating of the sample were fitted (Appendix 7). The resistivity obtained from the Drude model ranged from 3.29 to 3.69 X 10^{-5} Ω cm over the temperature range. These temperature dependent values are comparable to the resistivity found in other molybdenum thin films[188,189]. This investigation also demonstrates that the sample does not undergo a permanent structural change, rather a temperature dependent one, as it reverts close to its original state (as the ambient and post-anneal Ψ values are close to identical).

5.12 Transmission polarizability of the etched Mo-Al nano-fins

Visibly all the samples were a dark purple-black colour except for the 15 minute sputtered sample, as this film was patchier due to a more defined gradient between nano-fin formation and flat Mo-Al alloy. Samples deposited for ≥20 minutes progressively became darker as illustrated by the decrease in the p-polarized light across the visible spectrum in Appendix 8. The polarization effects of these nanostructures can also be seen in the optical data, with the difference between the two polarizations approaching a ratio of >80 in the 20 minute sample in Figure 46b. The ratio of the two polarization states is defined as the extinction ratio, in this section the transmission extinction ratio is discussed. For the 30 and 40 min samples displayed in Figure 46c and d, the extinction ratios are quite similar with only small changes, this is due both reflected polarizations decreasing as the growth times were increased. However, as the reflected p-polarized light was already very low (less than 10%) the reduction in the s-polarization leads to a smaller extinction ratio as the thickness/growth times increased. This polarization effect arises from the structural anisotropy where light is mostly reflected when the electric field is perpendicular to the nano-fins and strongly absorbed when parallel.

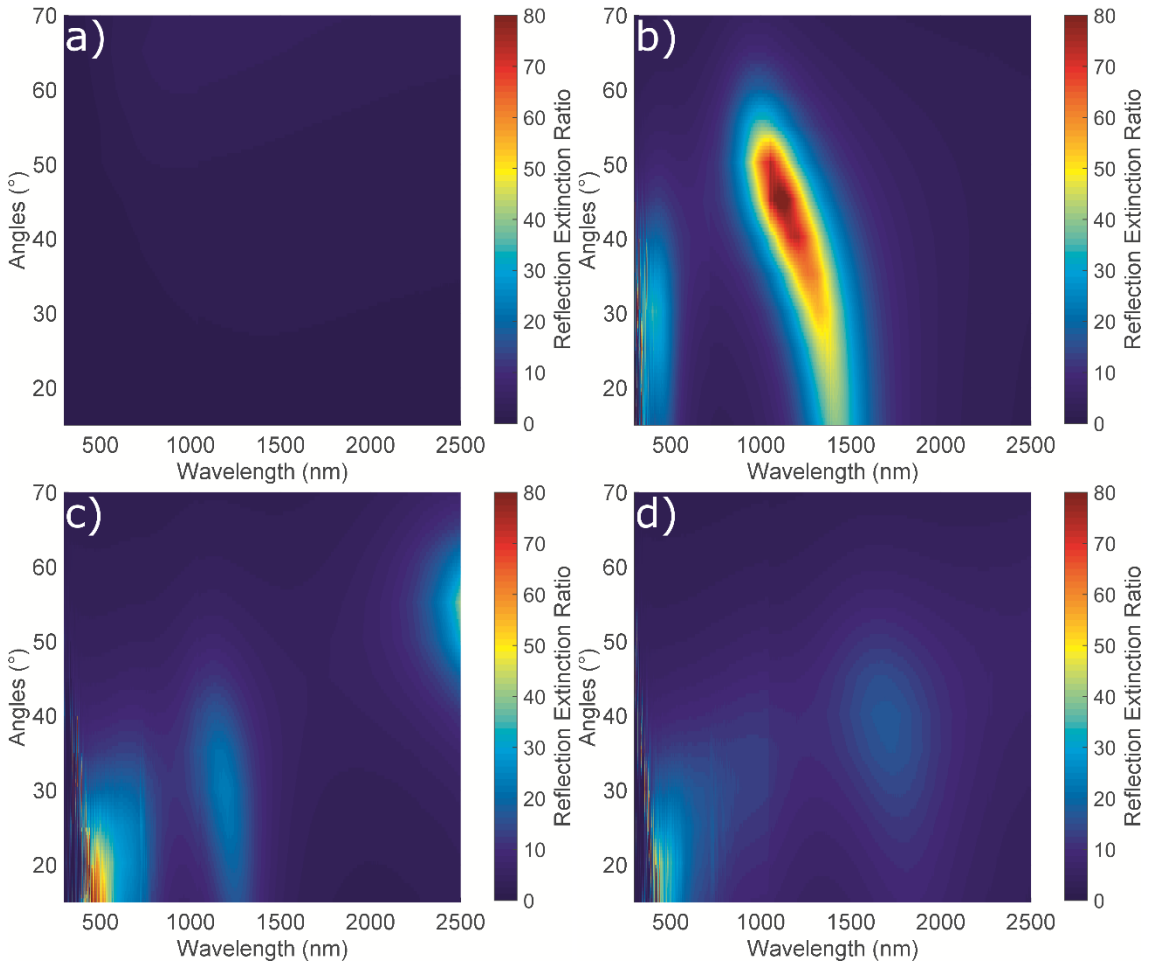

Figure 46 Reflection extinction ratios calculated from s- and p- polarized reflectance data scanned at 300-2500 nm between 10-70° at (a) 15,(b) 20, (c) 30 and (d) 40 minute growth times of Mo-Al nano-fins.

The polarizability of these nanostructures was investigated further to compare extinction ratios to those of commercial linear glass polarizing filters (the latter being typically in the range 1:100) within similar wavelength ranges. It was suspected that removal of the Al by de-alloying would improve the thermal structural stability and transparency of the nano-fins. After selective dissolution of the aluminium, there was restructuring of the morphology of the nano-fins, which resulted in even greater alignment. The optimum transmission extinction ratio achieved was greater than 1:100 in the range 500 to 1100 nm. The removal of aluminium and the movement of the molybdenum to fill the gaps results in the semi-uniformity seen in Figure 47. The gaps in between the nano-fin growth were as large as 200 nm wide and varied, usually being at least a micron in length. These large crevices resembled cracking from stress during de-alloying, though further investigation is required to understand the formation and movement of the elements within the alloy.

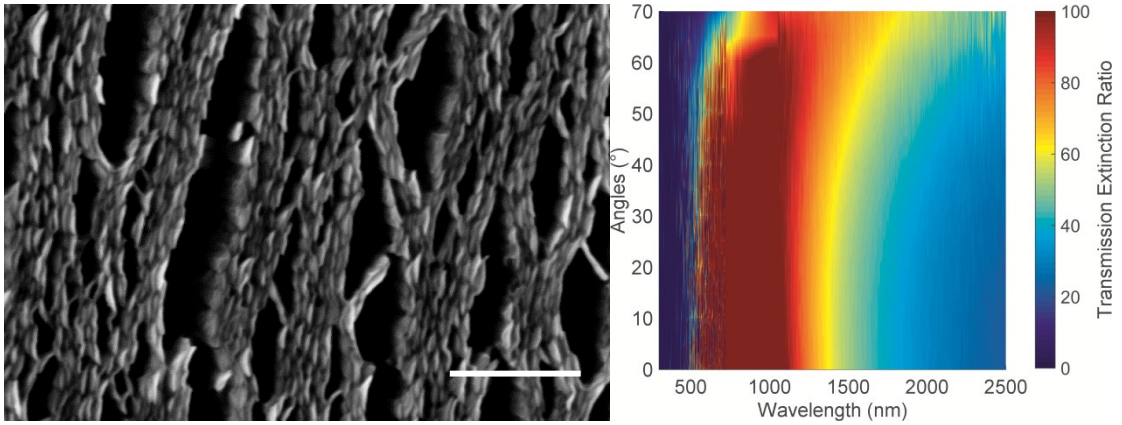

Figure 47 SEM micrograph (left), and the optimal transmission extinction ratio (right) of selectively etched nano-fins. Scale bar is 500 nm.

5.13 Optical analysis of uniform and nanostructured thin films of VO_2

5.13.1 In-air heated ellipsometry

After sample fabrication, samples were first measured on a Woollam V-Vase Ellipsometer with a custom-built in-air temperature stage to observe the optical properties at room temperature up to 90°C. Planar thin films of VO_2 were used to fit an oscillator model consisting of a combination of Tauc-Lorentz, and Lorentz oscillators for the room temperature semi-conducting phase, with the high temperature phase consisting of Tauc-Lorentz, Lorentz and Drude oscillators (Appendix 9). A biaxial effective medium model [114] was used for the nanostructured VO_2.

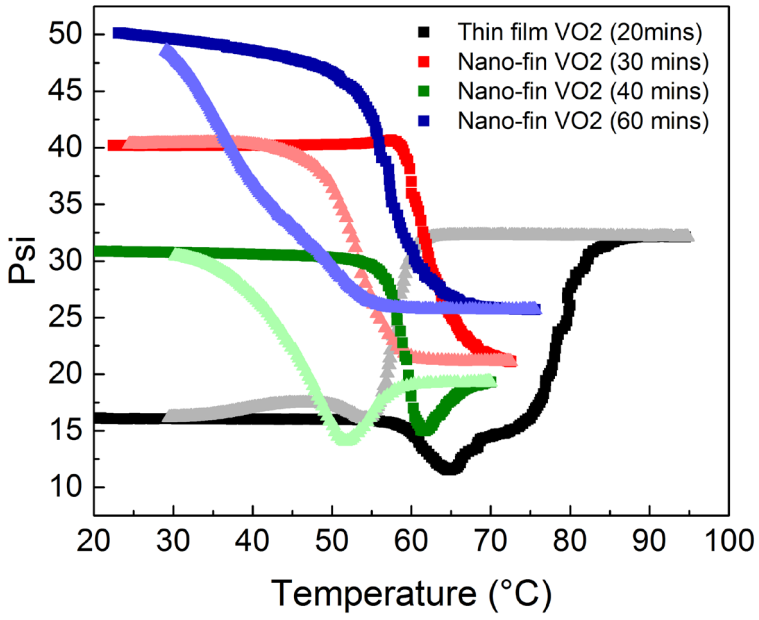

Figure 48: Hysteresis of the VO_2 films as measured by ellipsometry (2500 nm), lighter colour is the change in psi when cooling.

The thin films were placed onto the ellipsometer temperature stage and heated to observe the insulator-metal transition (IMT) at multiple wavelengths ranging from UV/Vis – IR. The hysteresis of psi plots differ greatly between thin film VO_2 and nanostructured VO_2, as seen in Figure 48. An increase in psi is observed for the planar thin films, as expected due to the Drude response of the metallic state, whereas the opposite effect occurs for the nanostructured thin films. This phenomena is caused by the nanostructures once they transition from insulator to metal. A plasmonic response caused by the nano-fins results in absorption of wavelengths in the infrared range. Thus by tuning the thickness of the nanostructured thin films, the emissivity and plasmonic resonance can be shifted to alter the change in emissivity.

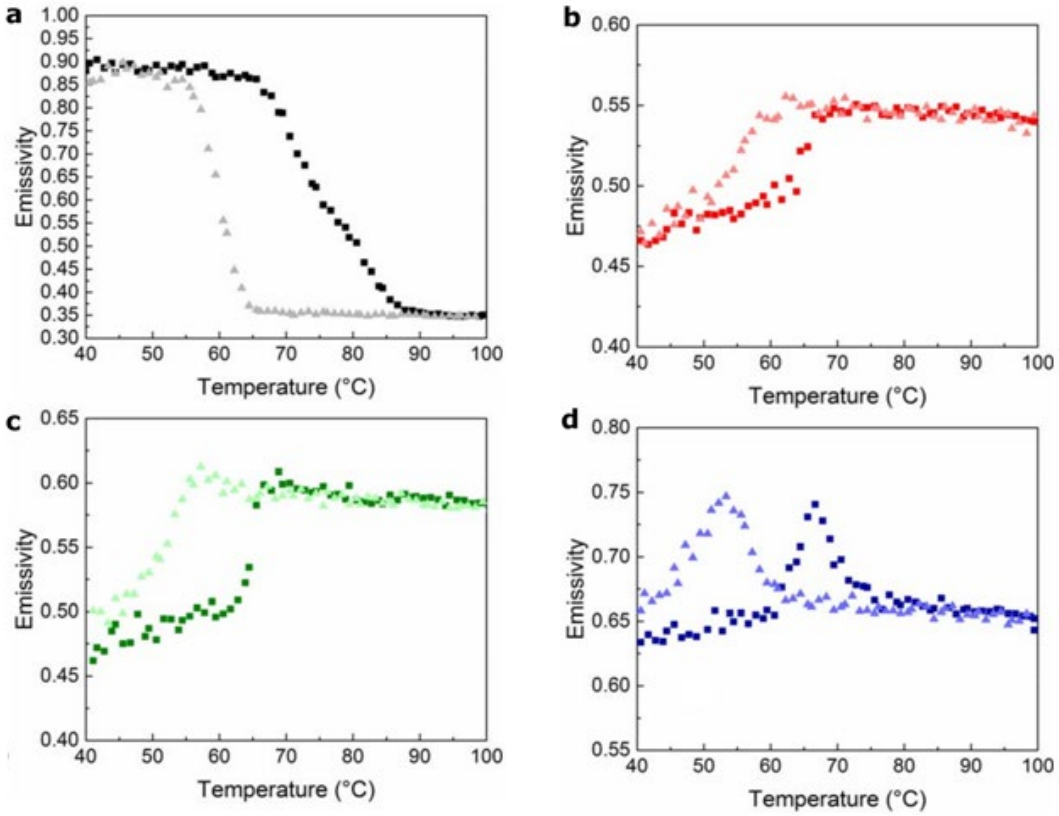

Figure 49: Normal incidence temperature dependent emissivity of (a) planar VO_2, (b-400 nm, c-800 nm, d-1200 nm) various thickness nanostructured VO_2 samples, showing some of the possible emittance profiles.

An optical model was produced to fit the ellipsometric data obtained so that the optimal thickness and parameters could be found (Appendix 10). Data acquired on VO_2 at room temperature and after the transition temperature were used to fit the data of the thin film VO_2 within the solar and infrared ranges. The optical data assessed by the ellipsometers were combined and a basic optical model fitted to the 300-3500 nm range to ensure the previous VO_2 model worked for these samples. The IR section of the ellipsometric data was appended to the fitted UV/Vis section of the data and

oscillators were added to fit the data in the IR. Once an adequate fit was produced for the thin film VO_2, the nanostructured thin films were then fitted. This optical model also simulated the structures that were produced on the nanostructured thin films. A biaxial effective medium approximation was used to simulate the anisotropic nature of these films in conjunction with a gradient graded layer as the nano-fins taper. Thicknesses of the nanostructured thin films were estimated with cross-section SEM and used as initial values for the fitting software. The resultant model was then used to simulate potential samples with similar structures to determine the optimal thicknesses.

5.13.2 Temperature Dependent Emissivity (via thermal emission measurement)

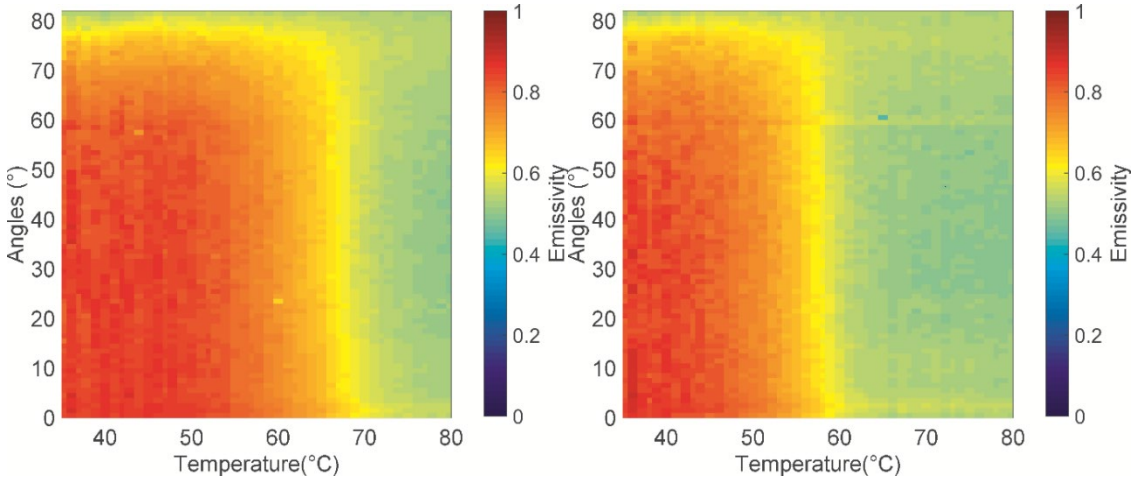

Figure 50: Angular dependent emissivity ε(theta) of planar VO_2, during heating from 35 to 80°C (left) and cooling from 80° back to 35°C (right)

By varying the morphology from planar films to nanostructures of various thickness, we were able to fabricate samples of varied thermal emittance responses. Planar thin films of VO_2 show the typical variation, from high emittance to low emittance upon heating to the metallic state.

An interesting variation in angular emissivity is seen for the smooth thin film samples upon the transition from insulator to metallic state, Figure 50. In the hot (metallic) state less angular variation is observed than that of room temperature. It is often not necessary to undertake a full matrix scan as seen in Figure 50, with a normal incidence temperature (Figure 49), and angular (Figure 50) scans at both hot and cold states being sufficient for routine measurements.

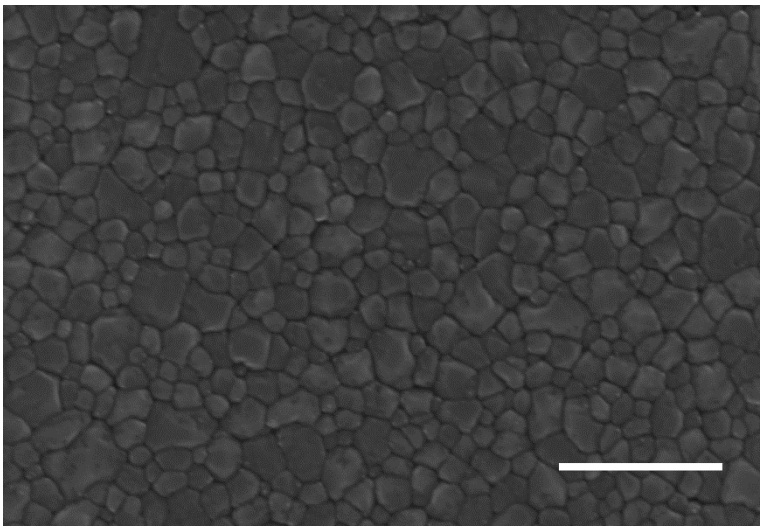

Figure 51: SEM image of 100 nm thick Planar VO_2 (500 nm Scale bar)

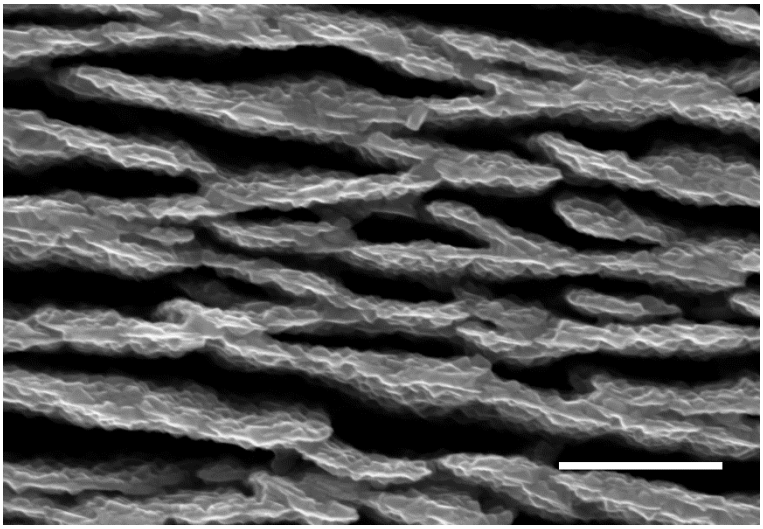

Figure 52: SEM image of a typical nanostructured VO2 thin film on glass. (Scale bar 500 nm)

Figure 51 shows the surface of the VO_2 thin films produced and how they differ from the distinct oriented nature of the nanostructured VO_2 films depicted in Figure 52. These spontaneously formed features were used earlier to produce refractory polarizers in the visible range[114] and can be exploited to alter the thermal emission from a surface. An example of the variations in angular emission is shown in Figure 53. In this case, at room temperature the emissivity is relatively isotropic, while once the structure is heated not only do we observe an increase in emittance, we also see a separation in the two planes of incidence due the anisotropy of the structure.

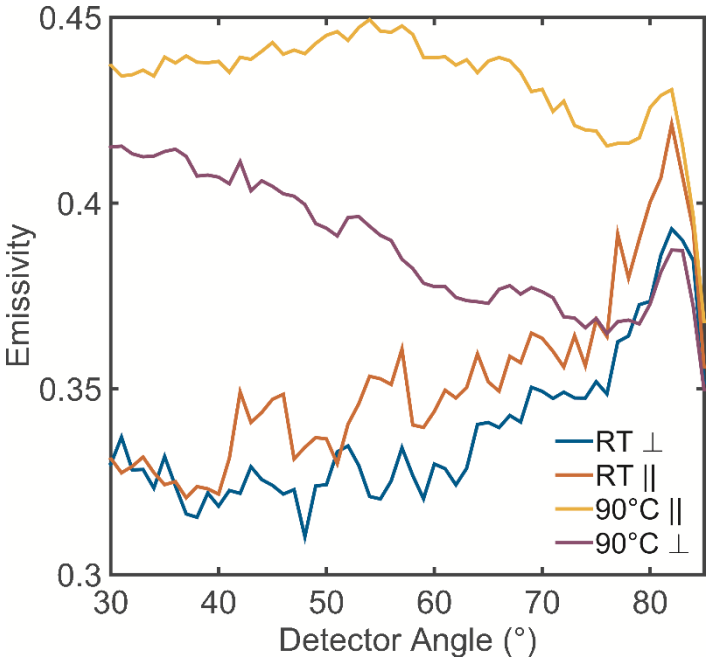

Figure 53: Angular dependent emissivity, showing the anisotropic response at high temperature of a typical 800 nm structured film.

This measurement technique is particularly useful for materials such as VO_2 with significant variation in emissivity across a range of temperature.

5.14 Summary

Refractory metal wire grid polarizers were produced by co-sputtering molybdenum and aluminium under specific conditions, which in conjunction with the removal of the aluminium through selective dissolution enabled the nanostructure array to transmit light. Basic thermal stability tests were conducted and the etched refractory metal nano-fins were stable in vacuum up to approximately 400°C with minor reversible effects. The refractory metal nano-fins were also stable up to 670°C, but beyond this permanent structural and polarization changes were noticeable until complete breakdown occurred around 1000°C.

The polarization spans 500 to 1100 nm and the extinction ratio significantly increases to >100. Possessing broadband polarization and sufficient extinction ratios, the new polarizing film has potential applications in coatings for sunglasses, windows, pyrometers, scientific instruments, and LCD panels.

In order to evaluate the flexibility of the system we produced VO_2 thin films and nanostructures which exhibit both positive and negative differential emission. Coatings which can increase their emissivity as temperature increases are of particular interest for radiatively cooled self-regulating

emitting surfaces. Formation of appropriately sized features in vanadium which can be oxidised to VO_2 opens up a new method for plasmonically controlling radiative transfer from a VO_2 surface.

Ruthenium and molybdenum nano-fins were produced and their electrochemical properties were compared in the form of capacitors. The electrochemical areal capacitance of the nano-fins were 22 times greater than their respective flat film electrodes. The electrochemical capacitances were 2.75 $mF/cm^2$and 2.16 mF/cm^2 for the ruthenium and molybdenum nano-fins respectively. However, when the capacitance per volume was compared, the molybdenum nano-fins demonstrated higher values at 21.66 F/cm^3 to the ruthenium at 20.77 F/cm^3.

6 Chapter 6 - Conclusion

This thesis presents how nanoporous metallic structures can be produced through chemical de-alloying. The precursor alloys were prepared by DC magnetron co-sputtering of aluminium and gold/refractory metal. The sponges may be divided into two types: those that are inert to oxidation and those that can oxidize. Nanoporous gold is the standout example of the first kind, whereas refractory metal sponges are examples of the second type.

The selected precursor alloy for gold sponges, $AuAl_2$ possesses a very distinct purple colour, easily recognisable and readily prepared, making it a suitable choice for *spongification*. The precursor alloy was also interesting for reasons other than sponge formation too: A high density of defects and Al vacancies were introduced when this material was deposited at room temperature. These were removed by annealing which caused a colour change to a deeper purple-pink. These optical changes were observed in ellipsometric experiments with a heated stage. Deposition of the alloy at high temperatures resulted in a much darker purple colour. This is due to the combination of two effects: the film was deposited with a lower defect density due to the higher temperature, and it acquired a very rough surface topography. The latter causes a darker colour due to the scattering of light from the surface roughness. X-ray diffraction results revealed that $AuAl_2$ was formed in both types of films, with additional peaks in the HT deposited thin films.

Consistent fabrication of high quality sponges involved careful timing and a keen eye. Often sponges would delaminate from the surface of the substrate due to over-etching. Composition and thickness were important parameters. A technique to conclusively determine optimal de-alloying times was developed. In this technique an optical model was created based on in situ transmittance measurements whilst de-alloying. Optical models for $AuAl_2$, nanoporous gold, glass and water were generated and fitted to the optical transmittance over time. Through this technique, the kinetics and mechanism of the de-alloying could be probed. Activation energies were found to be 46.5 ± 6.4 kJ/mol (0.48 ± 0.07 eV). The available evidence indicates that the rate is limited by movement of Al atoms and not by surface diffusion or movement of the Au atoms.

Further investigations into the optical properties of gold sponges uncovered differences between those produced in this project by de-alloying Au-Al precursors and the more ‘typical’ gold sponges produced by de-alloying a Au-Ag alloy. This was due to the ‘pinhole’ structure found in the present sponges that differs from the more interconnected pores and ligaments formed by other gold-reactive metal compositions. These sponges were optically characterized within a heating chamber on the ellipsometer. This investigation revealed that permanent coarsening of the gold sponges

made from precursors deposited at high temperatures began at temperatures as low as 50°C, although quite slowly. Higher temperatures significantly increased coarsening rates. As temperatures were increased so did the optical constants (*n* and *k*). However, the reverse effect occurs for the gold sponges made from precursors deposited at room temperature. Elevated temperatures caused significant and permanent coarsening.

Refractory metal alloys and sponges also were produced with diverse morphologies, with the sponges of Ta and W possessing morphologies similar to Au and Nb with a more web-like nanostructure. The concentration of NaOH needed was much greater for the refractory metal alloys as de-alloying times were much slower (due to slower diffusion rates of the refractory metals) and significant cracking also occurred. During the etching process, oxides were formed due to the concentration of the alkaline solution selected. The nanoporous refractory metals were visually similar to their oxide counterparts.

Although the refractory metal sponges were interesting, the morphology taken on by many of the precursor films was even more remarkable. This 'new' shape of nanostructure was dubbed 'nano-fins'. The 'nano-fin' coatings could be created by DC magnetron co-sputtering of several elements with aluminium. Due to the polarizing and refractory nature of the coatings, a concerted attempt was made to understand the growth regime of these fins. Substrate positioning is important as both metal fluxes must be received by the substrate to produce nano-fins. This was proved by depositing onto a surface on which grooves had been cut by laser: there was no growth of nano-fins deep within the lines which provides more evidence of the necessity of metal co-sputtering. The nano-fin microstructure could be produced with a wide range of elemental combinations of other refractory metals (W, Ta, Nb, V, Ru, Zr, Ti, Fe, Ni, Pt and Cr) with Al, with most possessing similar configurations. One exception is that Ru appears to have fins more closely packed together. Other combinations were looked into (Nb-Cu, Mo-Nb, no rotation Mo and Al), however these combinations did not produce any growth of nano-fins. Alteration of gas pressures were also investigated to observe changes that may affect the formation of nano-fins. Pressures slightly lower than normal (2.7 mTorr) caused scarce or no development of the nano-fins. As gas pressure was increased, the changes in morphology and growth were not very apparent, until the gas pressure was doubled to 5.5 mTorr. Morphological changes corresponded to optical changes with greater nano-fin formation denoted greater polarisation effects.

The polarizability of these nano-fin structures indicated potential optical applications for high temperature broadband polarizers. When annealed, the nano-fins were capable of withstanding temperatures of up to 670°C before slow oxidation with increasing temperatures, before complete

destruction at around 1000°C. The fins maintained their polarization effects with reflectance decreasing due to scattering of light caused by oxidation. With the removal of aluminium through selective dissolution, the thin films became transparent. Once de-alloyed the nano-fins become smaller and aggregated to become fairly aligned, similar to grid polarisers. The multiscale hierarchical structures possess polarization effects spanning from 500 to 1100 nm and extinction ratios >100. Thermal stability tests were conducted on these multiscale structures and they were shown to be stable in vacuum up to 400°C with reversible effects in the resistivity.

The ability to construct the nano-fins with different refractory metals means introduction of polarization effects and high surface area to a metal and its oxides. Such an oxide is VO_2 which possesses a transition from an insulator to a metal. Nano-fin VO_2 was discovered to produce an opposite effect to uniform flat film VO_2, whereby an increase in emissivity occurs passed the transition temperature of VO_2. This opposite effect has many implications into spectral selective coatings for passive cooling in an attempt to reduce energy costs.

The high surface area of the nano-fin coatings also indicated that they might have possible use in electrochemical capacitors. Ruthenium and its nano-fin counterpart possessed higher areal capacitance than molybdenum though the enhancement from uniform film to nano-fins was much greater for molybdenum (enhancement was 22 times from respective flat film to nano-fin). Areal capacitances were 2.75 $mF/cm^2$and 2.16 mF/cm^2 for the ruthenium and molybdenum nano-fins respectively. However, when the capacitance per volume was compared the molybdenum nano-fins demonstrated higher values at 21.66 F/cm^3 to the ruthenium at 20.77 F/cm^3. This suggests that ruthenium is a better metal for the production of electrochemical electrodes in NaCl solution, though with minimal increases at higher costs. It is also possible that these new structures would have gas sensing capabilities due to their high surface area.

In the future, further production of nano-fins with other metals (Mn, Co) might be worthwhile. An unanswered question is whether the second metal must be Al, or whether some other elements could also work. Exploration of other parameters that may affect nano-fin development, for example, high and low temperature deposition, stage height, slower rotation could be interesting. Further expansion of capacitor work utilising more metals such as Ta and oxidation of the fins to further increase the surface area of the nano-fins. Cross-section TEM and EDS/EELs would help determine the mechanism responsible for building the nano-fins.

7 Appendix

7.1 Refractive indices

7.1.1 Water

Wavelength (µm)	n	k
0.4000	1.3157	0.0000
0.4050	1.3152	0.0000
0.4100	1.3148	0.0000
0.4150	1.3144	0.0000
0.4200	1.3141	0.0000
0.4250	1.3137	0.0000
0.4300	1.3134	0.0000
0.4350	1.3130	0.0000
0.4400	1.3127	0.0000
0.4450	1.3124	0.0000
0.4500	1.3121	0.0000
0.4550	1.3118	0.0000
0.4600	1.3115	0.0000
0.4650	1.3112	0.0000
0.4700	1.3110	0.0000
0.4750	1.3107	0.0000
0.4800	1.3105	0.0000
0.4850	1.3102	0.0000
0.4900	1.3100	0.0000
0.4950	1.3098	0.0000
0.5000	1.3096	0.0000
0.5050	1.3093	0.0000
0.5100	1.3091	0.0000
0.5150	1.3089	0.0000
0.5200	1.3087	0.0000
0.5250	1.3085	0.0000
0.5300	1.3084	0.0000
0.5350	1.3082	0.0000
0.5400	1.3080	0.0000
0.5450	1.3078	0.0000
0.5500	1.3076	0.0000
0.5550	1.3075	0.0000
0.5600	1.3073	0.0000
0.5650	1.3072	0.0000
0.5700	1.3070	0.0000
0.5750	1.3069	0.0000
0.5800	1.3067	0.0000
0.5850	1.3066	0.0000
0.5900	1.3064	0.0000
0.5950	1.3063	0.0000
0.6000	1.3062	0.0000
0.6050	1.3060	0.0000
0.6100	1.3059	0.0000
0.6150	1.3058	0.0000
0.6200	1.3056	0.0000
0.6250	1.3055	0.0000
0.6300	1.3054	0.0000
0.6350	1.3053	0.0000
0.6400	1.3052	0.0000
0.6450	1.3050	0.0000
0.6500	1.3049	0.0000

0.6550	1.3048	0.0000	0.7300	1.3033	0.0000
0.6600	1.3047	0.0000	0.7350	1.3033	0.0000
0.6650	1.3046	0.0000	0.7400	1.3032	0.0000
0.6700	1.3045	0.0000	0.7450	1.3031	0.0000
0.6750	1.3044	0.0000	0.7500	1.3030	0.0000
0.6800	1.3043	0.0000	0.7550	1.3029	0.0000
0.6850	1.3042	0.0000	0.7600	1.3028	0.0000
0.6900	1.3041	0.0000	0.7650	1.3027	0.0000
0.6950	1.3040	0.0000	0.7700	1.3027	0.0000
0.7000	1.3039	0.0000	0.7750	1.3026	0.0000
0.7050	1.3038	0.0000	0.7800	1.3025	0.0000
0.7100	1.3037	0.0000	0.7850	1.3024	0.0000
0.7150	1.3036	0.0000	0.7900	1.3023	0.0000
0.7200	1.3035	0.0000	0.7950	1.3023	0.0000
0.7250	1.3034	0.0000	0.8000	1.3022	0.0000

Appendix 1 Table of optical constants (n and k) for water.

7.1.2 Glass substrate

Wavelength (µm)	n	k			
0.4000	1.5463	0.0000	0.4650	1.5361	0.0000
0.4050	1.5453	0.0000	0.4700	1.5355	0.0000
0.4100	1.5443	0.0000	0.4750	1.5349	0.0000
0.4150	1.5434	0.0000	0.4800	1.5344	0.0000
0.4200	1.5426	0.0000	0.4850	1.5338	0.0000
0.4250	1.5417	0.0000	0.4900	1.5333	0.0000
0.4300	1.5409	0.0000	0.4950	1.5328	0.0000
0.4350	1.5401	0.0000	0.5000	1.5323	0.0000
0.4400	1.5394	0.0000	0.5050	1.5319	0.0000
0.4450	1.5387	0.0000	0.5100	1.5314	0.0000
0.4500	1.5380	0.0000	0.5150	1.5310	0.0000
0.4550	1.5373	0.0000	0.5200	1.5306	0.0000
0.4600	1.5367	0.0000	0.5250	1.5301	0.0000
			0.5300	1.5297	0.0000

0.5350	1.5293	0.0000	0.6700	1.5220	0.0000
0.5400	1.5290	0.0000	0.6750	1.5218	0.0000
0.5450	1.5286	0.0000	0.6800	1.5216	0.0000
0.5500	1.5282	0.0000	0.6850	1.5214	0.0000
0.5550	1.5279	0.0000	0.6900	1.5212	0.0000
0.5600	1.5276	0.0000	0.6950	1.5210	0.0000
0.5650	1.5272	0.0000	0.7000	1.5208	0.0000
0.5700	1.5269	0.0000	0.7050	1.5207	0.0000
0.5750	1.5266	0.0000	0.7100	1.5205	0.0000
0.5800	1.5263	0.0000	0.7150	1.5203	0.0000
0.5850	1.5260	0.0000	0.7200	1.5202	0.0000
0.5900	1.5257	0.0000	0.7250	1.5200	0.0000
0.5950	1.5254	0.0000	0.7300	1.5199	0.0000
0.6000	1.5252	0.0000	0.7350	1.5197	0.0000
0.6050	1.5249	0.0000	0.7400	1.5195	0.0000
0.6100	1.5246	0.0000	0.7450	1.5194	0.0000
0.6150	1.5244	0.0000	0.7500	1.5193	0.0000
0.6200	1.5241	0.0000	0.7550	1.5191	0.0000
0.6250	1.5239	0.0000	0.7600	1.5190	0.0000
0.6300	1.5237	0.0000	0.7650	1.5188	0.0000
0.6350	1.5234	0.0000	0.7700	1.5187	0.0000
0.6400	1.5232	0.0000	0.7750	1.5186	0.0000
0.6450	1.5230	0.0000	0.7800	1.5184	0.0000
0.6500	1.5228	0.0000	0.7850	1.5183	0.0000
0.6550	1.5226	0.0000	0.7900	1.5182	0.0000
0.6600	1.5224	0.0000	0.7950	1.5180	0.0000
0.6650	1.5221	0.0000	0.8000	1.5179	0.0000

Appendix 2 Table of optical constants (n and k) for the glass substrate.

7.1.3 $AuAl_2$

Wavelength (µm)	n	k	0.4050	2.3048	2.9472
0.4000	2.2493	2.9705	0.4100	2.3568	2.9193

0.4150	2.4047	2.8872	0.5700	1.8954	2.2797
0.4200	2.4481	2.8511	0.5750	1.8616	2.3035
0.4250	2.4864	2.8118	0.5800	1.8290	2.3292
0.4300	2.5194	2.7698	0.5850	1.7978	2.3565
0.4350	2.5467	2.7256	0.5900	1.7679	2.3854
0.4400	2.5681	2.6800	0.5950	1.7393	2.4156
0.4450	2.5837	2.6337	0.6000	1.7122	2.4469
0.4500	2.5933	2.5873	0.6050	1.6864	2.4794
0.4550	2.5973	2.5414	0.6100	1.6620	2.5128
0.4600	2.5957	2.4967	0.6150	1.6390	2.5470
0.4650	2.5888	2.4536	0.6200	1.6172	2.5819
0.4700	2.5771	2.4127	0.6250	1.5967	2.6174
0.4750	2.5608	2.3743	0.6300	1.5775	2.6535
0.4800	2.5404	2.3388	0.6350	1.5594	2.6899
0.4850	2.5163	2.3065	0.6400	1.5425	2.7268
0.4900	2.4889	2.2775	0.6450	1.5267	2.7639
0.4950	2.4586	2.2521	0.6500	1.5119	2.8013
0.5000	2.4259	2.2302	0.6550	1.4982	2.8388
0.5050	2.3912	2.2121	0.6600	1.4854	2.8766
0.5100	2.3548	2.1976	0.6650	1.4736	2.9144
0.5150	2.3171	2.1867	0.6700	1.4627	2.9523
0.5200	2.2784	2.1795	0.6750	1.4526	2.9902
0.5250	2.2390	2.1758	0.6800	1.4433	3.0282
0.5300	2.1993	2.1755	0.6850	1.4348	3.0661
0.5350	2.1595	2.1786	0.6900	1.4270	3.1040
0.5400	2.1199	2.1847	0.6950	1.4200	3.1419
0.5450	2.0805	2.1940	0.7000	1.4136	3.1797
0.5500	2.0418	2.2060	0.7050	1.4079	3.2174
0.5550	2.0038	2.2208	0.7100	1.4028	3.2550
0.5600	1.9666	2.2381	0.7150	1.3983	3.2925
0.5650	1.9305	2.2578	0.7200	1.3944	3.3299

0.7250	1.3910	3.3672	0.7650	1.3819	3.6601
0.7300	1.3882	3.4044	0.7700	1.3827	3.6958
0.7350	1.3858	3.4414	0.7750	1.3839	3.7312
0.7400	1.3840	3.4783	0.7800	1.3853	3.7664
0.7450	1.3827	3.5150	0.7850	1.3870	3.8014
0.7500	1.3818	3.5516	0.7900	1.3889	3.8362
0.7550	1.3814	3.5879	0.7950	1.3911	3.8708
0.7600	1.3814	3.6241	0.8000	1.3935	3.9053

Appendix 3 Table of optical constants (n and k) for $AuAl_2$.

7.1.4 Nanoporous gold

Wavelength (μm)	n	k			
0.4000	1.4478	1.0310	0.5000	1.1240	1.1534
0.4050	1.4407	1.0313	0.5050	1.1024	1.1707
0.4100	1.4325	1.0317	0.5100	1.0809	1.1893
0.4150	1.4232	1.0322	0.5150	1.0597	1.2092
0.4200	1.4127	1.0330	0.5200	1.0388	1.2302
0.4250	1.4011	1.0341	0.5250	1.0184	1.2523
0.4300	1.3884	1.0357	0.5300	0.9986	1.2755
0.4350	1.3746	1.0379	0.5350	0.9793	1.2997
0.4400	1.3597	1.0407	0.5400	0.9608	1.3248
0.4450	1.3439	1.0442	0.5450	0.9429	1.3508
0.4500	1.3271	1.0486	0.5500	0.9258	1.3775
0.4550	1.3094	1.0540	0.5550	0.9095	1.4048
0.4600	1.2908	1.0603	0.5600	0.8940	1.4328
0.4650	1.2716	1.0677	0.5650	0.8793	1.4613
0.4700	1.2517	1.0762	0.5700	0.8655	1.4902
0.4750	1.2312	1.0860	0.5750	0.8524	1.5194
0.4800	1.2103	1.0969	0.5800	0.8402	1.5490
0.4850	1.1890	1.1091	0.5850	0.8287	1.5787
0.4900	1.1675	1.1226	0.5900	0.8180	1.6087
0.4950	1.1458	1.1373	0.5950	0.8080	1.6388
			0.6000	0.7987	1.6690

0.6050	0.7901	1.6992	0.7050	0.7183	2.2821
0.6100	0.7821	1.7294	0.7100	0.7181	2.3096
0.6150	0.7748	1.7596	0.7150	0.7180	2.3369
0.6200	0.7680	1.7898	0.7200	0.7181	2.3641
0.6250	0.7618	1.8199	0.7250	0.7185	2.3911
0.6300	0.7562	1.8499	0.7300	0.7189	2.4180
0.6350	0.7510	1.8797	0.7350	0.7196	2.4447
0.6400	0.7463	1.9095	0.7400	0.7204	2.4712
0.6450	0.7421	1.9391	0.7450	0.7213	2.4976
0.6500	0.7383	1.9686	0.7500	0.7224	2.5239
0.6550	0.7349	1.9979	0.7550	0.7236	2.5500
0.6600	0.7318	2.0271	0.7600	0.7249	2.5760
0.6650	0.7292	2.0561	0.7650	0.7264	2.6018
0.6700	0.7268	2.0849	0.7700	0.7279	2.6275
0.6750	0.7248	2.1136	0.7750	0.7296	2.6531
0.6800	0.7230	2.1421	0.7800	0.7313	2.6785
0.6850	0.7216	2.1705	0.7850	0.7332	2.7039
0.6900	0.7204	2.1986	0.7900	0.7351	2.7291
0.6950	0.7195	2.2266	0.7950	0.7372	2.7542
0.7000	0.7188	2.2544	0.8000	0.7393	2.7791

Appendix 4 Table of optical constants (n and k) for nanoporous gold.

7.2 SEM micrographs of attempted nano-fins

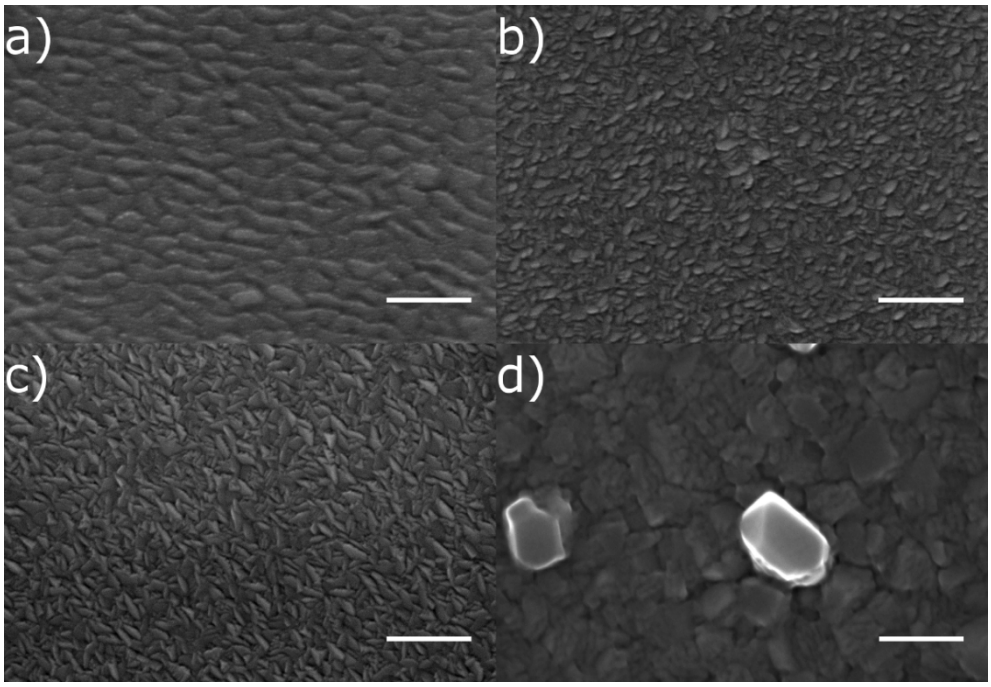

Appendix 5 SEM micrographs of co-sputtered a) Nb-Cu and c)Mo-Nb as well as deposited b) Mo and d) Al with no rotation. All scale bars are 200 nm.

7.3 Capacitance within the Mo-Al nano-fins

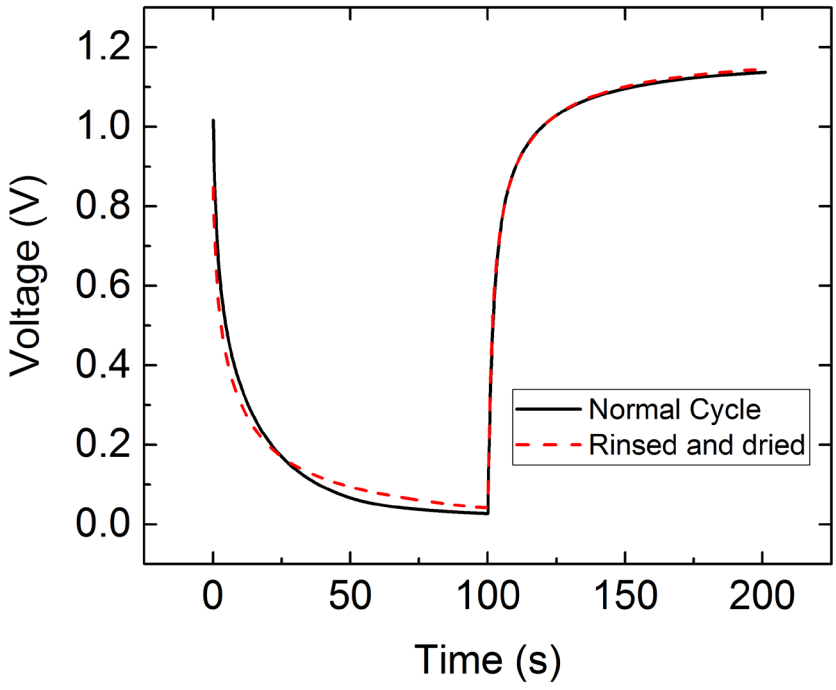

Appendix 6 Comparison of a normal voltage charge-discharge cycle and after the sample was rinsed and dried, still retaining charge.

7.4 Model fits to experimental data for Mo-Al nano-fins

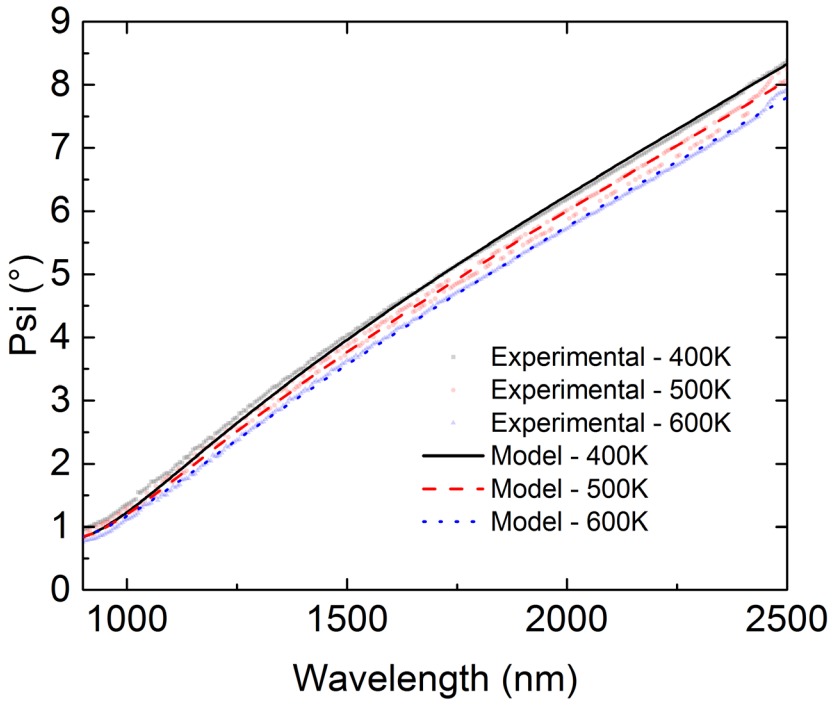

Appendix 7 Raw psi data obtained from heated ellipsometry, fit with optical model consisting of Gaussian-Drude oscillators.

7.5 s- and p- polarisation reflection data for Mo-Al nano-fins

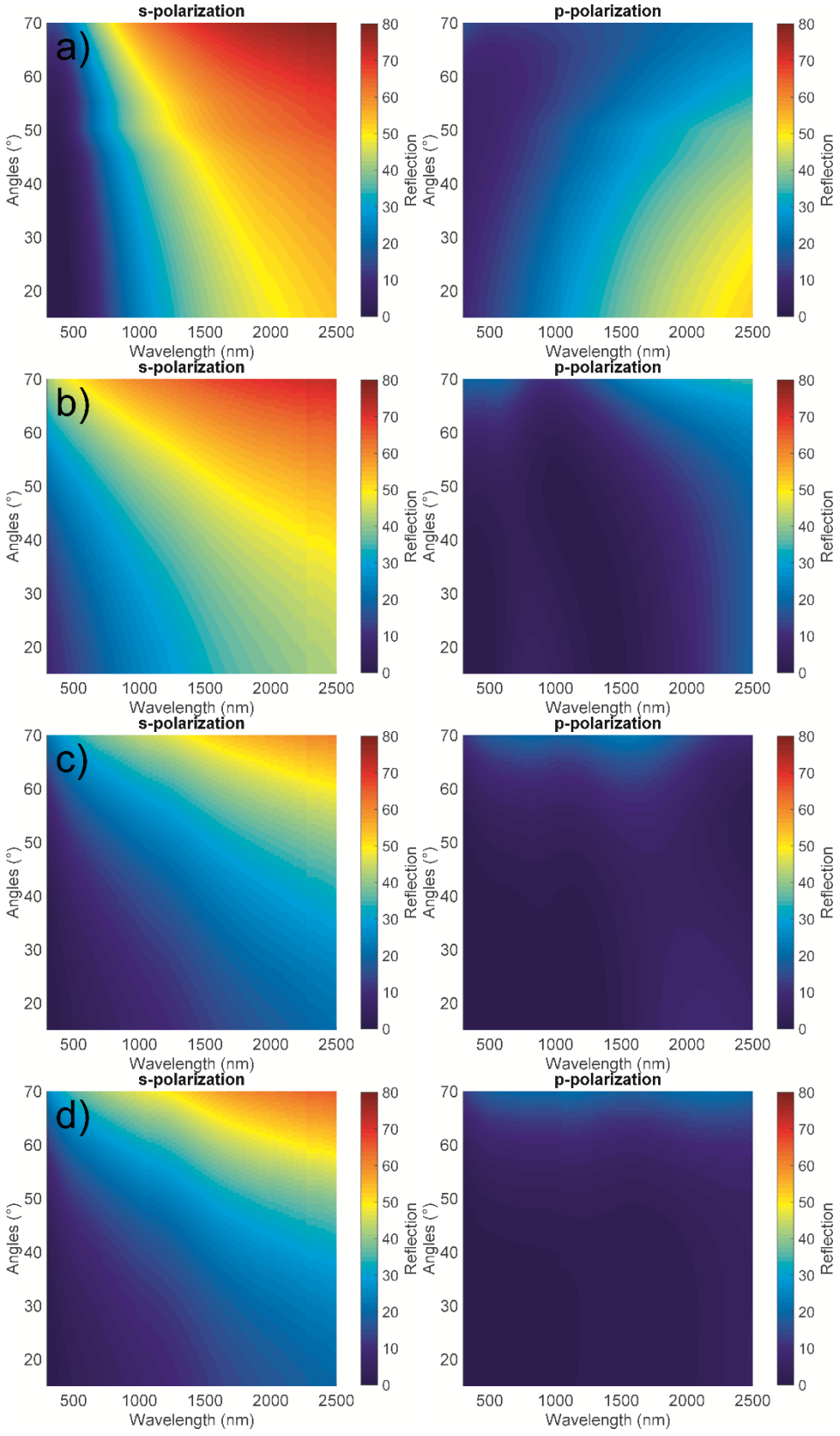

Appendix 8 s- and p- polarisation reflection data for fins at a) 15, b) 20, c) 30 and d) 40 minutes deposition time.

7.6 Model fits for hot and room temperature planar VO_2

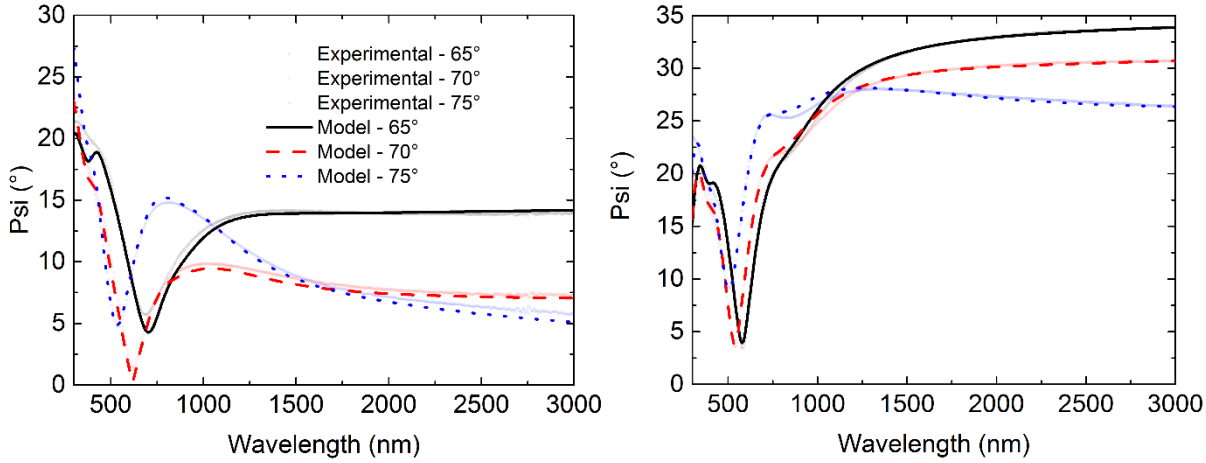

Appendix 9 Model fits for planar VO_2 at left: room temperature and right: after transition temperature.

7.7 Model fits for hot and room temperature nano-fin VO_2

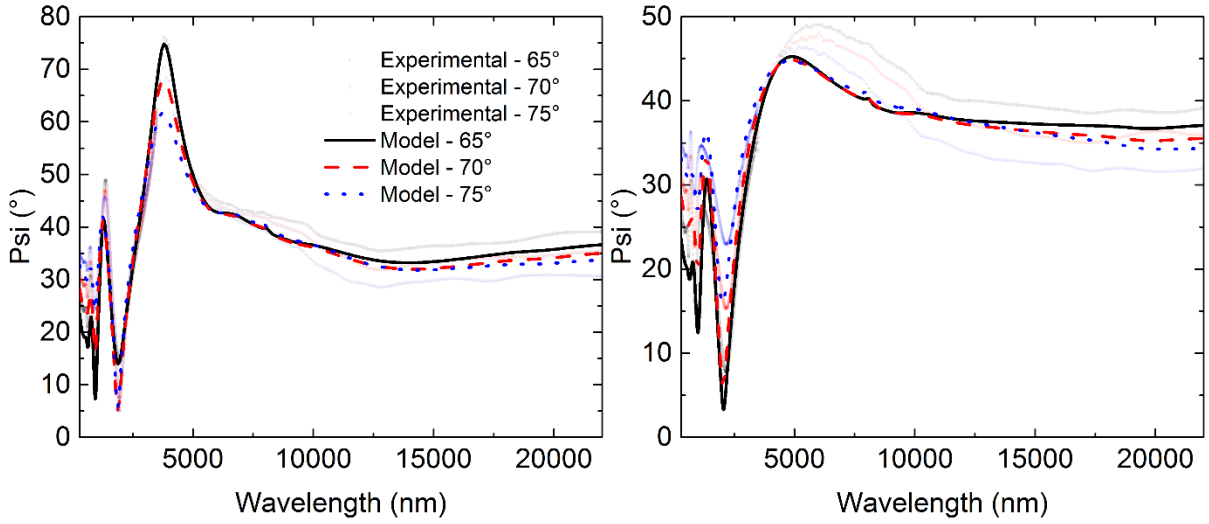

Appendix 10 Model fits for nano-fin VO_2 at left: room temperature and right: after transition temperature.

8 References

1 Tai, M. *et al.* Thermal Stability of Nanoporous Raney Gold Catalyst. *Metals* **5**, 1197-1211, doi:10.3390/met5031197 (2015).

2 Kraehnert, R. *et al.* Electrochemically dealloyed platinum with hierarchical pore structure as highly active catalytic coating. *Catal. Sci. Technol.* **5**, 206-216, doi:10.1039/C4CY00851K (2015).

3 Lang, X., Hirata, A., Fujita, T. & Chen, M. Nanoporous metal/oxide hybrid electrodes for electrochemical supercapacitors. *Nature nanotechnology* **6**, 232-236, doi:10.1038/nnano.2011.13 (2011).

4 Mortari, A., Maaroof, A., Martin, D. & Cortie, M. B. Mesoporous gold electrodes for sensors based on electrochemical double layer capacitance. *Sensors and Actuators B: Chemical* **123**, 262-268, doi:10.1016/j.snb.2006.08.018 (2007).

5 Glaner, L., der Lingen, E. & Cortie, M. B. Gold catalysts and methods for their preparation. *Australian Patent* **215039**, 30 (2003).

6 Yamazaki, T. *et al.* NO2 Gas Sensor Made of Porous MoO3 Sputtered Films. *Japanese Journal of Applied Physics* **44**, 792-795, doi:10.1143/JJAP.44.792 (2005).

7 Cortie, M. B., Maaroof, A., Smith, G. B. & Ngoepe, P. Nanoscale coatings of AuAlx and PtAlx and their mesoporous elemental derivatives. *Current Applied Physics* **6**, 440-443, doi:10.1016/j.cap.2005.11.036 (2006).

8 Maaroof, A. I., Cortie, M. B., Gentle, A. & Smith, G. B. Mesoporous gold sponge as a prototype 'metamaterial'. *Physica B: Condensed Matter* **394**, 167-170, doi:10.1016/j.physb.2006.12.014 (2007).

9 Supansomboon, S., Porkovich, A., Dowd, A., Arnold, M. D. & Cortie, M. B. Effect of Precursor Stoichiometry on the Morphology of Nanoporous Platinum Sponges. *ACS Applied Materials & Interfaces* **6**, 9411-9417, doi:10.1021/am501794y (2014).

10 El Mel, A.-A. *et al.* Unusual Dealloying Effect in Gold/Copper Alloy Thin Films: The Role of Defects and Column Boundaries in the Formation of Nanoporous Gold. *ACS Applied Materials & Interfaces* **7**, 2310-2321, doi:10.1021/am5065816 (2015).

11 Morrish, R., Dorame, K. & Muscat, a. J. Formation of nanoporous Au by dealloying AuCu thin films in HNO3. *Scripta Materialia* **64**, 856-859, doi:10.1016/j.scriptamat.2011.01.021 (2011).

12 Rizzi, P., Scaglione, F. & Battezzati, L. Nanoporous gold by dealloying of an amorphous precursor. *Journal of Alloys and Compounds* **586**, S117-S120, doi:10.1016/j.jallcom.2012.11.029 (2014).

13 Chen-Wiegart, Y. C. K., Wang, S., McNulty, I. & Dunand, D. C. Effect of Ag-Au composition and acid concentration on dealloying front velocity and cracking during nanoporous gold formation. *Acta Materialia* **61**, 5561-5570, doi:10.1016/j.actamat.2013.05.039 (2013).

14 Matsuno, H., Yokoyama, A., Watari, F., Uo, M. & Kawasaki, T. Biocompatibility and osteogenesis of refractory metal implants, titanium, hafnium, niobium, tantalum and rhenium. *Biomaterials* **22**, 1253-1262, doi:http://dx.doi.org/10.1016/S0142-9612(00)00275-1 (2001).

15 Gold, R. E. & Harrod, D. L. Refractory metal alloys for fusion reactor applications. *Journal of Nuclear Materials* **85–86, Part 2**, 805-815, doi:http://dx.doi.org/10.1016/0022-3115(79)90359-3 (1979).

16 Evans, D. A. (Google Patents, 1999).

17 Van Tong, P., Hoa, N. D., Van Duy, N. & Van Hieu, N. Micro-wheels composed of self-assembled tungsten oxide nanorods for highly sensitive detection of low level toxic chlorine gas. *RSC Advances* **5**, 25204-25207, doi:10.1039/C5RA00916B (2015).

18 Varghese, O. K. *et al.* Extreme Changes in the Electrical Resistance of Titania Nanotubes with Hydrogen Exposure. *Advanced Materials* **15**, 624-627, doi:10.1002/adma.200304586 (2003).

19 Yang, P., Zhao, D., Margolese, D. I., Chmelka, B. F. & Stucky, G. D. Generalized syntheses of large-pore mesoporous metal oxides with semicrystalline frameworks. *Nature* **396**, 152-155 (1998).

20 Ab Kadir, R. *et al.* Anodized nanoporous WO 3 Schottky contact structures for hydrogen and ethanol sensing. *J. Mater. Chem. A* **3**, 7994-8001, doi:10.1039/C4TA06286H (2015).

21 Kirchgeorg, R., Berger, S. & Schmuki, P. Ultra fast electrochromic switching of nanoporous tungsten–tantalum oxide films. *Chem. Commun.* **47**, 1000-1002, doi:10.1039/C0CC03201H (2011).

22 Minagar, S., Berndt, C. & Wen, C. Fabrication and Characterization of Nanoporous Niobia, and Nanotubular Tantala, Titania and Zirconia via Anodization. *Journal of Functional Biomaterials* **6**, 153-170, doi:10.3390/jfb6020153 (2015).

23 Ou, J. Z. *et al.* The anodized crystalline WO3 nanoporous network with enhanced electrochromic properties. *Nanoscale* **4**, 5980-5980, doi:10.1039/c2nr31203d (2012).

24 Erlebacher, J., Aziz, M. J., Karma, A., Dimitrov, N. & Sieradzki, K. Evolution of Nanoporosity in Dealloying. *Nature* **410**, 450-453, doi:10.1038/35068529 (2001).

25 Davis, M. E. Ordered porous materials for emerging applications. *Nature* **417**, 813-821, doi:10.1038/nature00785 (2002).

26 Masuda, H. & Fukuda, K. Ordered metal nanohole arrays made by a two-step replication of honeycomb structures of anodic alumina. *Science (New York, N.Y.)* **268**, 1466-1468, doi:10.1126/science.268.5216.1466 (1995).

27 Lu, X., Balk, T. J., Spolenak, R. & Arzt, E. Dealloying of Au-Ag thin films with a composition gradient: Influence on morphology of nanoporous Au. *Thin Solid Films* **515**, 7122-7126, doi:10.1016/j.tsf.2007.03.023 (2007).

28 Sardana, N., Birr, T., Schlenker, S., Reinhardt, C. & Schilling, J. Surface plasmons on ordered and bi-continuous spongy nanoporous gold. *New Journal of Physics* **16**, 063053-063053, doi:10.1088/1367-2630/16/6/063053 (2014).

29 Kucheyev, S. O. *et al.* Surface-enhanced Raman scattering on nanoporous Au. *Applied Physics Letters* **89**, 4-7, doi:10.1063/1.2260828 (2006).

30 Biener, J. *et al.* Nanoporous Plasmonic Metamaterials. *Advanced Materials* **20**, 1211-1217, doi:10.1002/adma.200701899 (2008).

31 Bryce C, T., Stephen A, S. & Luther, E. P. Nanoporous metal foams. *Angewandte Chemie - International Edition* **49**, 4544-4565, doi:10.1002/anie.200902994 (2010).

32 Hakamada, M. & Mabuchi, M. Processing of Nanoporous Gold by Dealloying and its Morphological Control. *Materials Science Forum* **561-565**, 1657-1660, doi:10.4028/www.scientific.net/MSF.561-565.1657 (2007).

33 Maaroof, A. I., Cortie, M. B. & Smith, G. B. Optical properties of mesoporous gold films. *Journal of Optics A: Pure and Applied Optics* **7**, 303-309, doi:10.1088/1464-4258/7/7/007 (2005).

34 San Marchi, C. & Mortensen, A. Deformation of open-cell aluminum foam. *Acta Materialia* **49**, 3959-3969, doi:10.1016/S1359-6454(01)00294-4 (2001).

35 Banhart, J. Properties and Applications of Cast Aluminum Sponges. *Advanced Engineering Materials* **2**, 188-191, doi:10.1002/(SICI)1527-2648(200004)2:4<188::AID-ADEM188>3.0.CO;2-G (2000).

36 Conde, Y. *et al.* Replication Processing of Highly Porous Materials. *Advanced Engineering Materials* **8**, 795-803, doi:10.1002/adem.200600077 (2006).

37 Ryan, G., Pandit, A. & Apatsidis, D. Fabrication methods of porous metals for use in orthopaedic applications. *Biomaterials* **27**, 2651-2670, doi:10.1016/j.biomaterials.2005.12.002 (2006).

38 Gauthier, M., Lefebvre, L. P., Thomas, Y. & Bureau, M. N. Production of metallic foams having open porosity using a powder metallurgy approach. *Materials and Manufacturing Processes* **19**, 793-811, doi:10.1081/Lmmp-20030539 (2004).

39 Oh, I. H., Nomura, N., Masahashi, N. & Hanada, S. Microstructures and mechanical properties of porous titanium compacts prepared by powder sintering. *Scripta Materialia* **49**, 1197-1202, doi:10.1016/j.scriptamat.2003.08.018 (2003).

40 Cai, A. *et al.* Direct formation of self-assembled nanoporous aluminium oxide on SiO 2 and Si substrates. **13**, 627-630 (2002).

41 Guzelaydin, A. H., Toparli, M. & Dikici, T. Formation and characterisation of nanoporous TiO2 layers on microroughened titanium surfaces by electrochemical anodisation. *Micro & Nano Letters* **9**, 144-148, doi:10.1049/mnl.2013.0719 (2014).

42 Qin, G. W. *et al.* A facile and template-free method to prepare mesoporous gold sponge and its pore size control. *Journal of Physical Chemistry C* **112**, 10352-10358, doi:10.1021/jp800923h (2008).

43 Gao, S. *et al.* Unique gold sponges: biopolymer-assisted hydrothermal synthesis and potential application as surface-enhanced Raman scattering substrates. *Nanotechnology* **16**, 2530-2535, doi:10.1088/0957-4484/16/11/012 (2005).

44 Cortie, M. B., Maaroof, A. I. & Smith, G. B. Electrochemical capacitance of mesoporous gold. *Gold Bulletin* **38**, 14-22, doi:10.1007/BF03215223 (2005).

45 Cortie, M. B., Maaroof, A. I., Stokes, N. & Mortari, A. Mesoporous gold sponge. *Australian Journal of Chemistry* **60**, 524-527, doi:10.1071/CH06372 (2007).

46 Xomeritakis, G. & Lin, Y. S. Fabrication of thin metallic membranes by MOCVD and sputtering. *Journal of Membrane Science* **133**, 217-230, doi:10.1016/S0376-7388(97)00084-7 (1997).

47 Jia, F., Yu, C., Deng, K. & Zhang, L. Nanoporous metal (Cu, Ag, Au) films with high surface area: General fabrication and preliminary electrochemical performance. *Journal of Physical Chemistry C* **111**, 8424-8431, doi:10.1021/jp071815y (2007).

48 Liu, L., Pippel, E., Scholz, R. & Gösele, U. Nanoporous Pt−Co Alloy Nanowires: Fabrication, Characterization, and Electrocatalytic Properties. *Nano Letters* **9**, 4352-4358, doi:10.1021/nl902619q (2009).

49 Kim, M.-S. & Nishikawa, H. Fabrication of nanoporous silver and microstructural change during dealloying of melt-spun Al–20 at.%Ag in hydrochloric acid. *Journal of Materials Science* **48**, 5645-5652, doi:10.1007/s10853-013-7360-3 (2013).

50 Wang, Y., Xu, J. L. & Wu, B. Electrochemical dealloying of Al2(Au,X) (X = Pt, Pd, PtPd, Ni, Co and NiCo) alloys in NaCl aqueous solution. *Physical chemistry chemical physics : PCCP* **15**, 5499-5509, doi:10.1039/c3cp44398a (2013).

51 Zhao, C., Qi, Z., Wang, X. & Zhang, Z. Fabrication and characterization of monolithic nanoporous copper through chemical dealloying of Mg-Cu alloys. *Corrosion Science* **51**, 2120-2125, doi:10.1016/j.corsci.2009.05.043 (2009).

52 Pugh, D. V., Dursun, A. & Corcoran, S. G. Formation of nanoporous platinum by selective dissolution of Cu from Cu0.75Pt0.25. *Journal of Materials Research* **18**, 216-221, doi:10.1557/JMR.2003.0030 (2003).

53 Hanarp, P., Käll, M. & Sutherland, D. S. Optical Properties of Short Range Ordered Arrays of Nanometer Gold Disks Prepared by Colloidal Lithography. *The Journal of Physical Chemistry B* **107**, 5768-5772, doi:10.1021/jp027562k (2003).

54 Hanarp, P., Sutherland, D. S., Gold, J. & Kasemo, B. Control of nanoparticle film structure for colloidal lithography. *Colloids and Surfaces A: Physicochemical and Engineering Aspects* **214**, 23-36, doi:10.1016/S0927-7757(02)00367-9 (2003).

55 Jansen, H., Boer, M. D., Legtenberg, R. & Elwenspoek, M. The black silicon method: a universal method for determining the parameter setting of a fluorine-based reactive ion etcher in deep silicon trench etching with profile control. *Journal of Micromechanics and Microengineering* **5**, 115-120, doi:10.1088/0960-1317/5/2/015 (1995).

56 Snyder, J., Asanithi, P., Dalton, A. B. & Erlebacher, J. Stabilized Nanoporous Metals by Dealloying Ternary Alloy Precursors. *Advanced Materials* **20**, 4883-4886, doi:10.1002/adma.200702760 (2008).

57 Erlebacher, J. An Atomistic Description of Dealloying. *Journal of The Electrochemical Society* **151**, C614, doi:10.1149/1.1784820 (2004).

58 Galinski, H. *et al.* Dealloying of platinum-aluminum thin Films: Dynamics of pattern formation. *Physical Review Letters* **107**, 6-9, doi:10.1103/PhysRevLett.107.225503 (2011).

59 Qian, L. H. & Chen, M. W. Ultrafine nanoporous gold by low-temperature dealloying and kinetics of nanopore formation. *Applied Physics Letters* **91**, 89-92, doi:10.1063/1.2773757 (2007).

60 Zhang, Z. *et al.* Fabrication and characterization of nanoporous gold composites through chemical dealloying of two phase Al–Au alloys. *Journal of Materials Chemistry* **19**, 6042-6050, doi:10.1039/B904052H (2009).

61 Sieradzki, K. *et al.* The Dealloying Critical Potential. *Journal of The Electrochemical Society* **149**, B370, doi:10.1149/1.1492288 (2002).

62 Atkins, P. W. *Physical Chemistry*. 6th edn, (W.H. Freeman and Company, 1997).

63 Lide, D. R. *Handbook of Chemistry & Physics*. 87th edn, (CRC, 2006).

64 Haynes, W. M. *CRC Handbook of Chemistry and Physics*. 93rd edn, (Taylor & Francis, 2012).

65 Aylward, G. H. & Findlay, T. J. V. *SI Chemical Data*. 6th edn, (John Wiley and Sons, 2008).

66 Bard, A. J., Parsons, R. & Jordan, J. *Standard Potentials in Aqueous Solution*. (Marcel Dekker, 1985).

67 Milazzo, G., Caroli, S. & Sharma, V. K. *Tables of Standard Electrode Potentials*. (Wiley, 1978).

68 Swift, E. H. & Butler, E. A. *Quantitative Measurements and Chemical Equilibria*. (Freeman, 1972).

69 *Electrode Potential and Galvanic Corrosion*, <https://www.engineeringtoolbox.com/electrode-potential-d_482.html> (2003).

70 Weissmüller, J., Newman, R. C., Jin, H.-J., Hodge, A. M. & Kysar, J. W. Nanoporous Metals by Alloy Corrosion: Formation and Mechanical Properties. *MRS Bulletin* **34**, 577-586, doi:10.1557/mrs2009.157 (2009).

71 Qian, L. H., Yan, X. Q., Fujita, T., Inoue, a. & Chen, M. W. Surface enhanced Raman scattering of nanoporous gold: Smaller pore sizes stronger enhancements. *Applied Physics Letters* **90**, 1-4, doi:10.1063/1.2722199 (2007).

72 Chen, H. A., Long, J. L., Lin, Y. H., Weng, C. J. & Lin, H. N. Plasmonic properties of a nanoporous gold film investigated by far-field and near-field optical techniques. *Journal of Applied Physics* **110**, 6-11, doi:10.1063/1.3631824 (2011).

73 Maaroof, A. I., Gentle, A., Smith, G. B. & Cortie, M. B. Bulk and surface plasmons in highly nanoporous gold films. *Journal of Physics D: Applied Physics* **40**, 5675-5682, doi:10.1088/0022-3727/40/18/024 (2007).

74 Maaroof, A. I., Gentle, A. R., Cortie, M. B. & Smith, G. B. Nanoporous plasmonic coatings. (2007).

75 Hoa, N. D., Duy, N. V., El-safty, S. A. & Hieu, N. V. Meso- / Nanoporous Semiconducting Metal Oxides for Gas Sensor Applications. *Journal of Nanomaterials* **2015** (2015).

76 Hyodo, T., Shibata, H., Shimizu, Y. & Egashira, M. H2 sensing properties of diode-type gas sensors fabricated with Ti- and/or Nb-based materials. *Sensors and Actuators, B: Chemical* **142**, 97-104, doi:10.1016/j.snb.2009.07.058 (2009).

77 Ruffato, G., Romanato, F., Garoli, D. & Cattarin, S. Nanoporous gold plasmonic structures for sensing applications. *Opt. Express* **19**, 13164-13170, doi:10.1364/OE.19.013164 (2011).

78 Wang, Y. *et al.* Mesoporous Transition Metal Oxides for Supercapacitors. *Nanomaterials* **5**, 1667-1689, doi:10.3390/nano5041667 (2015).

79 Lv, Q. *et al.* Ultrafast charge/discharge solid-state thin-film supercapacitors via regulating the microstructure of transition-metal-oxide. *Journal of Materials Chemistry A* **5**, 2759-2767, doi:10.1039/C6TA09849E (2017).

80 Zhang, J. & Li, C. M. Nanoporous metals: fabrication strategies and advanced electrochemical applications in catalysis, sensing and energy systems. *Chemical Society Reviews* **41**, 7016-7031, doi:10.1039/C2CS35210A (2012).

81 Mandapati, J. & Balasubramanian, K. *Simple Capacitors to Supercapacitors-An Overview*. Vol. 3 (2008).

82 Tai, M. C., Gentle, A., Arnold, M. D. & Cortie, M. B. Optical in situ study of de-alloying kinetics in nanoporous gold sponges. *RSC Advances* **6**, 85773-85778, doi:10.1039/C6RA18272K (2016).

83 Supansomboon, S., Maaroof, A. I. & Cortie, M. B. "Purple glory": The optical properties and technology of AuAl2 coatings. *Gold Bulletin* **41**, 296-304, doi:10.1007/BF03214887 (2008).

84 Philipp, H. R. AuAl2: Optical Properties and Consideration as a Transparent Electrode Material. *Physica Status Solidi (a)* **547**, 547-551 (1982).

85 Chen, L. Y. & Lynch, D. W. The Optical Properties of AuAl2 and PtAl2. *Physica Status Solidi (B)* **387** (1988).

86 Keast, V. J., Birt, K., Koch, C. T., Supansomboon, S. & Cortie, M. B. The role of plasmons and interband transitions in the color of AuAl 2, AuIn2, and AuGa2. *Applied Physics Letters* **99**, 97--100, doi:10.1063/1.3638061 (2011).

87 Keast, V. J., Zwan, B., Supansomboon, S., Cortie, M. B. & Persson, P. O. AuAl2 and PtAl2 as potential plasmonic materials. *Journal of Alloys and Compounds* **577**, 581--586, doi:10.1016/j.jallcom.2013.06.161 (2013).

88 Cahn, R. W. Materials science: A precious stone that isn't. *Nature* **396**, 523--524, doi:10.1038/25010 (1998).

89 Moser, M., Mayrhofer, P. H., Ross, I. M. & Rainforth, W. M. Microstructure and mechanical properties of sputtered intermetallic Al–Au coatings. *Journal of Applied Physics* **102**, 023523-023523, doi:10.1063/1.2761844 (2007).

90 Furrer, A., Seita, M. & Spolenak, R. The effects of defects in purple AuAl2 thin films. *Acta Materialia* **61**, 2874-2883, doi:10.1016/j.actamat.2013.01.029 (2013).

91 Keast, V. J. *et al.* The effect of vacancies on the optical properties of AuAl 2. *Journal of Physics: Condensed Matter* **27**, 505501-505501, doi:10.1088/0953-8984/27/50/505501 (2015).

92 Furrer, A. & Spolenak, R. Colors of thin films of binary and ternary gold- and platinum-based alloys. *Acta Materialia* **66**, 241-250, doi:10.1016/j.actamat.2013.11.056 (2014).

93 Mitterer, C., Lenhart, H., Mayrhofer, P. H. & Kathrein, M. Sputter-deposited Al-Au coatings. *Intermetallics* **12**, 579-587, doi:10.1016/j.intermet.2004.02.003 (2004).

94 Parida, S. *et al.* Volume change during the formation of nanoporous gold by dealloying. *Physical Review Letters* **97**, 4-7, doi:10.1103/PhysRevLett.97.035504 (2006).

95 Senior, N. a. & Newman, R. C. Synthesis of tough nanoporous metals by controlled electrolytic dealloying. *Nanotechnology* **17**, 2311-2316, doi:10.1088/0957-4484/17/9/040 (2006).

96 Sun, Y. & Balk, T. J. A multi-step dealloying method to produce nanoporous gold with no volume change and minimal cracking. *Scripta Materialia* **58**, 727-730, doi:10.1016/j.scriptamat.2007.12.008 (2008).

97 Sun, Y., Kucera, K. P., Burger, S. a. & John Balk, T. Microstructure, stability and thermomechanical behavior of crack-free thin films of nanoporous gold. *Scripta Materialia* **58**, 1018-1021, doi:10.1016/j.scriptamat.2008.01.036 (2008).

98 Bosman, M., Anstis, G. R., Keast, V. J., Clarke, J. D. & Cortie, M. B. Light splitting in nanoporous gold and silver. *ACS Nano* **6**, 319-326, doi:10.1021/nn203600n (2012).

99 Yu, F. *et al.* Simultaneous excitation of propagating and localized surface plasmon resonance in nanoporous gold membranes. *Analytical Chemistry* **78**, 7346-7350, doi:10.1021/ac060829h (2006).

100 Smith, G. B., Maaroof, A. I. & Gentle, A. Homogenized Lorentz–Drude optical response in highly nanoporous conducting gold layers produced by de-alloying. *Optics Communications* **271**, 263-268, doi:10.1016/j.optcom.2006.10.038 (2007).

101 Chen, a. Y. *et al.* Pore-size tuning and optical performances of nanoporous gold films. *Microporous and Mesoporous Materials* **202**, 50-56, doi:10.1016/j.micromeso.2014.09.048 (2015).

102 Detsi, E., Salverda, M., Onck, P. R. & De Hosson, J. T. M. On the localized surface plasmon resonance modes in nanoporous gold films. *Journal of Applied Physics* **115**, 044308-044308, doi:10.1063/1.4862440 (2014).

103 Zhang, L. *et al.* Effect of residual silver on surface-enhanced raman scattering of dealloyed nanoporous gold. *Journal of Physical Chemistry C* **115**, 19583-19587, doi:10.1021/jp205892n (2011).

104 Qian, L. H., Inoue, a. & Chen, M. W. Large surface enhanced Raman scattering enhancements from fracture surfaces of nanoporous gold. *Applied Physics Letters* **92**, 2006-2009, doi:10.1063/1.2890164 (2008).

105 Lang, X. Y., Chen, L. Y., Guan, P. F., Fujita, T. & Chen, M. W. Geometric effect on surface enhanced Raman scattering of nanoporous gold: Improving Raman scattering by tailoring

ligament and nanopore ratios. *Applied Physics Letters* **94**, 10-13, doi:10.1063/1.3143628 (2009).

106 Lang, X. Y., Guan, P., Zhang, L., Fujita, T. & Chen, M. W. Characteristic Length and Temperature Dependence of Surface Enhanced Raman Scattering of Nanoporous Gold. *The Journal of Physical Chemistry C* **113**, 10956-10961, doi:10.1021/jp903137n (2009).

107 Yamazaki, M. *et al.* Non-emissive colour filters for fluorescence detection. *Lab on a chip* **11**, 1228-1233, doi:10.1039/c0lc00642d (2011).

108 Yan, X. *et al.* Electrically conductive thin-film color filters made of single-material indium-tin-oxide. *Journal of Applied Physics* **109**, 1-5, doi:10.1063/1.3592222 (2011).

109 Antczak, G. & Ehrlich, G. Surface Diffusion: Metals, Metal Atoms, and Clusters. 784, doi:10.1017/CBO9780511730320 (2010).

110 Streicher, M. A. The Dissolution of Aluminum in Sodium Hydroxide Solutions. *Journal of The Electrochemical Society* **93**, 285, doi:10.1149/1.2773816 (1948).

111 Robin, A. Corrosion behaviour of tantalum in sodium hydroxide solutions. *Journal of Applied Electrochemistry* **33**, 37-42, doi:10.1023/A:1022982320438 (2003).

112 Heumann, T. & Stolica, N. The electrochemical behaviour of tungsten—II. The dissolution of tungsten in NaOH solutions. *Electrochimica Acta* **16**, 1635-1646, doi:https://doi.org/10.1016/0013-4686(71)85074-0 (1971).

113 Gad Allah, A. G. Nature and corrodability of thin oxide films formed on niobium in NaOH solutions. *Journal of Applied Electrochemistry* **21**, 346-350, doi:10.1007/bf01020220 (1991).

114 Tai, M. C., Gentle, A. R., Arnold, M. D. & Cortie, M. B. Spontaneous growth of polarizing refractory metal 'nano-fins'. *Nanotechnology* **29**, 105702 (2018).

115 Carver, G. E. Chemically vapor deposited molybdenum films of high infrared reflectance. *Thin Solid Films* **63**, 169-174, doi:10.1016/0040-6090(79)90121-4 (1979).

116 Agnihotri, O. P., Gupta, B. K., Agarwal, A. K. & Bhatnagar, V. P. Solar selective black molybdenum coatings by chemical conversion. *Thin Solid Films* **109**, 193-200, doi:10.1016/0040-6090(83)90108-6 (1983).

117 Chain, E. E., Gesheva, K. A. & Seraphin, B. O. Chemically vapor-deposited black molybdenum films of high IR reflectance and significant solar absorptance. *Thin Solid Films* **83**, 387-392, doi:10.1016/0040-6090(81)90645-3 (1981).

118 Weber, T., Käsebier, T., Helgert, M., Kley, E.-B. & Tünnermann, A. Tungsten wire grid polarizer for applications in the DUV spectral range. *Appl. Opt.* **51**, 3224-3227, doi:10.1364/AO.51.003224 (2012).

119 Weber, T., Käsebier, T., Kley, E.-B. & Tünnermann, A. Broadband iridium wire grid polarizer for UV applications. *Opt. Lett.* **36**, 445-447, doi:10.1364/OL.36.000445 (2011).

120 Liu, J., Cankurtaran, B., Wieczorek, L., Ford, M. J. & Cortie, M. Anisotropic Optical Properties of Semitransparent Coatings of Gold Nanocaps. *Advanced Functional Materials* **16**, 1457-1461, doi:10.1002/adfm.200500794 (2006).

121 Robbie, K., Friedrich, L. J., Dew, S. K., Smy, T. & Brett, M. J. Fabrication of thin films with highly porous microstructures. *Journal of Vacuum Science & Technology A: Vacuum, Surfaces, and Films* **13**, 1032-1035, doi:10.1116/1.579579 (1995).

122 Taschuk, M. T., Hawkeye, M. M. & Brett, M. J. Glancing angle deposition. *Handbook of Deposition Technologies for Films and Coatings*, 621-678 (2010).

123 Robbie, K. & Brett, M. J. Sculptured thin films and glancing angle deposition: Growth mechanics and applications. *Journal of Vacuum Science & Technology A: Vacuum, Surfaces, and Films* **15**, 1460-1465, doi:10.1116/1.580562 (1997).

124 Robbie, K. *et al.* Ultrahigh vacuum glancing angle deposition system for thin films with controlled three-dimensional nanoscale structure. *Review of Scientific Instruments* **75**, 1089-1097, doi:10.1063/1.1667254 (2004).

125 He, Y. & Zhao, Y. Advanced multi-component nanostructures designed by dynamic shadowing growth. *Nanoscale* **3**, 2361-2375, doi:10.1039/C1NR10103J (2011).

126 Robbie, K., Sit, J. C. & Brett, M. J. Advanced techniques for glancing angle deposition. *Journal of Vacuum Science & Technology B: Microelectronics and Nanometer Structures Processing, Measurement, and Phenomena* **16**, 1115-1122, doi:10.1116/1.590019 (1998).

127 Hodgkinson, I., Wu, Q. H., De Silva, L. & Arnold, M. Inorganic positive uniaxial films fabricated by serial bideposition. *Opt. Express* **12**, 3840-3847, doi:10.1364/OPEX.12.003840 (2004).

128 Hodgkinson, I. & Wu, Q. H. Serial bideposition of anisotropic thin films with enhanced linear birefringence. *Appl. Opt.* **38**, 3621-3625, doi:10.1364/AO.38.003621 (1999).

129 Beydaghyan, G., Kaminska, K., Brown, T. & Robbie, K. Enhanced birefringence in vacuum evaporated silicon thin films. *Appl. Opt.* **43**, 5343-5349, doi:10.1364/AO.43.005343 (2004).

130 Wu, Q. H., Silva, L. D., Arnold, M., Hodgkinson, I. J. & Takeuchi, E. All-silicon polarizing filters for near-infrared wavelengths. *Journal of Applied Physics* **95**, 402-404, doi:10.1063/1.1627481 (2004).

131 Hodgkinson, I., De Silva, L. & Arnold, M. in *Optics & Photonics 2005.* 587001-587001-587015 (International Society for Optics and Photonics).

132 Jensen, M. O. & Brett, M. J. Porosity engineering in glancing angle deposition thin films. *Applied Physics A* **80**, 763-768, doi:10.1007/s00339-004-2878-5 (2004).

133 Brett, M. J. & Hawkeye, M. M. Materials science. New materials at a glance. *Science (New York, N.Y.)* **319**, 1192-1193, doi:10.1126/science.1153910 (2008).

134 Arnold, M. D., Hodgkinson, I. J., Wu, Q. H. & Blaikie, R. J. Multi-axis retarder arrays by masked oblique deposition. *Journal of Vacuum Science & Technology B: Microelectronics and Nanometer Structures Processing, Measurement, and Phenomena* **23**, 1398-1404, doi:10.1116/1.1993618 (2005).

135 Km, A. S., Yong Jun, P. & Chang Kwon, H. Influence of deposition angle on the properties of ZrO$_2$ thin films fabricated by oblique angle deposition. *Journal of the Korean Physical Society* **56**, 1282-1282, doi:10.3938/jkps.56.1282 (2010).

136 Kranenburg, H. v. & Lodder, C. Tailoring growth and local composition by oblique-incidence deposition: a review and new experimental data. *Materials Science and Engineering: R: …*, 295-354 (1994).

137 Abel, P. R., Lin, Y.-M., Celio, H., Heller, A. & Mullins, C. B. Improving the Stability of Nanostructured Silicon Thin Film Lithium-Ion Battery Anodes through Their Controlled Oxidation. *ACS Nano* **6**, 2506-2516, doi:10.1021/nn204896n (2012).

138 Merkel, J. J., Sontheimer, T., Rech, B. & Becker, C. Directional growth and crystallization of silicon thin films prepared by electron-beam evaporation on oblique and textured surfaces. *Journal of Crystal Growth* **367**, 126-130, doi:10.1016/j.jcrysgro.2012.12.037 (2013).

139 Jensen, M. O. & Brett, M. J. Square spiral 3D photonic bandgap crystals at telecommunications frequencies. *Opt. Express* **13**, 3348-3354, doi:10.1364/OPEX.13.003348 (2005).

140 Savaloni, H., Haydari-Nasab, F. & Malmir, M. Nanostructure and Optical Properties of Silver Helical Pentagon Nanosculptured Thin Films. *Advances in Condensed …* **2014** (2014).

141 Pursel, S. M. & Horn, M. W. Prospects for nanowire sculptured-thin-film devices. *Journal of Vacuum Science & Technology B: Microelectronics and Nanometer Structures* **25**, 2611-2611, doi:10.1116/1.2787749 (2007).

142 He, Y., Fu, J. & Zhao, Y. Oblique angle deposition and its applications in plasmonics. *Frontiers of Physics* **9**, 47-59, doi:10.1007/s11467-013-0357-1 (2014).

143 Hawkeye, M. M. & Brett, M. J. Glancing angle deposition: Fabrication, properties, and applications of micro- and nanostructured thin films. *Journal of Vacuum Science & Technology A: Vacuum, Surfaces, and Films* **25**, 1317-1317, doi:10.1116/1.2764082 (2007).

144 Walsby, E. D., Arnold, M., Wu, Q. h., Hodgkinson, I. J. & Blaikie, R. J. Growth and characterisation of birefringent films on textured silicon substrates. *Microelectronic Engineering* **78–79**, 436-441, doi:https://doi.org/10.1016/j.mee.2004.12.055 (2005).

145 Vick, D. *et al.* Self-shadowing and surface diffusion effects in obliquely deposited thin films. *Thin Solid Films* **339**, 88-94, doi:https://doi.org/10.1016/S0040-6090(98)01154-7 (1999).

146 Chen, L., Lu, T. M. & Wang, G. C. Biaxially textured Mo films with diverse morphologies by substrate-flipping rotation. *Nanotechnology* **22**, 505701 (2011).

147 Dick, B., Brett, M. J. & Smy, T. Controlled growth of periodic pillars by glancing angle deposition. *Journal of Vacuum Science & Technology B: Microelectronics and Nanometer Structures Processing, Measurement, and Phenomena* **21**, 23-28, doi:10.1116/1.1529652 (2003).

148 El Beainou, R. *et al.* Correlation between structure and electrical resistivity of W-Cu thin films prepared by GLAD co-sputtering. *Surface and Coatings Technology* **313**, 1-7, doi:https://doi.org/10.1016/j.surfcoat.2017.01.039 (2017).

149 Yahya, M. *et al.* Nanostructured Ti–Ta thin films synthesized by combinatorial glancing angle sputter deposition. *Nanotechnology* **27**, 495604 (2016).

150 Chinmay, K., Aliaksandr, S., Pio John, S. B. & Alfred, L. Synthesis of WO 3 nanoblades by the dealloying of glancing angle deposited W-Fe nanocolumnar thin films. *Nanotechnology* **25**, 205606 (2014).

151 Brown, T. & Robbie, K. Observations of self-assembled microscale triangular-shaped spikes in copper and silver thin films. *Thin Solid Films* **531**, 103-112, doi:http://dx.doi.org/10.1016/j.tsf.2012.12.118 (2013).

152 Siad, A., Besnard, A., Nouveau, C. & Jacquet, P. Critical angles in DC magnetron glad thin films. *Vacuum* **131**, 305-311, doi:10.1016/j.vacuum.2016.07.012 (2016).

153 Saraiva, M. & Depla, D. Texture and microstructure in co-sputtered Mg-M-O (M = Mg, Al, Cr, Ti, Zr, and Y) films. *Journal of Applied Physics* **111**, 104903, doi:10.1063/1.4718431 (2012).

154 Radnóczi, G. Z., Seppänen, T., Pécz, B., Hultman, L. & Birch, J. Growth of highly curved Al1-xInxN nanocrystals. *physica status solidi (a)* **202**, R76-R78, doi:10.1002/pssa.200510024 (2005).

155 Lamas, J. S., Leroy, W. P. & Depla, D. Influence of the target–substrate distance on the growth of YSZ thin films. *Surface and Coatings Technology* **241**, 26-29, doi:10.1016/j.surfcoat.2013.10.018 (2014).

156 Lamas, J. S. *et al.* Using the macroscopic scale to predict the nano-scale behavior of YSZ thin films. *Surface and Coatings Technology* **238**, 45-50, doi:10.1016/j.surfcoat.2013.10.034 (2014).

157 Alvarez, R. *et al.* Growth regimes of porous gold thin films deposited by magnetron sputtering at oblique incidence: from compact to columnar microstructures. *Nanotechnology* **24**, 045604 (2013).

158 Gentle, A. *et al.* in *New Concepts in Solar and Thermal Radiation Conversion and Reliability.* 107590L (International Society for Optics and Photonics).

159 Balakrishnan, A. & Subramanian, K. R. V. *Nanostructured Ceramic Oxides for Supercapacitor Applications*. (CRC Press, 2014).

160 Zhang, C. Super pseudocapacitors. *Nature Energy* **3**, 1019-1019, doi:10.1038/s41560-018-0301-2 (2018).

161 Chen, L. Y. *et al.* Toward the Theoretical Capacitance of RuO2 Reinforced by Highly Conductive Nanoporous Gold. *Advanced Energy Materials* **3**, 851-856, doi:10.1002/aenm.201300024 (2013).

162 Liu, K.-y., Zhang, Y., Zhang, W., Zheng, H. & Su, G. Charge-discharge process of MnO2 supercapacitor. *Transactions of Nonferrous Metals Society of China* **17**, 649-653, doi:https://doi.org/10.1016/S1003-6326(07)60150-2 (2007).

163 Du, H. *et al.* Pseudocapacitance of nanoporous Ni@NiO nanoparticles on Ni foam substrate: Influence of the annealing temperature. *International Journal of Hydrogen Energy* **42**, 15236-15245, doi:https://doi.org/10.1016/j.ijhydene.2017.04.109 (2017).

164 Xiong, S., Yuan, C., Zhang, X., Xi, B. & Qian, Y. Controllable Synthesis of Mesoporous Co3O4 Nanostructures with Tunable Morphology for Application in Supercapacitors. *Chemistry – A European Journal* **15**, 5320-5326, doi:doi:10.1002/chem.200802671 (2009).

165 Cortie, M. B., der Lingen, E. & Pattrick, G. Catalysis and capacitance on nano-structured gold particles and sponges. *Proceedings of the Asia Pacific Nanotechnology Forum 2003*, 79-82 (2004).

166 Qiu, H. J. *et al.* Fabrication of large-scale nanoporous nickel with a tunable pore size for energy storage. *Journal of Power Sources* **247**, 896-905, doi:https://doi.org/10.1016/j.jpowsour.2013.08.070 (2014).

167 Ji, J. *et al.* Nanoporous Ni(OH)2 Thin Film on 3D Ultrathin-Graphite Foam for Asymmetric Supercapacitor. *ACS Nano* **7**, 6237-6243, doi:10.1021/nn4021955 (2013).

168 Salunkhe, R. R. *et al.* Asymmetric Supercapacitors Using 3D Nanoporous Carbon and Cobalt Oxide Electrodes Synthesized from a Single Metal–Organic Framework. *ACS Nano* **9**, 6288-6296, doi:10.1021/acsnano.5b01790 (2015).

169 Xie, K. *et al.* Highly ordered iron oxide nanotube arrays as electrodes for electrochemical energy storage. *Electrochemistry Communications* **13**, 657-660, doi:https://doi.org/10.1016/j.elecom.2011.03.040 (2011).

170 Saravanakumar, B., Purushothaman, K. K. & Muralidharan, G. Interconnected V2O5 Nanoporous Network for High-Performance Supercapacitors. *ACS Applied Materials & Interfaces* **4**, 4484-4490, doi:10.1021/am301162p (2012).

171 Wang, D., Wang, Q. & Wang, T. Morphology-Controllable Synthesis of Cobalt Oxalates and Their Conversion to Mesoporous Co3O4 Nanostructures for Application in Supercapacitors. *Inorganic Chemistry* **50**, 6482-6492, doi:10.1021/ic200309t (2011).

172 Wang, Z. *et al.* Broadband multilayer polarizers for the extreme ultraviolet. *Journal of Applied Physics* **99**, 056108, doi:10.1063/1.2179152 (2006).

173 Tan, M. Y. *et al.* Molybdenum–silicon aperiodic multilayer broadband polarizer for 13–30nm wavelength range. *Nuclear Instruments and Methods in Physics Research Section A: Accelerators, Spectrometers, Detectors and Associated Equipment* **654**, 588-591, doi:http://dx.doi.org/10.1016/j.nima.2011.07.007 (2011).

174 Catalanotti, S. *et al.* The radiative cooling of selective surfaces. *Solar Energy* **17**, 83-89, doi:https://doi.org/10.1016/0038-092X(75)90062-6 (1975).

175 Granqvist, C. G. & Hjortsberg, A. Radiative cooling to low temperatures: General considerations and application to selectively emitting SiO films. *Journal of Applied Physics* **52**, 4205-4220, doi:10.1063/1.329270 (1981).

176 Randich, E. & Allred, D. D. Chemically vapor-deposited ZrB2 as a selective solar absorber. *Thin Solid Films* **83**, 393-398, doi:https://doi.org/10.1016/0040-6090(81)90646-5 (1981).

177 Granqvist, C. G., Hjortsberg, A. & Eriksson, T. S. Radiative cooling to low temperatures with selectivity IR-emitting surfaces. *Thin Solid Films* **90**, 187-190, doi:https://doi.org/10.1016/0040-6090(82)90648-4 (1982).

178 Granqvist, C. G. Radiative heating and cooling with spectrally selective surfaces. *Appl. Opt.* **20**, 2606-2615, doi:10.1364/AO.20.002606 (1981).

179 Chen, Z., Zhu, L., Raman, A. & Fan, S. Radiative cooling to deep sub-freezing temperatures through a 24-h day–night cycle. *Nature Communications* **7**, 13729, doi:10.1038/ncomms13729

https://www.nature.com/articles/ncomms13729#supplementary-information (2016).

180 Rephaeli, E., Raman, A. & Fan, S. Ultrabroadband Photonic Structures To Achieve High-Performance Daytime Radiative Cooling. *Nano Letters* **13**, 1457-1461, doi:10.1021/nl4004283 (2013).

181 Ono, M., Chen, K., Li, W. & Fan, S. Self-adaptive radiative cooling based on phase change materials. *Opt. Express* **26**, A777-A787, doi:10.1364/OE.26.00A777 (2018).

182 Gentle, A., Maaroof, A. & Smith, G. Nanograin VO2 in the metal phase: a plasmonic system with falling dc resistivity as temperature rises. *Nanotechnology* **18**, 025202 (2006).

183 Gentle, A. R., Smith, G. B. & Maaroof, A. I. Frequency and percolation dependence of the observed phase transition in nanostructured and doped VO2 thin films. *Journal of Nanophotonics* **3**, 031505 (2009).

184 Leahu, G., Li Voti, R., Sibilia, C. & Bertolotti, M. Anomalous optical switching and thermal hysteresis during semiconductor-metal phase transition of VO2 films on Si substrate. *Applied Physics Letters* **103**, 231114 (2013).

185 Hendaoui, A., Émond, N., Chaker, M. & Haddad, É. Highly tunable-emittance radiator based on semiconductor-metal transition of VO2 thin films. *Applied Physics Letters* **102**, 061107 (2013).

186 Kats, M. A. *et al.* Vanadium dioxide as a natural disordered metamaterial: perfect thermal emission and large broadband negative differential thermal emittance. *Physical Review X* **3**, 041004 (2013).

187 Bevans, J., Luedke, E. & Nelson, K. A device for the rapid measurement of total emittance. *Journal of Spacecraft and Rockets* **3**, 758-760 (1966).

188 Khan, M. & Islam, M. Deposition and characterization of molybdenum thin films using dc-plasma magnetron sputtering. *Semiconductors* **47**, 1610-1615, doi:10.1134/s1063782613140017 (2013).

189 Scofield, J. H., Duda, A., Albin, D., Ballard, B. L. & Predecki, P. K. Sputtered molybdenum bilayer back contact for copper indium diselenide-based polycrystalline thin-film solar cells. *Thin Solid Films* **260**, 26-31, doi:http://dx.doi.org/10.1016/0040-6090(94)06462-8 (1995).